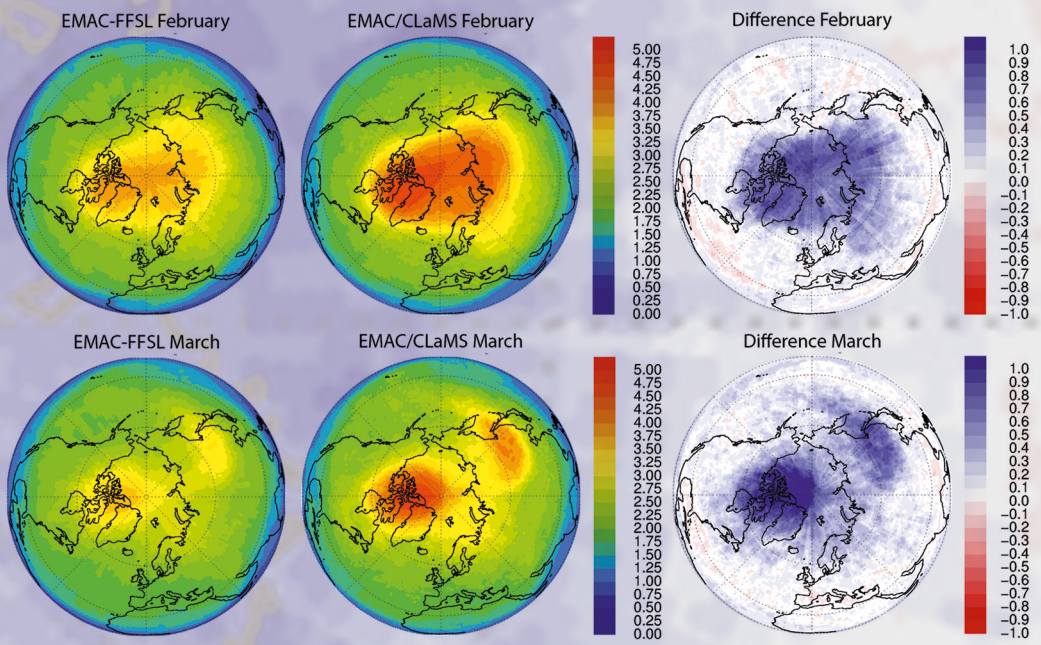

A Lagrangian transport core for the simulation of stratospheric trace species in a Chemistry Climate Model

Charlotte Marinke Hoppe

Member of the Helmholtz Association

JÜLICH
FORSCHUNGSZENTRUM

Schriften des Forschungszentrums Jülich
Reihe Energie & Umwelt / Energy & Environment Band / Volume 226

Forschungszentrum Jülich GmbH
Institute of Energy and Climate Research
Stratosphere (IEK-7)

A Lagrangian transport core for the simulation of stratospheric trace species in a Chemistry Climate Model

Charlotte Marinke Hoppe

Schriften des Forschungszentrums Jülich
Reihe Energie & Umwelt / Energy & Environment Band / Volume 226

ISSN 1866-1793 ISBN 978-3-89336-984-3

Bibliographic information published by the Deutsche Nationalbibliothek.
The Deutsche Nationalbibliothek lists this publication in the Deutsche Nationalbibliografie; detailed bibliographic data are available in the Internet at http://dnb.d-nb.de.

Publisher and Distributor: Forschungszentrum Jülich GmbH
Zentralbibliothek
52425 Jülich
Tel: +49 2461 61-5368
Fax: +49 2461 61-6103
Email: zb-publikation@fz-juelich.de
www.fz-juelich.de/zb

Cover Design: Grafische Medien, Forschungszentrum Jülich GmbH

Printer: Grafische Medien, Forschungszentrum Jülich GmbH

Schriften des Forschungszentrums Jülich
Reihe Energie & Umwelt / Energy & Environment, Band / Volume 226

D 468 (Diss., Wuppertal, Univ., 2014)

ISSN 1866-1793
ISBN 978-3-89336-984-3

The complete volume is freely available on the Internet on the Jülicher Open Access Server (JUWEL) at www.fz-juelich.de/zb/juwel

Abstract

Lagrangian transport schemes have proven to be useful tools for modelling stratospheric trace gas transport since they are less diffusive than classical Eulerian schemes and therefore especially well suited for maintaining steep tracer gradients as observed in the atmosphere. Here, the implementation of the full-Lagrangian transport core of the Chemical Lagrangian Model of the Stratosphere (CLaMS) in the ECHAM/MESSy Atmospheric Chemistry model (EMAC) is presented. A ten-year time-slice simulation was performed to evaluate the coupled model system EMAC/CLaMS. Simulated zonal mean age of air distributions were compared to the age of air derived from airborne measurements, showing the expected characteristics of the stratospheric circulation. Climatologies of long-lived tracers (CFC-11 (CCl_3F), CFC-12 (CCl_2F_2), CH_4, N_2O) were calculated using the standard flux-form semi-Lagrangian transport scheme (FFSL) in EMAC, as well as the new CLaMS Lagrangian transport scheme. The climatologies were compared both to each other and also to satellite measurements of trace gases. The differences in the resulting tracer distributions are most pronounced in the regions of strong transport barriers, namely the edge of the tropical pipe, the tropopause, and the edge of the polar vortex. These regions were analysed in detail and show improved results using the Lagrangian transport scheme, with stronger gradients at the respective transport barriers. The analyses of various trace gases and age of air in the polar vortex regions shows that the CLaMS Lagrangian transport scheme produces a stronger, more realistic transport barrier at the edge of the polar vortex than the FFSL transport scheme of EMAC. Differences in simulated age of air are in the range of up to one year in the Arctic polar vortex in late winter/early spring. The newly coupled model system EMAC/CLaMS thus constitutes a suitable tool for future model studies, e.g. for the simulation of polar ozone depletion, based on a sophisticated stratospheric tracer transport.

Zusammenfassung

Lagrangesche Transportschemata sind besonders gut für die Simulation von stratosphärischen Spurengasen geeignet, da sie die numerische Diffusion, die notwendigerweise in klassischen Eulerischen Modellen auftritt, deutlich reduzieren. So ist es möglich, starke Gradienten an Transportbarrieren aufrecht zu erhalten, so wie sie in der Atmosphäre beobachtet werden. Diese Arbeit präsentiert das neu entwickelte, gekoppelte Modell EMAC/CLaMS, bestehend aus dem Lagrangeschen Transportschema aus dem Chemical Lagrangian Model of the Stratosphere (CLaMS) integriert in das Chemie-Klima-Modell ECHAM/MESSy Atmospheric Chemistry Model (EMAC). Zur Validierung dieses Modellsystems werden Ergebnisse aus einem Zeitscheibenlauf über 10 Jahre analysiert. Modellierte und aus Messungen bestimmte Verteilungen des Alters der Luft werden miteinander verglichen und die gute Übereinstimmung zeigt, dass die stratosphärische Zirkulation im Modell insgesamt gut wiedergegeben wird. Klimatologien für langlebige Spurengase wie CFC-11 (CCl_3F), CFC-12 (CCl_2F_2), CH_4 und N_2O) wurden sowohl für das neue Lagrangesche CLaMS Transportschema, als auch für das Standard Semi-Lagrangesche Transportschema in Flussform (FFSL) erstellt. Diese Klimatologien werden miteinander und mit Spurengasklimatologien aus Satellitenmessungen verglichen. Die größten Unterschiede zwischen beiden Transportschemata zeigen sich in Regionen, in denen sich starke atmosphärische Transportbarrieren befinden, das heißt am subtropischen und polaren Jet, sowie an der Tropopause. Eine Analyse dieser Regionen zeigt, dass das Lagrangesche Transportschema hier verbesserte, d.h. stärkere Gradienten in den Spurengasverteilungen aufweist. Am Beispiel des Polarwirbels wird gezeigt, dass die stärkere und realistischere Transportbarriere mit dem Lagrangeschen Transportschema zu Altersunterschieden von bis zu einem Jahr im Arktischen Polarwirbel führt. Insgesamt zeigt die vorliegende Arbeit, dass das neue gekoppelte Modell EMAC/CLaMS realistische stratosphärische Spurengasverteilungen simuliert und daher für zukünftige Modellstudien verwendet werden kann.

Contents

CHAPTER 1

Introduction

Climate affects many aspects of human life, such as energy use and natural resources, human and ecosystem health, economies, and national and international policies. Since the 1950s, many changes in the climate system have been observed, in particular a warming of the atmosphere and ocean, a rise in sea level, and increasing greenhouse gas concentrations [*IPCC*, 2013]. Profound, reliable scientific information about climate change is important for the dicision making process for governments and people.

Numerical models are essential tools in climate research since they are the only way to produce projections of future climate evolution. The algorithms of climate models comprise the current knowledge of the Earth climate system. Developing climate models aims at a better understanding of relevant processes, a better representation of these processes in models, and at improved projections of future climate.

Chemistry climate models (CCMs) allow, in addition to atmospheric dynamics, transport and chemistry of chemical tracers to be described from the surface to the stratosphere and above. CCMs are key tools for projections of the future development of the stratosphere and in particular of the stratospheric ozone layer [e.g., *Eyring et al.*, 2005; *WMO*, 2011; *IPCC*, 2013]. Furthermore, such models are important for climate modelling because they are able to describe the impact of stratospheric change such as ozone depletion on tropospheric climate and to simulate the atmospheric response to tropospheric perturbations [*Shaw and Shepherd*, 2008;

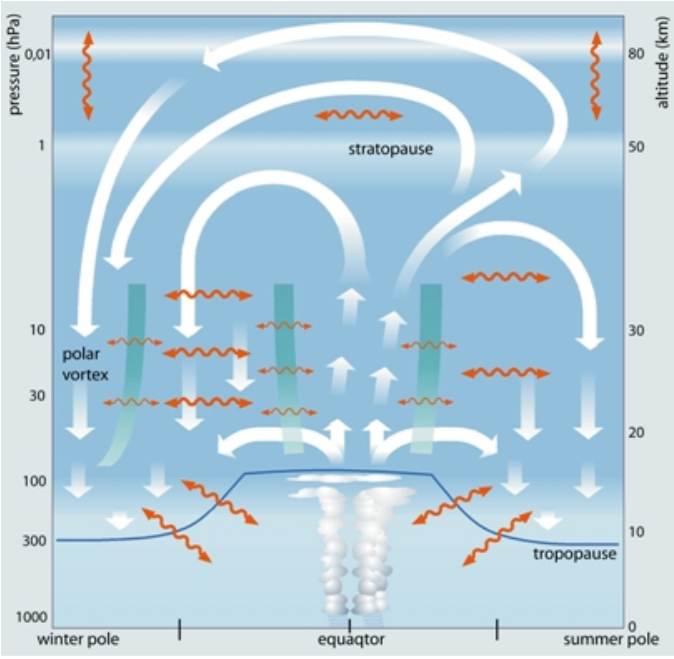

Figure 1.1: Schematic of the stratospheric circulation. Bold, white arrows display the Brewer-Dobson-Circulation. Red, wavy arrows indicate mixing processes and horizontal, isentropic transport. The turquoise bars in the stratosphere mark the transport barriers at the edges of the tropical pipe and of the polar vortex. Figure taken from *Bönisch et al.* [2011].

Thompson and Solomon, 2002; *Son et al.*, 2008]. Without including the interaction between stratospheric change and tropospheric response in the models, reliable projections of tropospheric climate change are impossible.

A schematic of transport processes in the stratosphere is presented in Fig. 1.1. The long-term stratospheric circulation (Brewer-Dobson-Circulation) is composed of an upwelling in the tropics and a downwelling in the extratropics. Mixing on short time scales occurs primarily on isentropic surfaces in the mid-latitudes in the so-called surfzone (see horizontal, wavy arrows in Fig. 1.1). Certain transport barriers are present in the stratosphere, namely at the tropopause, at the edges of the tropical upwelling region, and at the edge of the polar vortex in the winter hemisphere.

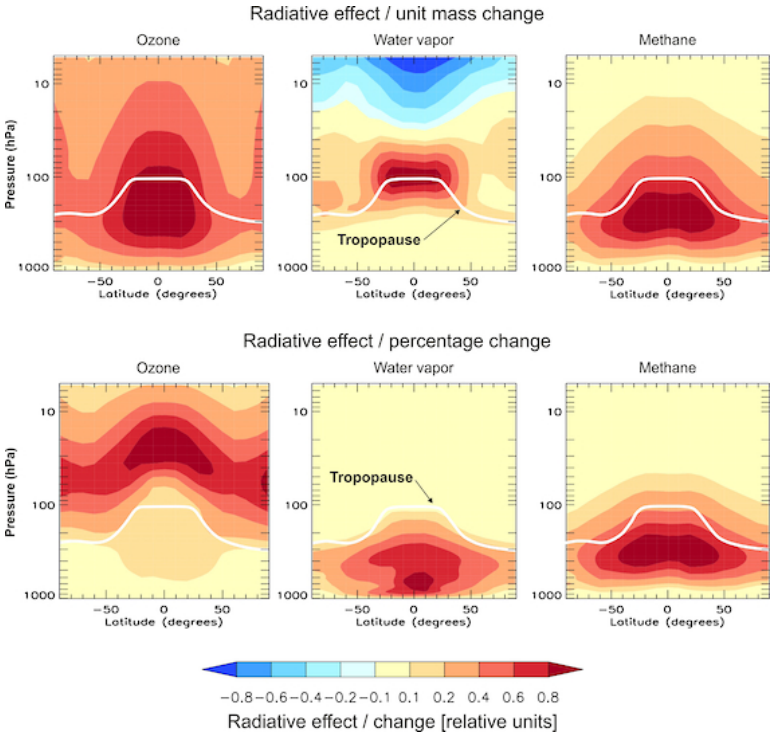

Figure 1.2: Sensitivity of surface temperature to the altitude and latitude of (left) ozone, (middle) water vapour, and (right) methane changes. Filled contours show relative impact on surface temperature, measured as radiative effect, from either (top) unit mass increases or (bottom) percentage increases applied at individual latitudes and altitudes (1 km thick layers). For each trace gas the calculated radiative effects have been normalised to the respective maximum value. Red tones are indicative of warming, blue tones indicate cooling. Figure taken from *Riese et al.* [2012].

For the description of surface climate change and its decadal variability it is important for the model to have an accurate description of water vapour in the upper troposphere/lower stratosphere (UTLS) region [*Solomon et al.*, 2010; *Riese et al.*, 2012]. Other trace gases are important as well. The impact of changes in ozone, water vapour and methane in the UTLS region is illustrated in Fig. 1.2. Clearly, the radiative effect per unit mass change of these trace gases is largest around the tropopause. Thus, in a climate simulation, small uncertainties in mixing ratios of these species in the UTLS region lead to large uncertainties in radiative forcing. For this reason it is very important to have an accurate representation of the UTLS region in climate models.

However, when tested in a process focussed manner against observations, simulations of CCMs still show several important deficits [*SPARC*, 2010]. In particular, a good representation of transport in the vicinity of strong tracer gradients (e.g. tropopause, polar and subtropical jet) is a challenge for the transport schemes of CCMs [e.g. *SPARC*, 2010; *Strahan et al.*, 2011]. Moreover, the velocity of upward transport throughout the stratosphere is insufficiently known, which constitutes an important obstacle for a description of the Brewer-Dobson-Circulation and its change with climate change [*Schoeberl et al.*, 2012; *Ploeger et al.*, 2012b; *Randel and Jensen*, 2013].

In studies using chemistry transport models (CTMs) and CCMs, the Lagrangian concept of transport has been proven to be successful [e.g., *McKenna et al.*, 2002a, b; *Konopka et al.*, 2004; *Stenke et al.*, 2009; *Wohltmann and Rex*, 2009] in overcoming the inherent numerical diffusivity of Eulerian transport schemes. In a pure Lagrangian transport scheme, transport of chemical tracers is described by an ensemble of air parcels that move along trajectories. These trajectories are calculated based on prescribed wind fields. The advantage of this transport representation is that the advection is non-diffusive and therefore very good in maintaining transport barriers and the assiciated trace gas gradients in simulations of atmospheric trace species.

Figure 1.3 illustrates the general difference between Lagrangian and semi-Lagrangian transport schemes. In a semi-Lagrangian or in a Eulerian scheme, the data points are located on a fixed grid structure (left panel of Fig. 1.3). At the end of each time step, values for tracer mixing ratios have to be interpolated to the grid point locations. This interpolation causes numerical diffusion since the tracer mixing ratio at each grid point is the weighted mean of the surrounding grid box. In contrast, in a full Lagrangian transport scheme (right panel in Fig. 1.3), data points are air parcels that may freely move since they are not bound to a fixed grid. During this

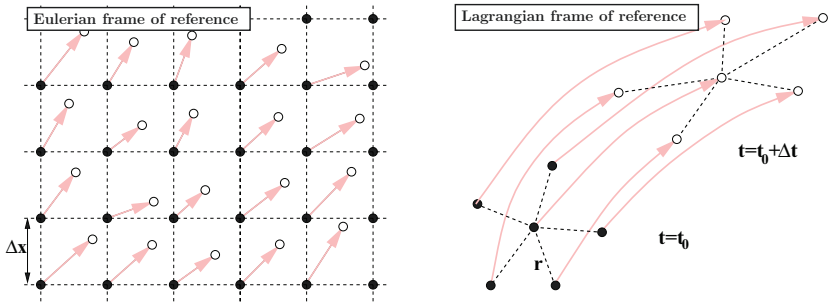

Figure 1.3: Schematic of semi-Lagrangian (left) and full-Lagrangian (right) transport. Data points are indicated by black dots, and positions after advection by open circles. The stratospheric circulation is visualised by pink arrows. Black dashed lines indicate the model grid in the Eulerian representation and the distance to the nearest neighbouring air parcels in the Lagrangian representation. Courtesy of P. Konopka.

transport time step all air parcels maintain their properties, in particular the mixing ratio of a chemical tracer. Thus, no interpolation is required for the advection part of a full-Lagrangian transport scheme.

The present work describes the integration of the transport core of the Chemical Lagrangian Model of the Stratosphere [CLaMS, *McKenna et al.*, 2002a, b] into the chemistry climate model ECHAM/MESSY Atmospheric Chemistry model [EMAC, *Jöckel et al.*, 2005, 2010]. CLaMS is especially designed for simulations of the stratosphere and the UTLS region. There are two main differences between the CLaMS transport scheme and the standard flux-form semi-Lagrangian transport scheme in EMAC [*Lin and Rood*, 1996]: First, CLaMS provides a full-Lagrangian transport scheme which has the advantage of being non-diffusive, as described above. The second difference is the choice of the vertical coordinate [*Kasahara*, 1974] and thus the representation of vertical velocities. As most CCMs, EMAC employs a pressure-based grid structure. The vertical velocities for tracer transport in EMAC are calculated by the transport scheme as a residual from the horizontal flux divergence using the continuity equation [*Lin*, 2004]. In contrast, CLaMS vertical coordinates in the stratosphere are defined on levels of constant potential temperature, and thus vertical velocities are derived from diabatic heating rates due to radiation, latent heat release, and other diabatic processes like turbulent mixing [*Konopka et al.*, 2012].

The approximate adiabatic nature of atmospheric large-scale motion such as planetary wave propagation, with the flow mainly being along isentropic surfaces, should favour the diabatic approach based on the isentropic coordinate system [*Mahowald et al.*, 2002].

A different Lagrangian transport model [Atmospheric Tracer Transport in a Lagrangian Model (ATTILA), *Reithmeier and Sausen*, 2002] has also been coupled to the ECHAM climate model. *Stenke et al.* [2008] show that the wet bias in stratospheric water vapour could be significantly reduced using the Lagrangian transport scheme ATTILA. In *Stenke et al.* [2009], this coupled model was expanded to a chemistry transport model. The Cl_y simulation could be improved considerably in this coupled model compared to the previously used semi-Lagrangian transport scheme. Although ATTILA and CLaMS are both Lagrangian transport schemes, they differ in many respects, e.g. the air parcel definition. In CLaMS, the air parcels are small data points which transport mixing ratios of chemical tracers that are representative of the surrounding air. In contrast, in ATTILA an air parcel represents a specified air mass. As there are no isolated air parcels in reality, mixing has to be included in Lagrangian transport models. The mixing algorithms also differ between CLaMS and ATTILA. In ATTILA, mixing is realised through nudging towards the mean value in the grid box in which the Lagrangian air parcels are located at the mixing time step, while in CLaMS mixing is dependent on the flow deformation.

The purpose of this thesis is to introduce and to evaluate the new coupled model system EMAC/CLaMS. The impact of the Lagrangian transport on trace gas distributions is investigated and the results are compared to those calculated with the standard flux-form semi-Lagrangian transport scheme in EMAC.

Outline

The next chapter introduces the chemistry transport model CLaMS and the chemistry climate model EMAC. In particular, the coupling strategy via the interface structure Modular Earth Submodel System (MESSy) is explained here. The end of Chapter 2 describes the setup used for the ten-year time-slice simulation in this study.

Chapter 3 contains a discussion of different representations of vertical velocity. The kinematic vertical velocity that drives transport in the standard flux-form semi-Lagrangian (FFSL) transport scheme, and the diabatic vertical velocity that is used in the CLaMS Lagrangian transport scheme are described. By applying the Trans-

formed Eulerian mean [TEM, *Andrews et al.*, 1987] to the kinematic vertical velocity fields, the latter can be compared to the zonal mean diabatic vertical velocities. Climatologies of both kinematic and diabatic vertical velocities in EMAC are presented.

The following chapters focus on the representation of regions in the vicinity of stratospheric transport barriers where strong gradients in the tracer distributions are expected.

Chapter 4 analyses the representation of the tropical upwelling region and the subtropical transport barrier using N_2O distributions. The influence of the quasi-biannual oscillation [QBO, *Baldwin et al.*, 2001] on trace gas anomaly patterns is discussed. The impact of transport barriers at the subtropical jet stream and the extratropical tropopause on age of air is demonstrated.

Chapter 5 presents an analysis of the Arctic and Antarctic polar vortex regions in the simulation using FFSL and CLaMS as two different transport schemes. Simulated age of air and trace gas distributions from both transport schemes are compared to each other and are validated with measurement climatologies.

In Chapter 6, zonal mean trace gas and age of air climatologies are presented. Differences between climatologies derived with the FFSL transport scheme and climatologies derived with the new CLaMS Lagrangian transport scheme are analysed. The climatologies from the simulation are compared to satellite measurements. As an example for an application of trace gas climatologies, relative lifetimes of CFC-12 and CFC-11 are derived based on the results of the model simulation. Summary and conclusions are presented in Chapter 7.

Publications

The results of this work will be reported in a number of publications, two of which are in a rather advanced state. The details of the implementation of the Lagrangian transport core into the CCM EMAC is described in:

C. M. Hoppe, L. Hoffmann, P. Konopka, J.-U. Grooß, F. Ploeger, G. Günther, P. Jöckel, and R. Müller: The implementation of the CLaMS Lagrangian transport core into the chemistry climate model EMAC2.40.1: Application on age of air and transport of long-lived trace species, Geosci. Model Dev. Discuss., 7*, 1759-1790, 2014*

A further, important result of this thesis was the information of stratospheric degradation of CFC-11 and CFC-12 in the simplified chemistry scheme of CLaMS and the

resulting analysis of CFC-11 and CFC-12 lifetimes, which are a contribution to:

L. Hoffmann, C. M. Hoppe, R. Müller, G. S. Dutton, J. C. Gille, S. Griessbach, A. Jones, C. I. Meyer, R. Spang, C. M. Volk, and K. A. Walker: Stratospheric lifetime ratio of CFC-11 and CFC-12 from satellite and model climatologies, in preparation for Atmos. Chem. Phys.

CHAPTER 2

Model description

2.1 The Lagrangian chemistry transport model CLaMS

The Chemical Lagrangian Model of the Stratosphere (CLaMS), a modular chemistry transport model (CTM), is introduced in this section. The model is described in more detail elsewhere [e.g., *McKenna et al.*, 2002a, b; *Konopka et al.*, 2004; *Grooß et al.*, 2011; *Konopka et al.*, 2012]. CLaMS comprises three main modules for Lagrangian advection, mixing, and stratospheric chemistry, as well as several other modules for the simulation of various physical and chemical processes in the atmosphere. Due to its full-Lagrangian transport scheme, CLaMS is especially well suited for maintaining atmospheric transport barriers, in particular at the edges of the tropical pipe and the polar vortex [e.g., *Steinhorst et al.*, 2005; *Günther et al.*, 2008; *Konopka et al.*, 2010; *Ploeger et al.*, 2013].

Figure 2.1 shows an example for the distribution of CLaMS air parcels in the UTLS region. It is visible that the air parcels are not equally distributed, instead they follow the wind field. In the regions of the subtropical jet streams, where strong temperature gradients are present, the air parcels follow the wavy structure of the jet. In vicinity of the strong transport barrier at the subtropical jet in the winter hemisphere (Northern hemisphere in the example shown in Fig. 2.1), the density of air parcels is larger than in other regions. However, no big gaps occur in the air parcel distribution, so that every region is represented in the model.

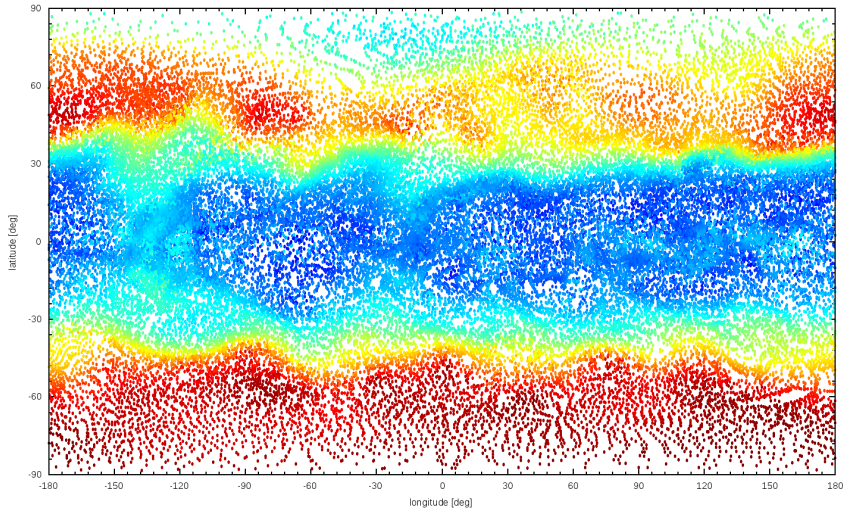

Figure 2.1: CLaMS air parcels in the UTLS region, i.e. in the potential temperature range from 380 K to 420 K at 6th Jan 2005, 0:00 UTC. The colour of the air parcels denotes the temperature at the air parcel position. Temperatures range from 180 K (blue) to 230 K (red).

2.1.1 Trajectory calculation

The CLaMS trajectory module (TRAJ) performs the full-Lagrangian, non-diffusive, three-dimensional advection of an ensemble of air parcels [*Sutton et al.*, 1994]. The numerical integration is based on a 4th-order Runge-Kutta scheme.

Required input fields are horizontal and vertical winds, e.g. from ERA-Interim reanalysis products [*Dee et al.*, 2011]. The representation of the vertical winds depends on the choice of the vertical coordinate system. It is possible to use different vertical coordinates in CLaMS, e.g. potential temperature θ in which case vertical winds would be determined as $\dot{\theta} = Q$, with Q the diabatic heating rate. In this study, the hybrid σ-θ coordinate ζ with $\dot{\zeta}$ as vertical velocity is used, as proposed by *Mahowald et al.* [2002]. The ζ-coordinate combines the terrain-following σ-coordinate ($\sigma = \frac{p}{p_s}$ where p_s is surface pressure) for the troposphere and the θ-coordinate for the radiation-dominated stratosphere. ζ is defined as follows:

$$\zeta = \theta \, \mathrm{f}(\sigma) \tag{2.1}$$

with

$$\mathrm{f}(\sigma) = \begin{cases} \sin(\frac{\pi}{2} \frac{1-\sigma}{1-\sigma_r}) & \sigma > \sigma_r \\ 1 & \sigma \leq \sigma_r \end{cases} \tag{2.2}$$

The implementation of ζ as a vertical coordinate in CLaMS is described in detail in *Konopka et al.* [2007, 2012]. In the present study, $\sigma_r = \frac{p_r}{p_s}$ is used which means that above the reference height p_r (300 hPa in this study) ζ is equal to the potential temperature θ.

2.1.2 Mixing

CLaMS includes a mixing module (MIX), so that air parcels are not completely isolated and some exchange is allowed in situations where strong flow deformation is present in the atmosphere. This constitutes the irreversible part of the CLaMS transport. The mixing of the air parcels in the CLaMS module MIX is controlled by the horizontal strain and vertical shear of the wind field [*McKenna et al.*, 2002b; *Konopka et al.*, 2007]. The mixing routine is usually called every 24 hours after the trajectory transport. One mixing event contains the following steps: First, discrete vertical layers are defined according to an entropy criterion such that each of those layers contains approximately the same number of air parcels [for details see *Konopka*

et al., 2007, 2012]. Second, the procedure that is illustrated in Fig. 2.2 is applied separately in each layer: Nearest neighbours of each air parcel before the advection are identified using Delaunay triangulation on a horizontal projection of the vertical layer (left panel in Fig. 2.2). For this step, the former air parcel positions are needed. The middle panel in Fig. 2.2 shows the wind field that moved the air parcels during the advection time step Δt. In this particular case, a strong wind shear including a shift in direction is present. The right panel in Fig. 2.2 shows the air parcel positions after the advection. If the distance between two neighbouring air parcels after the Lagrangian advection exceeds r_+^c, as defined in Eq. (2.3), a new air parcel is inserted in the middle. In the shown example, the distance between air parcels A and B has become too large according to Eq. (2.3), so the air parcel D is inserted between them. In cases where two air parcels are closer than r_-^c, they are merged such that they form one new air parcel. The air parcels A and C are merged in this example. In other cases, no mixing occurs. The critical radii $r_\pm^c$ are defined as follows:

$$r_\pm^c = r_0 \exp(\pm\lambda_c \Delta t) \tag{2.3}$$

In Eq. (2.3), r_0 is the mean horizontal distance of air parcels in the layer. The critical Lyapunov exponent λ_c, a measure of the deformation in the flow, determines the mixing strength in the model. In CLaMS, mixing is triggered in regions where the deformation is stronger than the critical deformation defined by λ_c. The impact of the uncertainty in the mixing strength is investigated in *Konopka et al.* [2004] and *Riese et al.* [2012] through varying the parameter λ_c. The pure Lagrangian trajectory advection is non-diffusive. The mixing adds some diffusion to the CLaMS Lagrangian transport (i.e. advection and mixing). The advantage of the CLaMS mixing procedure is that it is built in a physically-based manner, i.e. mixing occurs in regions of strong flow deformation and thus where it is expected in reality.

2.1.3 Chemistry

The original CLaMS version contains a detailed stratospheric chemistry scheme [CHEM, *McKenna et al.*, 2002a] involving around 150 species. The numerical solver is based on the A Self-contained Atmospheric chemistry coDe [ASAD, *Carver et al.*, 1997]. A simplified version was used for coupling to a climate model since it is more suitable for long-term simulations [*Pommrich et al.*, 2014]. The simplified scheme is called every 24 hours and uses daily-mean photolysis rates. It was used to investigate tropical upwelling by analysing the simulated CO pattern and its variability

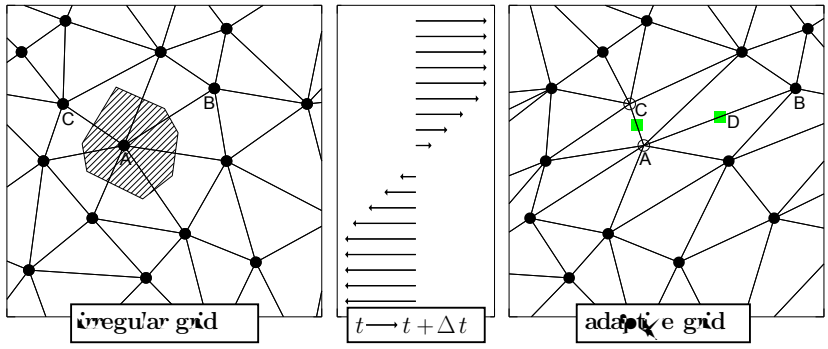

Figure 2.2: Schematic of the adative grid in the CLaMS mixing module. Air parcels are represented by the black dots, and nearest neighbours are connected by thin black lines. Unfilled dots in the right panel denote air parcels that are deleted by the mixing algorithm, while green squares denote air parcels that are created by the mixing algorithm. The left panel displays the position of the air parcels before the advection, and the right panel the positions after the advection. The middle panel shows the wind shear that triggers the mixing. Courtesy of P. Konopka.

by *Pommrich et al.* [2014]. Additionally, the simplified chemistry scheme allows for the reproduction of stratospheric loss of long-lived tracers (CCl_3F (CFC-11), CCl_2F_2 (CFC-12), N_2O, and CH_4) and describes the water vapour production by methane-oxidation.

The equations of the simplified chemistry scheme are designed to parametrise the net result of reaction cycles and can not be written stoichiometrically correct. The following parametrised chemical reactions are included in the chemistry algorithm (for details see *Pommrich et al.* [2014]):

$$CO + OH \longrightarrow CO_2 + \text{products} \tag{2.4}$$
$$CH_4 + OH \longrightarrow 2H_2O + CO + \text{products} \tag{2.5}$$
$$CH_4 + O(^1D) \longrightarrow 2H_2O + CO + \text{products} \tag{2.6}$$
$$CH_4 + Cl \longrightarrow 2H_2O + CO + \text{products} \tag{2.7}$$
$$N_2O + O(^1D) \longrightarrow \text{products} \tag{2.8}$$
$$N_2O + h\nu \longrightarrow \text{products} \tag{2.9}$$
$$CCl_3F + h\nu \longrightarrow \text{products} \tag{2.10}$$
$$CCl_2F_2 + h\nu \longrightarrow \text{products} \tag{2.11}$$
$$O_2 + h\nu(+2\,O_2) \longrightarrow 2O_3 \tag{2.12}$$
$$[O_3 + OH \longrightarrow HO_2 + O_2] \times {}_0 \tag{2.13}$$
$$[O_3 + HO_2 \longrightarrow OH + 2O_2] \times {}_2 \tag{2.14}$$

Reactions (2.12) to (2.14) describe the ozone chemistry in the lower stratosphere. Through the parametrised reactions in the simplified chemistry scheme, the O_3 budget is well represented in the upper tropical tropopause layer and in the lower stratosphere [*Ploeger et al.*, 2011, 2012a].

2.2 The chemistry climate model EMAC

The ECHAM/MESSY Atmospheric Chemistry model (EMAC) is a chemistry climate model (CCM) that comprises the climate model ECHAM5 [*Röckner et al.*, 2006] and the interface structure Modular Earth Submodel System [MESSy, *Jöckel et al.*, 2010].

MESSy provides a coupling interface structure for developing Earth system models with the flexibility to vary between many geophysical processes that are included as

submodels. Thus, single process parametrisations can be easily switched on and off. Additionally, for many processes, multiple parametrisation schemes are available in MESSy, so that it is possible to select the parametrisation which is most suitable for the current simulation.

MESSy includes various submodels, i.e. for tropospheric and middle atmosphere processes, ocean modules, land surface interaction, and anthropogenic emissions. The first version of MESSy [*Jöckel et al.*, 2006] was developed only for coupling submodels with ECHAM5, whereas the second version [*Jöckel et al.*, 2010] is also suitable for other basemodels, e.g. regional weather forecast models. For the current study, the MESSy version 2.40.1 was used.

2.2.1 The climate model ECHAM5

The present study uses the climate model ECHAM5 [*Röckner et al.*, 2006] as basemodel in MESSy. This climate model is the fifth generation of the atmospheric circulation model ECHAM, which evolved from the spectral weather prediction model developed by the European Centre for Medium-Range Weather Forecasts [ECMWF, *Simmons et al.*, 1989]. *Roeckner et al.* [2003] provide a detailed description of the ECHAM5 model.

The dynamics in ECHAM5 is calculated using expansions of the meteorological prognostic variables in spectral harmonics. The basic prognostic variables vorticity, divergence, temperature, and surface pressure are calculated in the spectral representation. The advantage of the spherical representation is that the derivatives can be solved analytically. Thus, the dynamical core calculates the coefficients of a series of truncated spherical harmonics.

For the interpretation of the model results, the variables derived in the spectral representation have to be transformed to a gridpoint representation. The number of basis functions in the spherical approach determines the horizontal resolution of the model grid. In the present study, a truncation at wave number 42 is applied. This corresponds to 64 associated Gaussian latitudes in the model grid, and 128 gridpoints in longitudinal direction, so that the horizontal resolution is about 2.8° in latitude and longitude at the equator.

The parametrisations in ECHAM5, e.g. radiation and tracer transport are calculated in the gridpoint representation.

For the vertical grid structure in ECHAM5, a hybrid σ-pressure coordinate is used. The middle atmosphere version of ECHAM5 contains 90 vertical layers up to 0.01 hPa.

The pressure at the model layer interfaces ('half-level') defines the vertical grid, such that

$$p_{k+1/2} = A_{k+1/2} + B_{k+1/2} \cdot p_s. \tag{2.15}$$

Here, $k = 0, ..., NLEV$ is the index of the model layer. The constants $A_{k+1/2}$ and $B_{k+1/2}$ define the vertical grid and are given by *Roeckner et al.* [2003]. In the lowest model layers, a pure σ coordinate is used by setting $A_{k+1/2} = 0$, while $B_{k+1/2} = 0$ in the upper model layers defines a pure pressure coordinate. The pressure at the model layer ('full-level') is defined by

$$p_k = \frac{1}{2}(p_{k-1/2} + p_{k+1/2}). \tag{2.16}$$

Thus, the pressure at a certain model level in ECHAM varies every timestep since it is dependent on the current surface pressure.

In the standard ECHAM5 setup, tracers are transported using a flux-form semi-Lagrangian transport scheme. The method of *Lin and Rood* [1996] for the extention of one-dimensional, flux-form advection schemes to multidimensions is integrated in ECHAM5. In the implementation of the scheme by *Lin and Rood* [1996] here, the horizontal transport is performed using the piece-wise parabolic method [PPM, *Carpenter et al.*, 1990]. The vertical transport is based on the use of the Huynh/Van Leer/Lin full monotonicity constraint [see Appendix B in *Lin*, 2004]. The vertical velocities are calculated internally in the transport scheme from the horizontal flux divergence using the continuity equation.

2.2.2 The MESSy interface structure

This section provides a short description of the architecture of the MESSy interface. A more detailed description is given in *Jöckel et al.* [2005, 2010]. The code of MESSy is structured, such that each FORTRAN95 module is assigned to one of the following four layers:

- The base model layer (BML): This part contains the source code of the base model. This can be for instance a climate model (ECHAM5 in our study), a simple boxmodel, or a regional weather forecast model.

- The base model interface layer (BMIL): This layer manages data input and

output, and the communication between particular submodels and the base model. Global variables are stored in special structures called 'channel objects'.

- The submodel interface layer (SMIL): This part of the code connects particular submodels to the BMIL. It sets pointers to the required global arrays in the BMIL. The SMIL contains the calls of the respective submodel routines for the initialization, time integration, and finalizing phase of the model.
- The submodel core layer (SMCL): The submodel source code is located in the SMCL. Examples for submodels are parameterizations of gravity waves, emissions of tracers or a mixed layer ocean.

MESSy includes a special submodel for dealing with atmospheric tracers. This submodel TRACER is described by *Jöckel et al.* [2008]. It provides a structure for coupling different external chemistry transport modules to a basemodel.

2.3 The coupled model system EMAC/CLaMS

The CLAMS main modules TRAJ, MIX, and CHEM were modified and integrated as new submodels in the MESSy interface structure. Other submodels, e.g. for the dehydration by cirrus cloud formation (CIRRUS) or for CLaMS boundary conditions (BMIX) were also included. There are two ways to use these CLaMS submodels in the MESSy interface (Fig. 2.3).

The first option is to run the coupled version with the ECHAM5 basemodel (left box in Fig. 2.3). In this case, CLaMS trajectories are driven by winds and heating rates from ECHAM5. The heating rates result from several process parameterisations, such as radiation, convection and clouds, gravity wave drag, and vertical diffusion. The MESSy interface also provides the possibility for two-way-coupling between processes. Thus, trace gas distributions derived by CLaMS could serve as input for the EMAC radiation calculation.

The second possible basemodel is the new developed CLaMS basemodel (right box in Fig. 2.3). Here, the meteorological input fields are read from external data files, e.g., from ERA-Interim reanalysis data. Running the CLaMS basemodel delivers the same result as the original uncoupled CLaMS model. Technically, the new CLaMS basemodel replaces a shell script that is used to run the original version of CLaMS. The single modules of the original version are represented as individual Fortran90 programs, which are started by the script. In the original version, data exchange

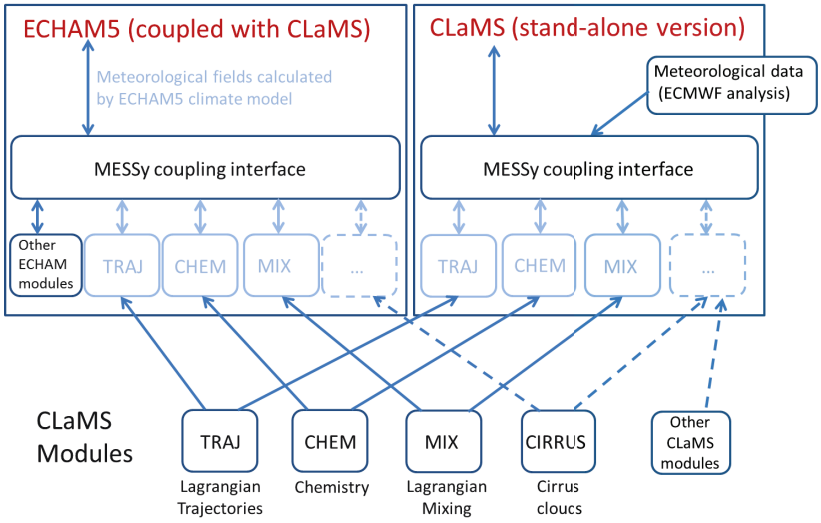

Figure 2.3: Schematic of the CLaMS modules integrated in the MESSy interface.

between the modules is achieved through NetCDF files. In contrast, in the MESSy version, the communication between the different modules is carried out via the interface structure in the BMIL, therefore no external data files and no file I/O are required for the communication between processes.

2.4 Simulation setup

This chapter presents example results of a ten-year time-slice simulation with the coupled EMAC/CLaMS model. In this simulation, two transport schemes were applied in parallel to describe the transport of two similar tracer sets. Tracer distributions calculated with the CLaMS full-Lagrangian transport scheme are compared to tracer fields derived from the flux-form semi-Lagrangian transport in EMAC. The transport with the full-Lagrangian transport scheme will be termed 'EMAC/CLaMS', and the one using the flux-form semi-Lagrangian transport will be denoted 'EMAC-FFSL'.

For this study, a ten-year time-slice simulation was performed with boundary conditions representing the year 2005. The underlying climate simulation was a free running ECHAM5 simulation without nudging to observations. The sea surface

temperature and sea ice concentration boundary conditions are taken from the Atmospheric Model Intercomparison Project [AMIP II, *Hurrell et al.*, 2008] climatology. The horizontal resolution is T42, which corresponds to a Gaussian grid with grid-boxes of approximately 2.8° in latitude and longitude ($\approx$ 300 km at the equator). The grid has 90 vertical levels from the surface up to 0.01 hPa ($\approx$ 80 km). The extent of the vertical levels (in km) is not equally distributed, instead it increases with altitude.

A group of chemical tracers is set up for each of the two transport schemes EMAC-FFSL and EMAC/CLaMS. The tracers include species for the simplified CLaMS chemistry scheme, as described in *Pommrich et al.* [2014]. The initial and boundary values for the tracer fields are taken from a climatological simulation with the uncoupled CLaMS model [*Pommrich et al.*, 2014] driven by ERA-Interim meteorological reanalysis data [*Dee et al.*, 2011]. As CFC-12 is not included in the CLaMS climatological run, the initial values for the CFC-12 mixing ratio in the EMAC/CLaMS simulation are obtained using three correlation functions of CFC-12 with N_2O for the tropics between 15°N and 15°S and the extratropics in the Northern and Southern hemisphere, respectively (J.-U. Groß, personal communication, Appendix C). The correlation between CFC-12 and N_2O were obtained from ACE-FTS satellite measurements (Sect. 5.1).

An age of air tracer is also added to each of the tracer sets [*Pommrich et al.*, 2011], implemented as a passive tracer with a linear increasing lower boundary condition ['clock-tracer', *Hall and Plumb*, 1994]. The mean age at a certain position in the atmosphere is derived from the difference between the local tracer value and the current value at the surface.

For the CLaMS transport scheme, about one million air parcels are set up from the surface up to the 2500 K potential temperature level. The number of air parcels is comparable to the number of gridpoints in the EMAC grid. However, the distribution of the data points is different for the two transport representations, as CLaMS air parcels are initialized in vertical layers that all have the same amount of entropy [*Konopka et al.*, 2007, 2012]. Every 24 hours, the CLaMS mixing procedure is applied on the ensemble of CLaMS air parcels and the simplified chemistry is calculated. The mixing parameters are set to $\lambda_c = 1.2\,\mathrm{day}^{-1}$ and $r_0 = 300\,\mathrm{km}$. The boundaries are updated after every mixing event.

A similar tracer set is defined in the EMAC gridpoint space for the EMAC-FFSL transport. These tracers are transported by the flux-form semi-Lagrangian trans-

port scheme. The same chemistry algorithm (CLaMS simplified chemistry) as for EMAC/CLaMS is also applied on the EMAC-FFSL tracer set. As already mentioned, the same boundary and initial values are used for both tracer sets.

Climatologies have been produced for the EMAC/CLaMS and EMAC-FFSL simulation results. Data are interpolated to the same regular grid structure for the daily output, and monthly mean values are calculated for each month. Then, the respective monthly means for all 10 years of simulation are used for the climatology. Climatologies averaged over the whole simulation period of 10 years have been compared to climatologies derived only from the last 5 years of output to test if there are large influences from the initialisation. Only small differences were found (see Fig. 5.3). Therefore, only the 10-year climatologies were used for the following analysis. The only exception are the lifetime estimates for CFC-12 in Section 6.4.

CHAPTER 3

Vertical velocity

Various coordinate systems can be used for the representation of the vertical dimension in meteorological models [*Kasahara*, 1974]. The two transport schemes that are investigated in this study use different vertical coordinate systems (see Sections 2.1 and 2.2). This implies that they contain different representations of the vertical velocity that is used for the tracer transport: In the FFSL transport scheme implemented in EMAC, the vertical velocity is calculated as a residual from the horizontal flux divergence using the continuity equation. Thus, in the EMAC-FFSL scheme, a *kinematic* vertical velocity representation is used. In contrast, in EMAC/CLaMS potential temperatures are used as the vertical coordinate in the stratosphere and vertical velocities are derived from diabatic heating rates. This is denoted *diabatic* vertical velocity.

This chapter describes the characteristics of each vertical velocity representation and presents an analysis of the differences between the kinematic and the diabatic vertical velocity in the EMAC model.

3.1 Diabatic vertical velocity in EMAC/CLaMS

In EMAC/CLaMS potential temperature is used as the vertical coordinate in the stratosphere. The vertical velocity $\dot{\theta}$ in this representation is derived from the diabatic heating rate Q:

$$\dot{\theta} = Q \frac{\theta}{T} \tag{3.1}$$

Here, diabatic heating rate means $Q = J/c_p$, where J is the diabatic heating rate per unit mass and c_p the specific heat capacity at constant pressure. Only through diabatic heating transport across isentropic surfaces can take place. The diabatic heating rate Q is the sum of radiative heating Q_{rad}, heating from diffusion and tubulent mixing Q_{diff} and heating from latent heat release Q_{lat}:

$$Q = Q_{\text{rad}} + Q_{\text{diff}} + Q_{\text{lat}} \tag{3.2}$$

The radiative heating Q_{rad} is the dominant term in the stratosphere, while in the tropopause region the latent heat release is also of importance [*Ploeger et al.*, 2010]. The contributions of the different terms to the diabatic heating rate in the ERA-Interim reanalysis are also investigated by *Fueglistaler et al.* [2009] and *Wright and Fueglistaler* [2013].

A diagnostic tool to capture the diabatic heating from the different process parameterisations in EMAC was implemented during this work. A slightly modified version of the tendency diagnostic of the ECHAM6 model [*Stevens et al.*, 2013] was used for this task (S. Rast, personal communication). The diagnostic reads the temperature before and after processes that cause diabatic heating and calculates temperature tendencies ΔT [K/s]. Let $\Delta T_-^{(i)}$ be the integrated temperature tendency over all processes before a certain process (i). The integrated temperature tendency after process (i) is denoted $\Delta T_+^{(i)}$. If temperature T at time t is changed by n different processes in the model time step Δt, then the temperature in the next time step $T(t + \Delta t)$ reads:

$$T(t + \Delta t) = T(t) + \Delta T_+^{(n)}(t)\Delta t \tag{3.3}$$

For $i = 1, ..., n - 1$ it holds that $\Delta T_+^{(i)} = \Delta T_-^{(i+1)}$. The tendency due to process (i) is denoted $\Delta T^{(i)}$ and calculated by

$$\Delta T^{(i)} = \Delta T_+^{(i)} - \Delta T_-^{(i)} \tag{3.4}$$

The temperature tendencies $\Delta T^{(i)}$ from all processes that cause diabatic heating are added up and the units are converted to K/day. The vertical velocity $\dot{\theta}$ is then determined by Eq. (3.1). In EMAC, the parameterisations for radiation, convection,

clouds, vertical diffusion, and gravity wave drag contribute to the total diabatic heating rate Q. Most of the processes mentioned above can not be resolved by the coarse model grid and have to be parameterised. However, subgrid parameterisations always imply a certain degree of inaccuracy. Different parameterisations of the same process deliver different results. E.g. the choice of the convection scheme influences the diabatic vertical velocity in the tropical tropopause region (TTL).

Figure 3.1 shows the annual zonal mean of the diabatic vertical velocity in EMAC using three different convection schemes. The figures focus on the TTL region, which is the crucial region for tropospheric air entering the stratosphere. Here, the vertical velocity is small compared to other regions of the atmosphere and small differences in upwelling have a large impact on the trace gas transport. Figure 3.1 shows the diabatic vertical velocity for the standard Tiedtke convection scheme [*Tiedtke*, 1989; *Nordeng*, 1994], the operational ECMWF convection scheme [*Tiedtke*, 1989; *Bechtold et al.*, 2004], and the Zhang-McFarlane-Hack (ZFH) convection scheme [*Hack*, 1994; *Zhang and McFarlane*, 1995]. All other process parameterisations are unchanged. The ECMWF convection leads to the strongest vertical upwelling in the tropics. The ZFH convection shows the weakest upwelling, and the strength of upwelling in the Tiedtke convection scheme is in between the other two convection schemes. Another difference is found in the strength of the transport barrier at the level of zero radiative heating at about 350 K. The Tiedtke and the ECMWF convection scheme lead to a strong barrier to vertical transport with an extensive layer of negative vertical velocities in the annual mean at 350 K. However, this transport barrier is not present throughout the year and thus upward transport into the stratosphere is not completely inhibited. In some seasons, there are regions with positive vertical velocities at this altitude. Further, in a model simulation, if the layer of negative vertical velocities is sufficiently thin, there could still be an exchange of tropospheric and stratospheric air through vertical numerical diffusion. The ZFH convection does not show the layer with negative vertical velocities extending throughout the tropics in the annual mean. Here, at 5°S and 5-10°N the annual mean has small positive values of the vertical velocity. Overall, there are clear differences in the TTL region using different convection schemes, with the Tiedtke and ECMWF convection showing stronger upwelling between 300 and 340 K and a more pronounced transport barrier at the level of zero radiative heating ($\approx$ 350 K) than the ZFH convection. The influence of choice of convection scheme in EMAC is analysed in detail in *Tost et al.* [2006]. The authors find that the tested convection schemes show varying skill levels for different aspects of the simulation. Thus they do not give a recommendation

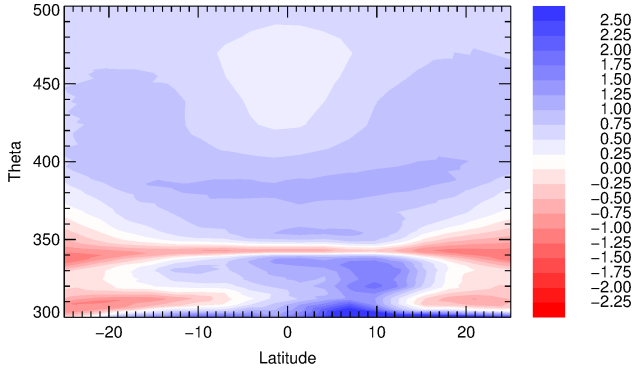

(a) Standard Tiedtke convection scheme

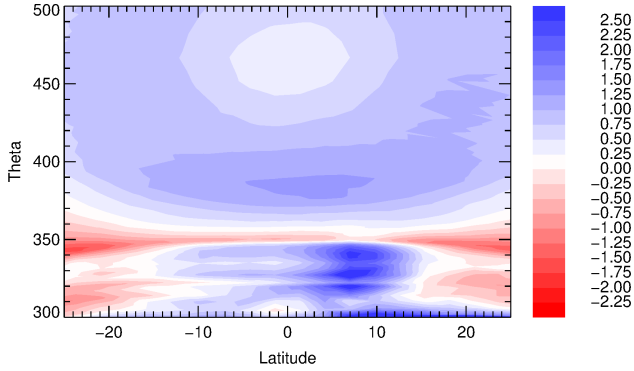

(b) ECMWF convection scheme

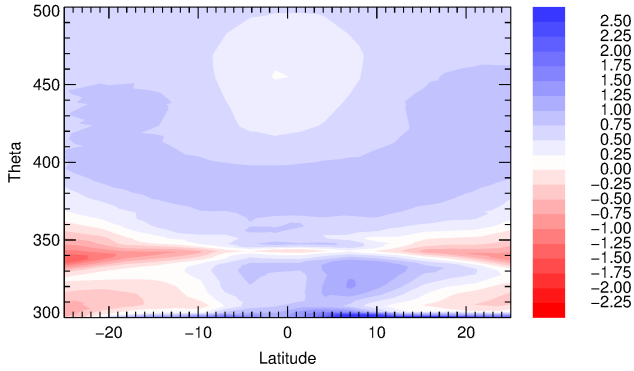

(c) ZFH convection scheme

Figure 3.1: Annual, zonal mean of diabatic vertical velocity $\dot{\theta}$ [K/day] in EMAC for the year 2005 using three different convection schemes (see text).

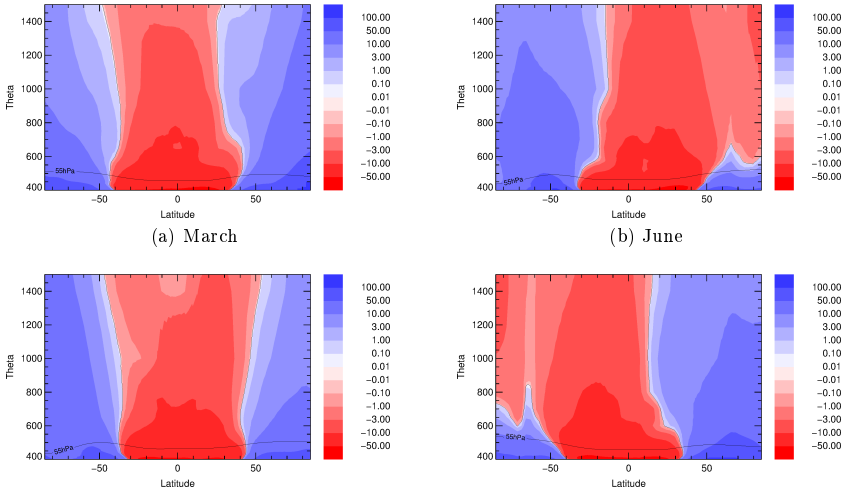

(a) March (b) June

(c) September (d) December

Figure 3.2: Diabatic vertical velocity $\overline{\omega}_\theta$ in [Pa/day] (converted from $\dot{\theta}$, see Sect. 3.4) for different months from the 10-year EMAC climatology.

for a specific convection scheme. In the present work, the Tiedtke parameterisation is used. The parameterisations of the other processes are also set to the standard EMAC configuration (see Appendix A).

In Fig. 3.2 the seasonal variation of the diabatic circulation is displayed by showing zonal mean diabatic vertical velocity of four months as an example for every season. The upwelling region of the diabatic circulation in the tropics (the so-called 'tropical pipe', see Sect. 4.1) follows a distinct annual cycle. It is always shifted toward the summer hemisphere. Thus, in boreal summer (June, Fig. 3.2b) there is upwelling throughout the Northern hemisphere above 700 K. Analogously, there is upwelling throughout the Southern hemisphere in December (Fig. 3.2d) above 800 K. This constitutes a realistic representation of the seasonal cycle of the Brewer-Dobson-Circulation [*Plumb and Eluszkiewicz*, 1999]. In the transition periods, i.e. autumn and spring (Figures 3.2a and 3.2c), there is downwelling in both hemispheres from mid-latitudes to the poles. The tropical pipe is located in the tropics. Above 600 K, the upwelling region is wider in September than in March. The figures of both months, March and September, display the transition of the maximum upwelling from the former summer hemisphere to the future summer hemisphere. E.g. in September, at high altitudes at 1400 K, the maximum upwelling is located at 25°N,

whereas in lower altitudes the maximum upwelling has already shifted to the future summer hemisphere at 5°S.

3.2 Kinematic vertical velocity in EMAC-FFSL

The standard vertical velocity in EMAC is derived from the spectral advection scheme in ECHAM5. The vertical wind $\dot{\eta}$ in ECHAM5 is calculated from the zonal and meridional horizontal winds using the continuity equation:

$$\frac{\partial}{\partial \eta}\left(\frac{\partial p}{\partial t}\right) + \nabla \cdot \left(\overrightarrow{v_h}\frac{\partial p}{\partial \eta}\right) + \frac{\partial}{\partial \eta}\left(\dot{\eta}\frac{\partial p}{\partial \eta}\right) = 0 \tag{3.5}$$

Here, η denotes the vertical hybrid σ-p coordinate in ECHAM5 [see *Roeckner et al.*, 2003]. $\overrightarrow{v_h}$ is the horizontal wind vector on an ECHAM5 model layer. After the advection time step, the new surface pressure is calculated for each grid box which determines the pressure levels of the hybrid model grid for the next time step.

This method implies fundamental problems since the horizontal wind speed in the atmosphere is much higher than vertical wind speed. As a result, small errors in the horizontal wind lead to large errors in the vertical wind. Vertical wind fields derived through the continuity equation often show very patchy structures. This known phenomenon is shown by e.g. *Schoeberl et al.* [2003] and *Ploeger et al.* [2011], although their results are also affected by assimilation effects.

Only the horizontal winds are input parameters for the FFSL tracer transport in EMAC. Horizontal tracer mass fluxes are derived using the horizontal wind field. The vertical velocity used in the tracer transport is derived with the continuity equation for the tracer (mass conservation) from the horizontal mass fluxes for individual model grid boxes. This vertical velocity in the tracer transport differs from the vertical velocity $\dot{\eta}$ from the wind field, since different advection schemes are used for the air-mass density and for trace gases: the spectral advection is used for air-masses, and the flux-form semi-Lagrangian transport [*Lin and Rood*, 1996] is used for the tracers. Each advection scheme uses its own grid and is internally mass-conservative, but re-mapping of trace gas distributions to the η-grid can produce inconsistencies. This phenomenon is investigated in detail by *Jöckel et al.* [2001].

Within the frame of this work, a diagnostic for the vertical velocities was developed and implemented in the EMAC flux-form semi-Lagrangian transport module. The diagnostic for the vertical velocity in the transport scheme is adapted from the Com-

munity Atmosphere Model (CAM) finite-volume dynamical core (implemented by C. Chen, described in *Lin* [2004]). The internal grid in the FFSL transport module differs from the η-grid in ECHAM5: it is variable in the vertical dimension and fixed in the horizontal dimensions. This concept is denoted as 'vertically Lagrangian' [*Lin*, 2004]. In each advection time step, horizontal mass fluxes through the lateral boundaries are calculated for each grid box. Through the advection the mass in each grid box changes and therefore also the thickness of each grid box in a pressure based vertical coordinate system. For the ω-diagostic the pressure at the layer interfaces before and after the advection is compared. The pressure in one grid box is influenced by the mass in the grid boxes above and by the horizontal mass fluxes into the grid box. This constitutes the vertically Lagrangian character of the advection scheme, since it shifts the pressure boundaries of the grid boxes. After the advection time step, the new surface pressure based on the new mass distribution in each column of the model grid is calculated. Then, a vertical remapping according to the η-levels defined by the new surface pressure takes place.

The differences between the vertical velocity from the horizontal winds in the spectral representation and the vertical velocity derived in the FFSL transport scheme are small but present. As an example, Fig. 3.3 shows vertical cross-sections of the kinematic vertical velocity ω for one day in April. This figure reveals the patchy structure of the kinematic vertical velocities. The fluctuations in the vertical velocities are slightly stronger in the spectral vertical wind field than in the FFSL scheme. The peak magnitudes of the updraft and downdraft are slightly weaker pronounced in the ω-distribution derived from the tracer transport scheme than in the ω-distribution from the spectral representation. One example for such a structure is located at 10°S at 800 K in the example shown in Fig. 3.3. Here, ω from the spectral representation shows stronger downdraft (indicated by deeper blue colour) than ω from the FFSL transport scheme.

The annual, zonal mean of the kinematic vertical velocity $\overline{\omega}$ (Fig. 3.4) shows only small differences between $\overline{\omega}$ from the spectral scheme and $\overline{\omega}$ from the gridpoint based FFSL transport scheme. The minimum in the tropical upwelling at 800 K above the equator is more pronounced using the spectral representation. All other parts of the zonal mean vertical velocity distributions in Fig. 3.4 are similar.

Considering the comparisons of the vertical velocity ω from the transport diagnostic to ω from the spectral representation, the differences are rather small. However, it is important to do this diagnostic instead of taking ω from the spectral representation without being sure that the differences between the kinematic vertical velocities

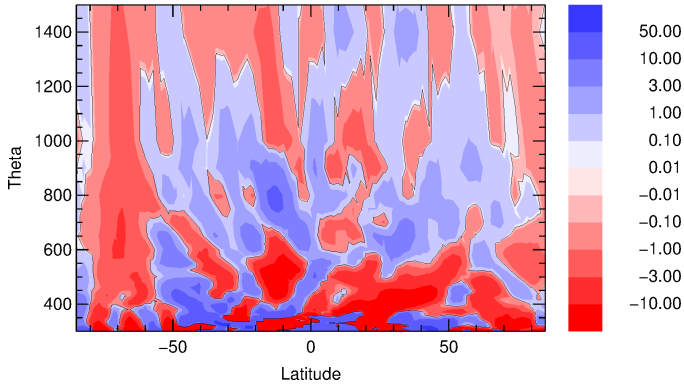

(a) ω from spectral winds

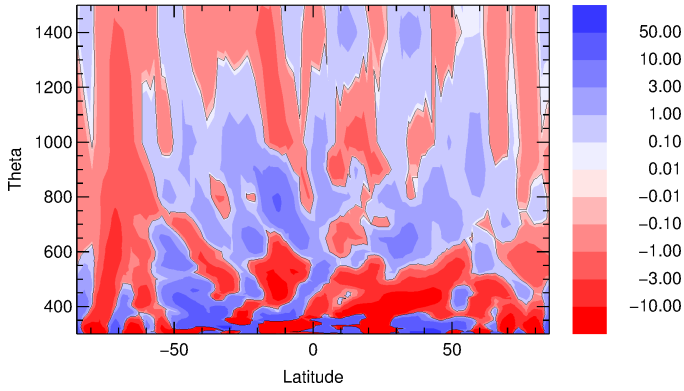

(b) ω from EMAC FFSL transport scheme

Figure 3.3: Cross-section of vertical velocity ω [hPa/day] at 50°E for the 8$^{\text{th}}$ April 2005 from EMAC. The top panel shows the vertical velocity derived from the horizontal wind field and the bottom panel shows the vertical velocity derived from horizontal mass fluxes in the FFSL transport scheme.

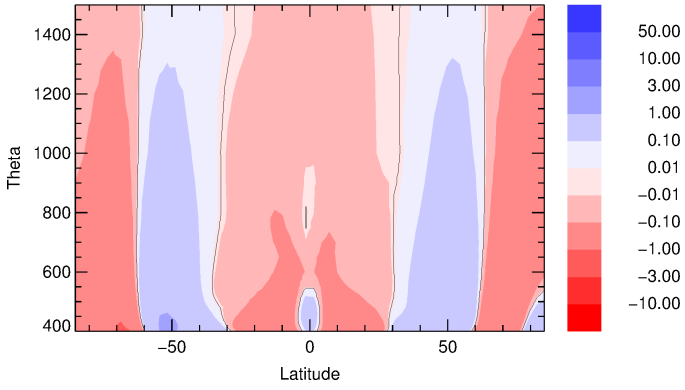

(a) $\overline{\omega}$ from spectral winds

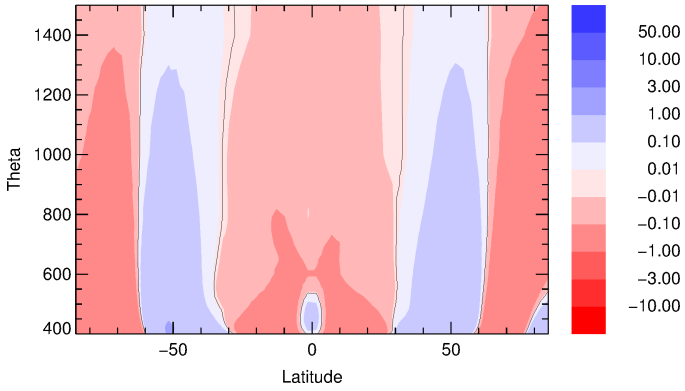

(b) $\overline{\omega}$ from EMAC FFSL transport scheme

Figure 3.4: Annual, zonal mean vertical velocity ω [hPa/day] for the 8th April 2005 from EMAC. The top panel shows the vertical velocity derived from the horizontal wind field and the bottom panel shows the vertical velocity derived from horizontal mass fluxes in the FFSL transport scheme.

from the different numerical schemes are not significant. In the following analysis the vertical velocity obtained from the new diagnostic in the transport scheme is used since this is the actual vertical velocity that causes vertical advection in the FFSL transport scheme.

3.3 Transformed Eulerian mean

The calculation of the Eulerian zonal mean $\overline{\omega}$ of the kinematic vertical velocity ω does not deliver a meaningful representation of the atmospheric circulation that is relevant for the trace gas transport. Planetary waves that propagate on isentropic surfaces modify $\overline{\omega}$ but do not cause net vertical transport. In this situation, calculating the Eulerian zonal mean of ω yields zonal mean upwelling and downwelling in different latitudes due to the planetary wave. A more detailed discussion of this phenomenon is given in *Brasseur et al.* [1999].

The transformed Eulerian mean (TEM) can be used instead of the Eulerian mean to avoid the misleading effects in the zonal mean vertical velocity. The idea of this transformation is to produce a similar picture as if the average vertical velocity was taken along planetary waves [e.g. *Andrews et al.*, 1987]. The TEM mean meridional velocity $\overline{v}^*$ and vertical velocity $\overline{w}^*$ are defined as follows:

$$\overline{v}^* = \overline{v} - \frac{1}{\rho_0}\frac{\partial}{\partial z}\left(\frac{\rho_0\,\overline{v'\theta'}}{\overline{\theta}_z}\right) \tag{3.6}$$

$$\overline{w}^* = \overline{w} + \frac{\partial}{\partial y}\left(\frac{\overline{v'\theta'}\cos\phi}{\overline{\theta}_z}\right) \tag{3.7}$$

Here, $\overline{v}$ denotes the Eulerian mean meridional velocity, $\overline{w}$ the Eulerian mean vertical velocity in log-pressure coordinates, $\overline{v'\theta'}$ the eddy heat flux, $\overline{\theta}$ the Eulerian mean potential temperature, subscript z denotes the partial derivative in the vertical ($\frac{\partial}{\partial z}$), and ϕ latitude. $\rho_0(z) \equiv \rho_s \cdot e^{-z/H}$ is the basic mass density with ρ_s denoting the mass density at the surface pressure p_0. The log-pressure height z is derived from pressure p through:

$$z = -H \cdot \ln\frac{p}{p_0} \tag{3.8}$$

In this study, surface pressure p_0 and scale height H were set to 1000 hPa and 7 km, respectively.

The circulation described by $\overline{v}^*$ and $\overline{w}^*$ is also called the residual mean circulation.

Figure 3.5 shows the zonal mean vertical velocity $\overline{w}$ and transformed Eulerian mean (TEM) vertical velocity $\overline{w}^*$ from EMAC for the year 2005. The zonal mean vertical velocity $\overline{w}$ in Fig. 3.5a features a pronounced downwelling in the 40 ° to 60 ° latitude region and an upwelling in the polar regions from 60 ° latitude to the poles in both hemispheres. This pattern is due to eddy flux divergences and the zonal mean $\overline{w}$ thus gives a very misleading picture. The TEM vertical velocity $\overline{w}^*$ in Fig. 3.5b represents the relevant circulation for zonal mean tracer transport. Here, the circulation shows downwelling throughout the entire extratropical stratosphere in the annual mean, as expected.

3.4 Comparison of diabatic and kinematic velocities

This section presents an analysis of the differences between the diabatic and kinematic vertical velocities in EMAC. For this comparison, both velocities have been converted to $\omega = \dfrac{Dp}{Dt}$. The kinematic vertical velocity $\overline{w}^*$ (defined in the log-pressure coordinate system and calculted in the TEM formalism) has been converted to $\overline{\omega}^*$ in pressure coordinates using the definition of the log-pressure height (Eq. 3.8):

$$\overline{\omega}^* = -\frac{\overline{w}^* \cdot p}{H} \tag{3.9}$$

In Eq. (3.9), p denotes the pressure of the model layer and H denotes the scale height. This conversion is only valid for model layers of constant pressure. The EMAC hybrid model layers are defined so that above about 55 hPa the pressure at the model layers is constant. Therefore, the 55 hPa isobar is plotted in Figs. 3.6 and 3.7 to indicate the region where the transformation from $\overline{w}^*$ to $\overline{\omega}^*$ is valid.

The diabatic vertical velocity $\dot{\theta}$ was converted to the respective velocity $\overline{\omega}_\theta$ in pressure coordintes by transforming the total derivative of θ in spherical coordinates:

$$\frac{D\theta}{Dt} = \frac{\partial\theta}{\partial t} + \frac{1}{r_E \cos\phi} u \frac{\partial\theta}{\partial\phi} + \frac{1}{r_E} v \frac{\partial\theta}{\partial\lambda} + \omega \frac{\partial\theta}{\partial p} \tag{3.10}$$

Here, λ denotes longitude and r_E the radius of the Earth. Solving Eq. (3.10) for ω leads to:

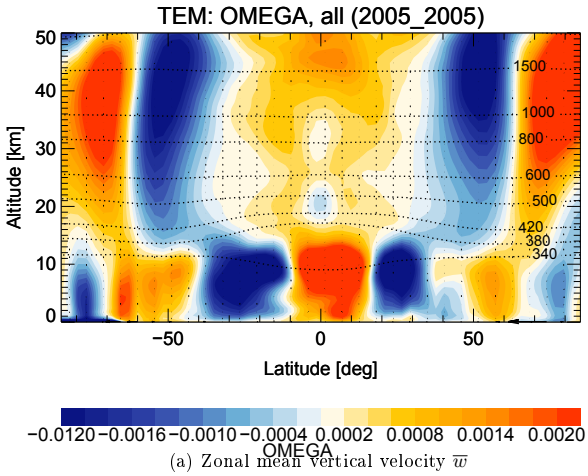

(a) Zonal mean vertical velocity $\overline{w}$

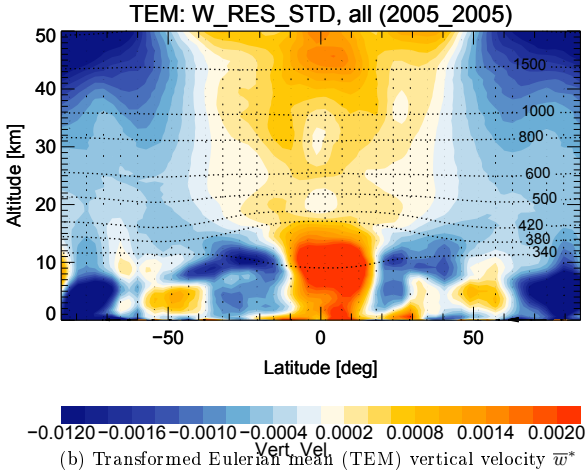

(b) Transformed Eulerian mean (TEM) vertical velocity $\overline{w}^*$

Figure 3.5: Annual, zonal mean vertical velocity $\overline{w}$ and transformed Eulerian mean (TEM) vertical velocity $\overline{w}^*$ [m/s] from EMAC for the year 2005. Dotted lines display potential temperature levels [K].

$$\omega_\theta = \frac{-\frac{\partial\theta}{\partial t} - \frac{1}{r_E\cos\phi}u\frac{\partial\theta}{\partial\phi} - \frac{1}{r_E}v\frac{\partial\theta}{\partial\lambda} + \dot{\theta}}{\frac{\partial\theta}{\partial p}} \tag{3.11}$$

Figure 3.6 shows the zonal mean of the diabatic vertical velocity $\overline{\omega}_\theta$ calculted from Eq. (3.11) and the kinematic vertical velocity $\overline{\omega}^*$ according to the TEM formulation in the 10-year EMAC simulation. The 10-year mean of both vertical velocity representations exhibits continuous upwelling at low latitudes and continuous downwelling at the higher latitudes and the polar regions. There are notable differences in the shape of the upwelling region (tropical pipe): The turnaround latitude in the NH of $\overline{\omega}^*$ is nearly constant with height, so that the tropical pipe in EMAC-FFSL is almost straight. It tends to be slightly wider in the Southern hemisphere at high altitudes than at SH lower altitudes. In contrast, the tropical pipe of the diabatic vertical velocity $\overline{\omega}_\theta$ has a different shape. It is wider than the upwelling region of $\overline{\omega}^*$ up to 700 K and narrower at higher altitudes. In the lower panel of Fig. 3.6 the turnaround latitudes can directly be compared to each other. At 1500 K the turnaround latitudes of the diabatic velocity are located at 40° latitude while they are found at 35° latitude in the kinematic velocity field. The upwelling around 500 K extends to higher latitudes in EMAC/CLaMS in both hemispheres, i.e. from 40°S to 42°N in $\overline{\omega}_\theta$ compared to 35°S to 37°N in $\overline{\omega}^*$. The upwelling is stronger in the diabatic vertical velocities in the latutude range between 30° and 40° in both hemispheres. EMAC-FFSL exhibits a minimum in the kinematic vertical velocity at 500 K over the equator. This pattern is also present in the ERA-Interim reanalysis [*Seviour et al.*, 2012] and in other climate models [*Butchart et al.*, 2006]. In higher altitudes, directly above the equator the mean kinematic vertical velocity $\overline{\omega}^*$ is lower than at 10° latitude. This is visible e.g. in the −3 Pa/day contour of $\overline{\omega}^*$ at 1300 K over the equator in Fig. 3.6b. The equatorial minimum is not seen in the 10-year mean in the diabatic vertical velocity pattern. The diabatic vertical velocity shows maximum values around 0° latitude and therefore stronger upwelling above the equator than the kinematic vertical velocity. In general, the circulation pattern is more uniform using diabatic vertical velocities. The kinematic vertical velocities exhibit more structures, even in the 10-year zonal mean, than the diabatic vertical velocity. In particular, the kinematic vertical velocity shows an equatorial minimum, a minimum in downwelling at 75°S and a minimum in upwelling at 30°N between 1000 and 1200 K. Above 800 K, the tropical pipe is wider in $\overline{\omega}^*$ than in $\overline{\omega}_\theta$ but the region of the strongest upwelling is narrower. This is indicated by the −3Pa/day

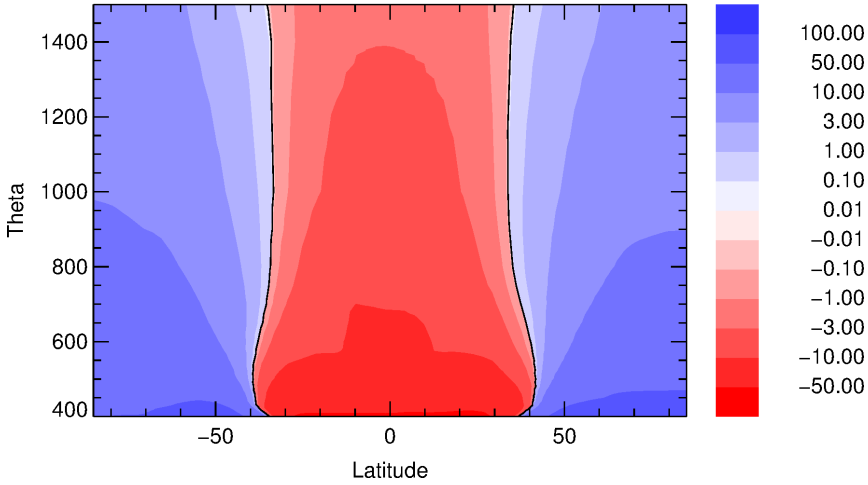

(a) Diabatic vertical velocity $\overline{\omega}_\theta$

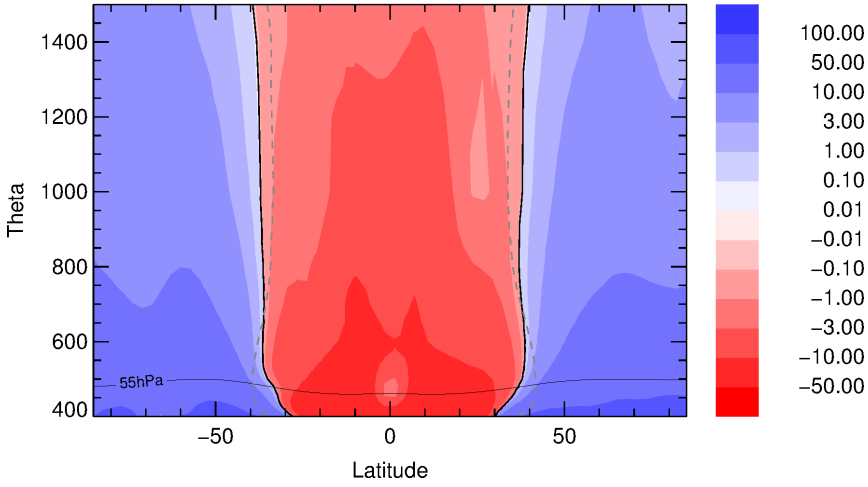

(b) Transformed Eulerian mean (TEM) vertical velocity $\overline{w}^*$

Figure 3.6: Vertical velocity $\overline{\omega}_\theta$ from diabatic heating rates and transformed Eulerian mean (TEM) vertical velocity $\overline{\omega}^*$ from 10 year EMAC climatology [Pa/day]. Solid black contours indicate the respective turnaround latitudes. Dashed grey lines in the bottom panel show the turnaround latitudes for $\overline{\omega}_\theta$ for comparison.

contour in Fig. 3.6. While this contour is nearly symmetric in the diabatic vertical velocity field, it has a maximum at 10°N in the kinematic representation. At lower altitudes at about 800 K, both velocity patterns show a maximum upwelling in the Southern hemisphere. This is a realistic representation of the diabatic circulation, since the maximum upwelling is observed during SH summer and NH winter, where strong wave activity is observed in the Northern hemisphere [*Randel et al.*, 2007]. The downwelling in the polar vortex regions is stronger using the diabatic vertical velocities. The 10 Pa/day contour is located at higher altitudes in $\overline{\omega}_\theta$ in the region from 60° latitude to the pole in both hemispheres.

Figure 3.7 presents $\overline{\omega}_\theta$ and $\overline{\omega}^*$ from the 10 year simulation climatology for each month. The seasonal cycle in the stratospheric circulation that was already shown in Fig. 3.2 is clearly visible in both vertical velocity representations. The most remarkable difference between the two transport schemes is the more uniform upwelling and downwelling of $\overline{\omega}_\theta$. This feature is more clearly visible in the monthly mean than in the annual mean, since the $\overline{\omega}^*$ is much more noisy in the monthly mean compared to the annual mean even when considering a 10-year climatology. The kinematic vertical velocity $\overline{\omega}^*$ exhibits several minima in the upwelling and downwelling regions which do not appear in the diabatic $\overline{\omega}_\theta$. The most pronounced minimum in the upwelling of $\overline{\omega}^*$ is located above the equator at 500 K. This minimum is visible in all seasons. In May to July and in December the mean values are even positive, which means downward transport above the equator in ω. At higher altitudes, the kinematic upwelling directly above the equator is also weaker than the surrounding upwelling at around 10°N or 10°S. In the diabatic vertical velocity field, the minimum at 500 K is barely visible. There is a hint of lower values at this location in the monthly means of $\overline{\omega}_\theta$ from May to July. In contrast to $\overline{\omega}^*$, maximum vertical velocities are located above the equator in several months in the diabatic representation, e.g. in October.

There are also other structures of weaker vertical velocity in the kinematic $\overline{\omega}^*$ velocity field. Minima in the downwelling regions are also present in the kinematic vertical velocity. In the SH polar region, a minimum in downwelling is visible from June to September throughout the whole altitude range of the stratosphere at 70°S. From June to August, this feature is also present in the diabatic vertical velocity field, but there the minimum is not so distinct and the downward vertical velocity is higher than in $\overline{\omega}^*$. In NH winter, the minimum vertical velocities are visible at high latitudes polewards from 80°N. This weaker downwelling occurs in the kinematic $\overline{\omega}^*$ from November to February. In the zonal mean of $\overline{\omega}_\theta$, the minimum at the pole is less pronounced and lasts only from December to January.

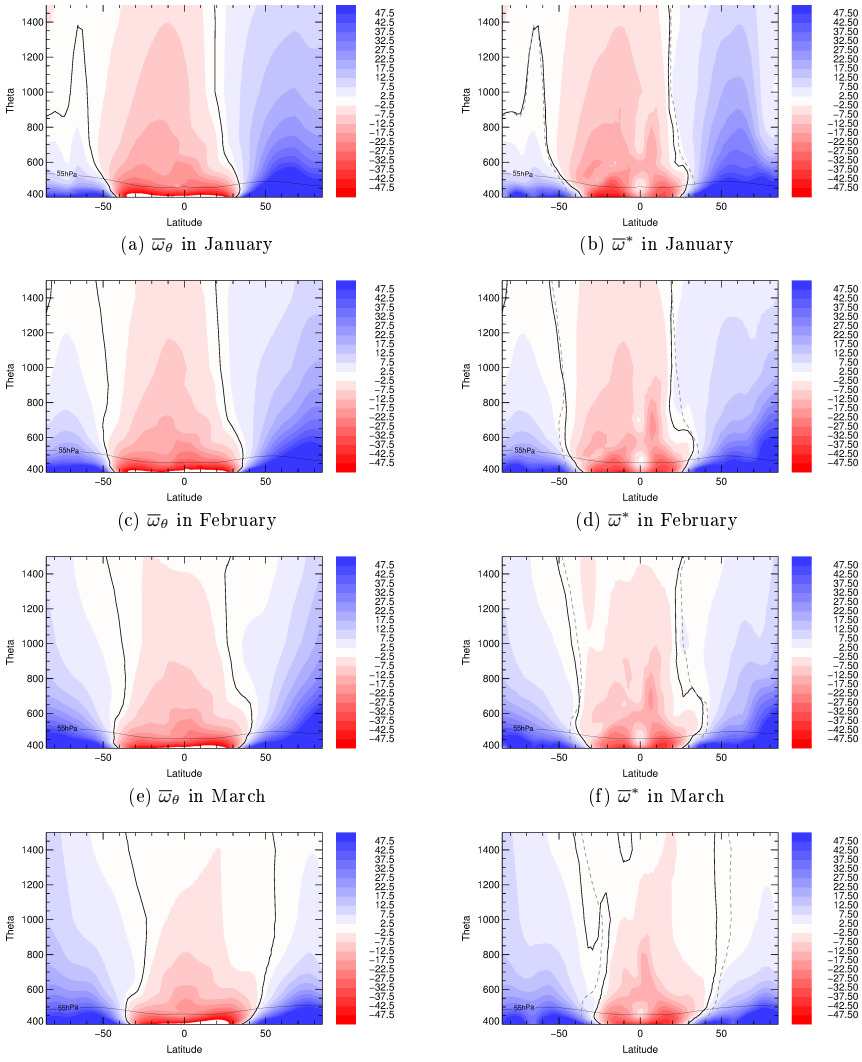

(a) $\overline{\omega}_\theta$ in January

(b) $\overline{\omega}^*$ in January

(c) $\overline{\omega}_\theta$ in February

(d) $\overline{\omega}^*$ in February

(e) $\overline{\omega}_\theta$ in March

(f) $\overline{\omega}^*$ in March

(g) $\overline{\omega}_\theta$ in April

(h) $\overline{\omega}^*$ in April

Figure 3.7: Vertical velocities $\overline{\omega}_\theta$ from diabatic heating rates and transformed Eulerian mean (TEM) vertical velocity $\overline{\omega}^*$ in [Pa/day] from the 10-year EMAC climatology. Dashed lines in the right panels for $\overline{\omega}^*$ show the turnaround latitudes for $\overline{\omega}_\theta$.

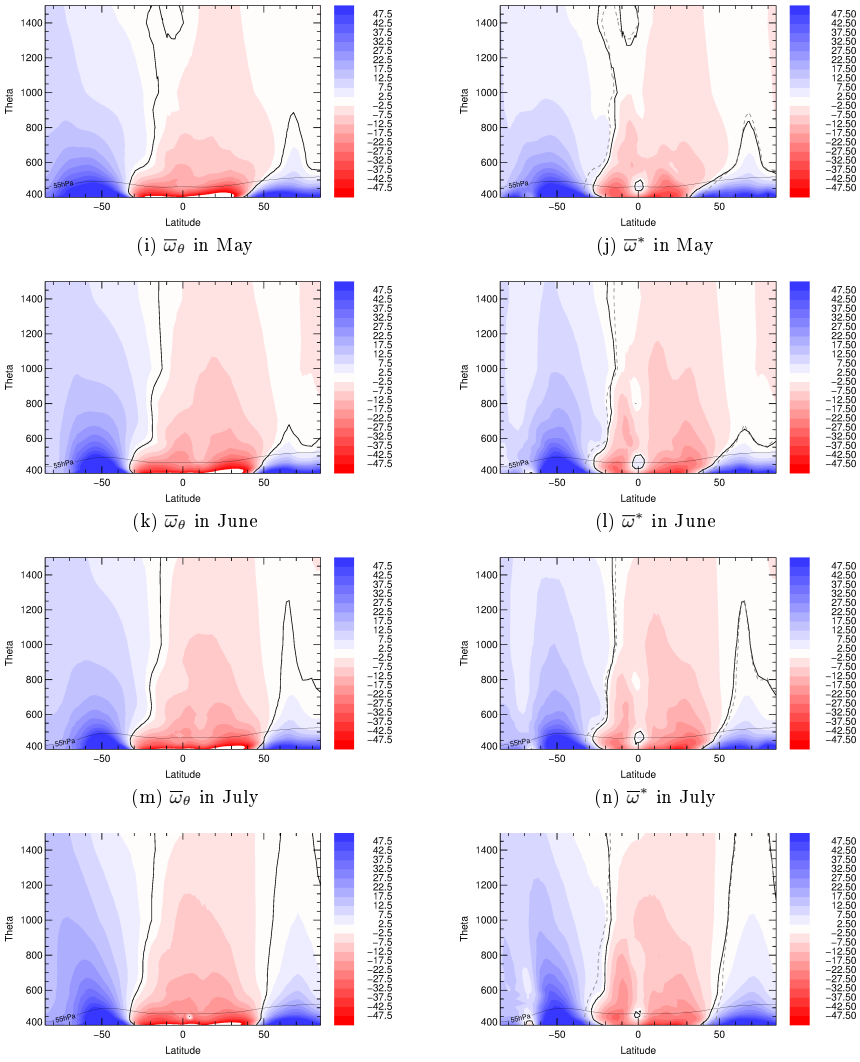

(i) $\overline{\omega}_\theta$ in May

(j) $\overline{\omega}^*$ in May

(k) $\overline{\omega}_\theta$ in June

(l) $\overline{\omega}^*$ in June

(m) $\overline{\omega}_\theta$ in July

(n) $\overline{\omega}^*$ in July

(o) $\overline{\omega}_\theta$ in August

(p) $\overline{\omega}^*$ in August

Figure 3.7: (Continued)

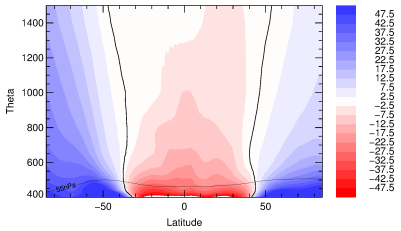

(q) $\overline{\omega}_\theta$ in September

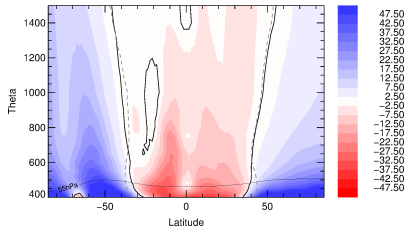

(r) $\overline{\omega}^*$ in September

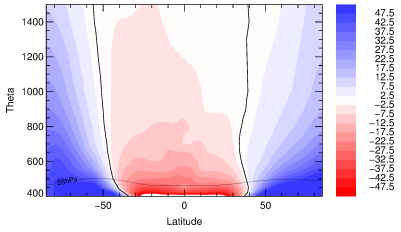

(s) $\overline{\omega}_\theta$ in October

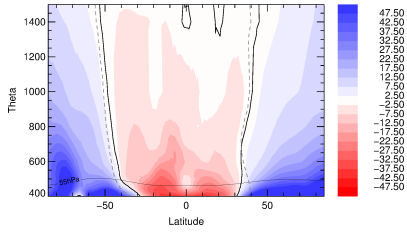

(t) $\overline{\omega}^*$ in October

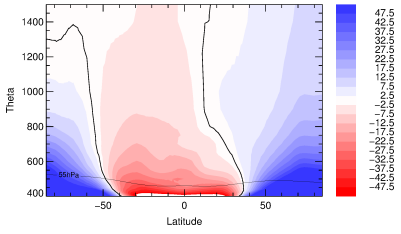

(u) $\overline{\omega}_\theta$ in November

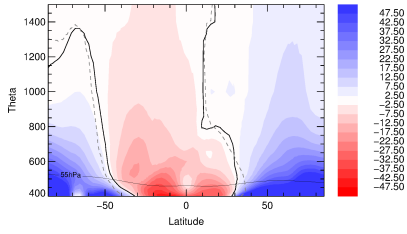

(v) $\overline{\omega}^*$ in November

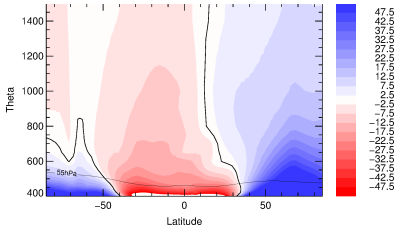

(w) $\overline{\omega}_\theta$ in December

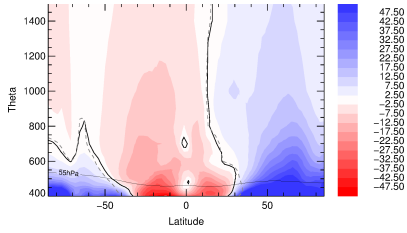

(x) $\overline{\omega}^*$ in December

Figure 3.7: (Continued)

In the regions around the addressed minima in the vertical velocity pattern of $\overline{\omega}^*$ noted above (e.g. Fig. 3.7d), the surrounding areas often show higher vertical velocities than the diabatic $\overline{\omega}_\theta$. One example for the upwelling regions is the monthly mean for February. In $\overline{\omega}^*$, there are higher vertical velocities around the equatorial minimum at 500 K than in $\overline{\omega}_\theta$. At higher altitude at 700 K around the second equatorial minimum, there are also high vertical velocities in $\overline{\omega}^*$. Here, the effect is most pronounced in the Northern hemisphere, where the kinematic upwelling is about 10 Pa/day higher than the diabatic upwelling.

Another difference that is clearly visible in the annual mean is the wider upwelling region of the diabatic $\overline{\omega}_\theta$ below 600 K. This feature is present in all monthly means throughout the year.

The movement of the upwelling region from one summer hemisphere to the future summer hemisphere is visible when considering the monthly mean. This transition happens at the same time of year in both vertical velocity representations. One important difference between the kinematic and the diabatic vertical velocity representation is illustrated in Fig. 3.8. This figure shows that the upwelling in SH summer (here: February) in the Southern hemispheric tropics is stronger using diabatic vertical velocities than when using kinematic vertical velocities. This difference in the vertical velocities has an impact on the simulated trace gas and age of air patterns (see Sect. 6.1).

The contour plot in Fig. 3.9 shows selected isolines of zonal mean upwelling velocities of the two transport schemes for July. It is clearly visible that the upwelling region in $\overline{\omega}^*$ is shifted northwards compared to the upwelling region of $\overline{\omega}_\theta$. The -5 Pa/day isoline reveals that the maximum upwelling region in EMAC-FFSL is shifted northwards by about 5° compared to EMAC/CLaMS. The -12 Pa/day isoline of the kinematic vertical velocity also exhibits a northward shift in the Northern hemispheric upwelling region. This shift has a large impact on trace gas distributions. Comparisons of trace gas distributions with measurement climatologies suggest that the location of the maximum upwelling of the diabatic vertical velocity fits better to the observed maximum that is visible through maximum trace gas distributions (see Sect. 4.1).

To summarize, the kinematic and the diabatic vertical velocities show roughly similar, realistic seasonal variations. The kinematic vertical velocity pattern are more noisy than the diabatic ones. Because the minima are surrounded by high vertical velocity patterns in the kinematic wind field, it is in some cases difficult to state whether

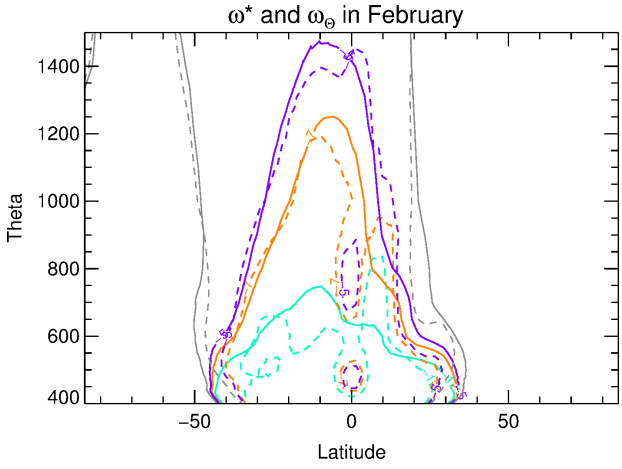

Figure 3.8: Vertical velocity for EMAC-FFSL ($\overline{\omega}^*$, dashed lines) and EMAC/CLaMS ($\overline{\omega}_\theta$, solid lines) for February in the 10-year climatology. Different contours for selected velocities are shown: 0 Pa/day (grey), −5 Pa/day (violet), −7 Pa/day (orange), and −12Pa/day (turquoise).

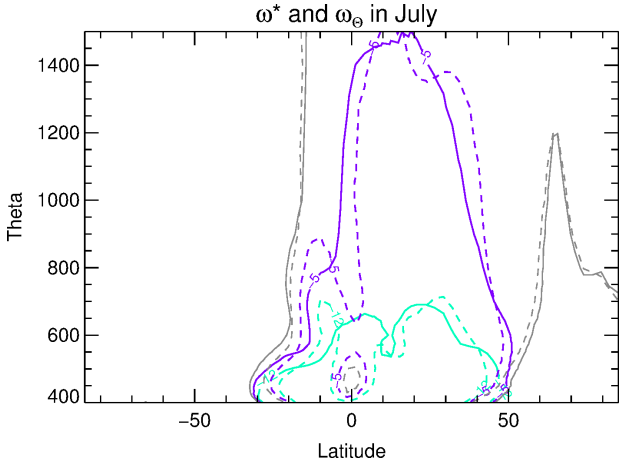

Figure 3.9: Vertical velocity for EMAC-FFSL ($\overline{\omega}^*$, dashed lines) and EMAC/CLaMS ($\overline{\omega}_\theta$, solid lines) for July in the 10-year climatology. Different contours for selected velocities are shown: 0 Pa/day (grey), −5 Pa/day (violet), and −12Pa/day (turquoise).

the total upwelling in the diabatic or in the kinematic representation is stronger. An accumulated effect of the different vertical velocities is visible in the age of air and trace gas distributions using different transport schemes. These distributions are analysed in detail in the next chapter.

CHAPTER 4

Tropical upwelling and subtropical jet

The upwelling region of the Brewer-Dobson-Circulation or diabatic circulation is located in the tropics and often referred to as 'tropical pipe' [*Plumb*, 1996]. The turnaround latitudes, i.e. the latitudes where the sign of the upwelling changes, form the Northern and Southern boundaries of the tropical pipe and show a distinct seasonal variation. The subtropical jet streams are located at the edges of the tropical pipe. Thus, the edges of the tropical upwelling region are transport barriers with limited mixing between tropics and extratropics. The strongest transport barrier is found in the winter hemisphere, when highest wind speeds occur in the jet stream. This chapter presents an analysis of the shape and location of the tropical upwelling region and its impact on trace gas distributions in the model simulation. The seasonal variation and the transport barriers at the boundary of the tropical pipe are also analysed.

4.1 N_2O in the tropical pipe

Chemical tracers with a tropospheric origin and a stratospheric sink show high concentrations in the tropical pipe compared to the concentrations outside the tropical pipe at the same altitude. Therefore their distributions can serve to characterise the tropical upwelling. Here, N_2O is used for this analysis. N_2O is a greenhouse gas that is produced in the troposphere. The atmospheric lifetime of N_2O is about 123

years [*SPARC*, 2013]. The N_2O emissions originate from both, natural sources and human activities. Most of the anthropogenic emissions are produced using fertilizers in agriculture. N_2O is depleted in the stratosphere and is today the most important ozone-depleting substance [*Ravishankara et al.*, 2009].

N_2O distributions from the simulation climatologies are compared to N_2O mixing ratios in monthly climatologies from measurements of the Microwave Limb Sounder (MLS) onboard the NASA Aura satellite. These satellite climatologies have been created from MLS version 3.3 data [*Livesey et al.*, 2011] for the years 2005 to 2012. The MLS data have been interpolated on vertical pressure levels for each profile, binned horizontally (lat $\times$ lon) and averaged for each month. MLS measures about 3500 profiles per day, thereby providing a high-frequency sampling of the global atmosphere and good statistics for creating global monthly climatologies.

Figures 4.1 and 4.2 show comparisons between modelled, climatological, horizontal N_2O distributions of EMAC-FFSL, EMAC/CLaMS, and a measurement climatology from MLS at 700 K for different seasons. The simulation and measurement climatologies show high N_2O mixing ratios in the tropics, due to upwelling of N_2O-rich air masses from the troposphere throughout the year. There are lower mixing ratios at mid-latitudes and the lowest concentrations occur in the polar vortex regions. In boreal winter (Fig. 4.1), the highest N_2O mixing ratios of 250 ppb at 700 K are located directly above the equator in the MLS climatology (Fig. 4.1c). This is captured well in the EMAC/CLaMS simulation (Fig. 4.1b). In EMAC-FFSL (Fig. 4.1a), the maximum N_2O mixing ratios are lower and lie about 240 ppb. Additionally, the location of maximum upwelling is slightly shifted Northwards in the EMAC-FFSL simulation results. In the extratropics in the Northern hemisphere, the EMAC/CLaMS simulation is in good agreement with the MLS measurements. However, EMAC-FFSL shows weaker gradients at the edges of the tropical pipe and the polar vortex than MLS and EMAC/CLaMS. In the Southern hemispheric extratropical regions, MLS N_2O mixing ratios range from 120 ppb to 130 ppb. The N_2O mixing ratios in EMAC/CLaMS show a good agreement with MLS in large parts of the Antarctic and are up to 10 ppb higher than MLS in the mid-latitude regions in the Southern hemisphere. On the contrary, EMAC-FFSL N_2O mixing ratios show a low-bias throughout the Southern hemisphere, where the N_2O mixing ratios are about 100 ppb in the simulation using the flux-form semi-Lagrangian transport scheme. This is consistent with the age of air distributions in the Southern hemisphere shown in Fig. 5.2. Here, EMAC-FFSL shows older air than EMAC/CLaMS in mid-latitudes in the Southern hemisphere which indicates that there is less horizontal mixing in EMAC-FFSL.

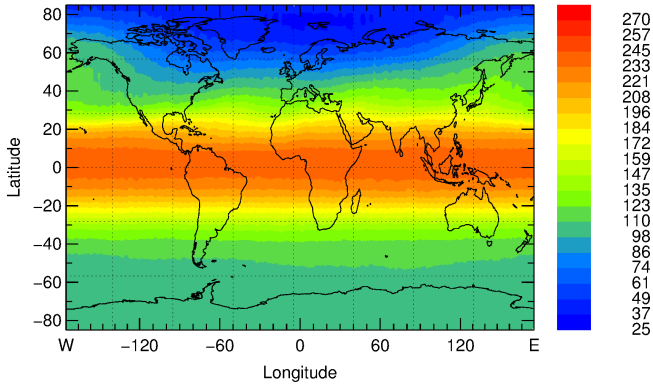

(a) EMAC-FFSL 10-year climatology

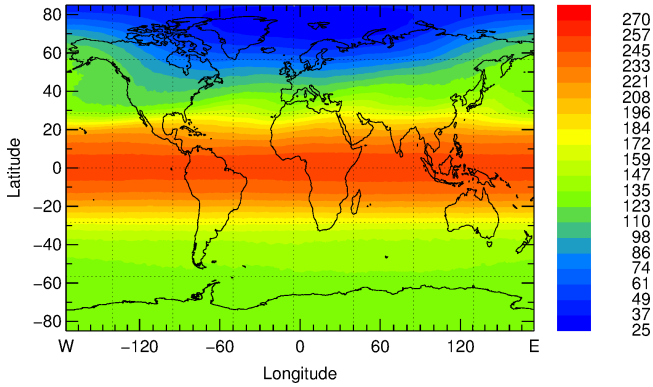

(b) EMAC/CLaMS 10-year climatology

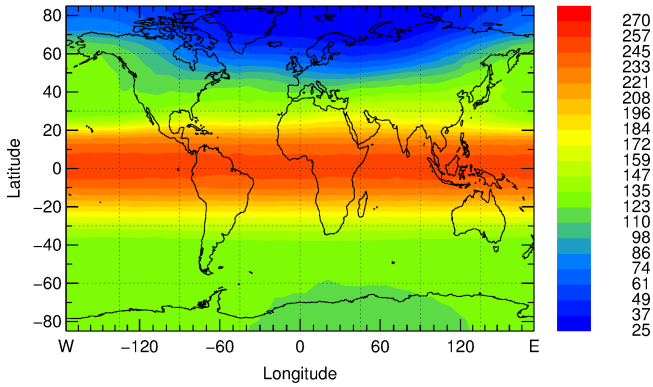

(c) MLS 2005-2012 climatology

Figure 4.1: Horizontal, climatological N_2O [ppb] distributions at 700 K for December to February from simulations (EMAC-FFSL and EMAC/CLaMS) and satellite measurements (MLS).

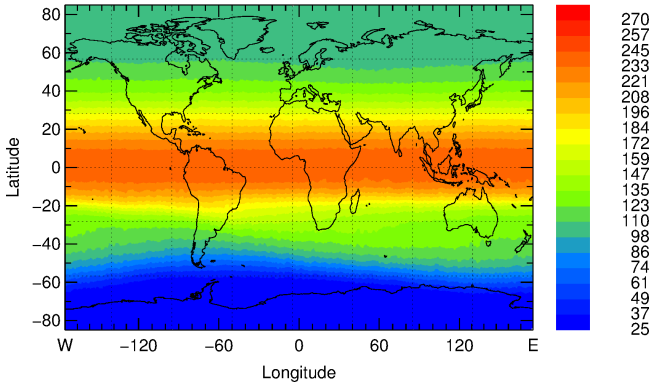

(a) EMAC-FFSL 10-year climatology

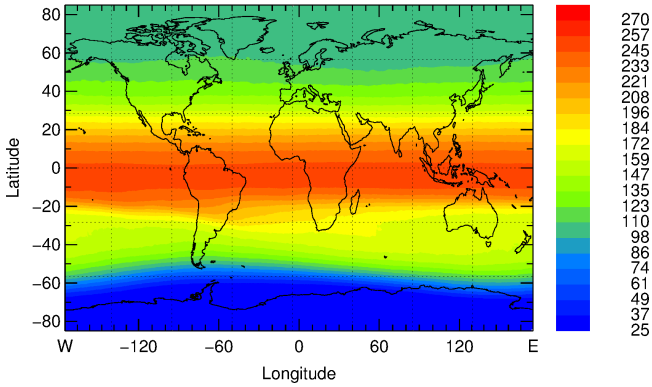

(b) EMAC/CLaMS 10-year climatology

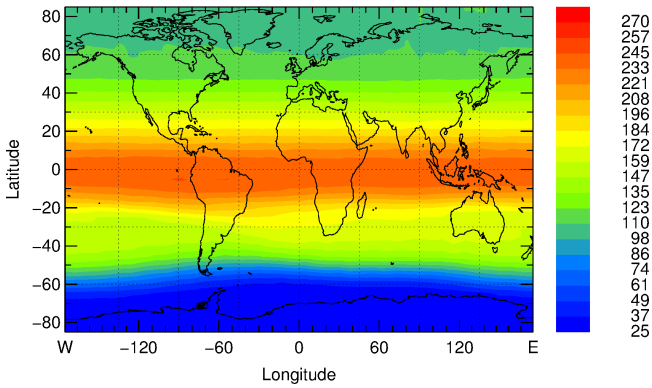

(c) MLS 2005-2012 climatology

Figure 4.2: Horizontal, climatological N_2O [ppb] distributions at 700 K for June to August from simulations (EMAC-FFSL and EMAC/CLaMS) and satellite measurements (MLS).

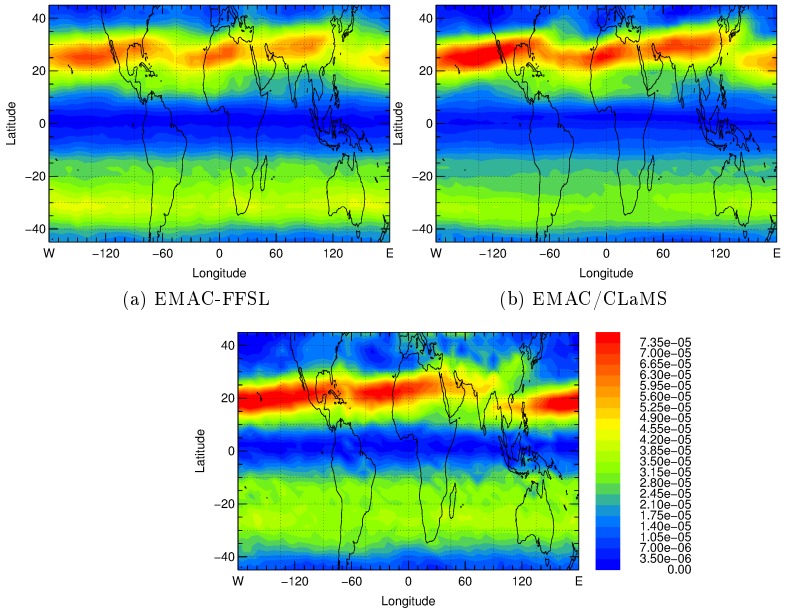

(a) EMAC-FFSL

(b) EMAC/CLaMS

(c) MLS 2005-2012 climatology

Figure 4.3: Meridional gradient of N_2O [ppb/m] at 700 K for February.

In boreal summer (Fig. 4.2), there is a good agreement in the peak N_2O mixing ratios of 240 ppb between EMAC-FFSL (Fig. 4.2a) and MLS (Fig. 4.2c). In this season, less mixing and stronger upwelling in EMAC/CLaMS (Fig. 4.2b) lead to maximum mixing ratios around 250 ppb and a more pronounced tropical pipe. The region of maximum upwelling in the MLS climatology is not located directly above the equator, but slightly shifted Southwards. The Southward shift is more pronounced in EMAC/CLaMS. In contrast, the tropical pipe is slightly shifted Northwards in EMAC-FFSL. In the extratropics of the Northern hemisphere, both models agree well with the MLS measurements in boreal summer. At mid and high latitudes in the Southern hemisphere, EMAC-FFSL N_2O mixing ratios are lower than those of MLS and EMAC/CLaMS.

Figures 4.3 and 4.4 display the absolute values of the meridional gradients of N_2O at the 700 K potential temperature surface. The N_2O gradients are shown for EMAC-FFSL, EMAC/CLaMS, and MLS for two months in different seasons. The upwelling in the tropical pipe results in a meridional gradient in the distributions of trace gases

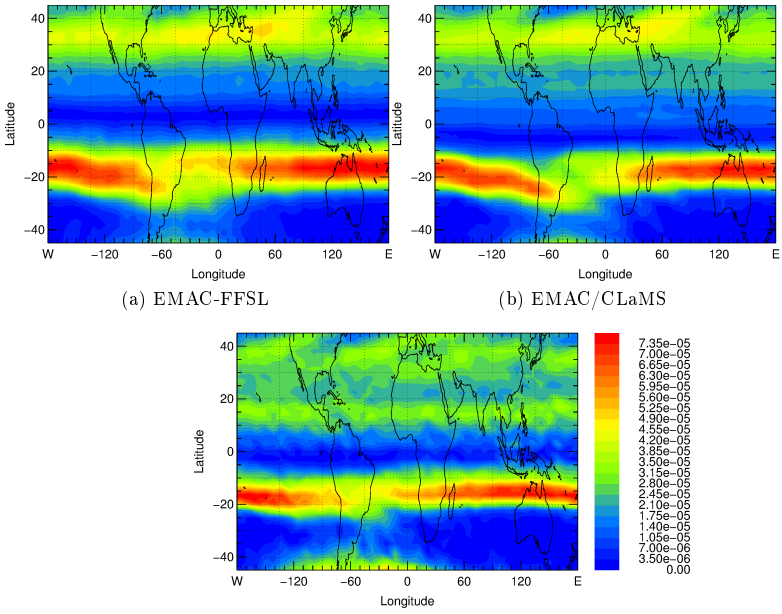

(a) EMAC-FFSL

(b) EMAC/CLaMS

(c) MLS 2005-2012 climatology

Figure 4.4: Meridional gradient of N_2O [ppb/m] at 700 K for September.

that are of tropospheric origin. The horizontal distribution of the tracer gradients gives information on the transport barrier at the edge of the tropical pipe: The magnitude and the location of the maximum gradient display the strength and location of the transport barrier, respectively. The strongest gradients occur in the winter hemisphere. These distinct gradients in the winter hemisphere are well represented in the EMAC/CLaMS simulation. The largest values are similar to the strongest N_2O gradients in the MLS climatology. The maximum N_2O gradients are located at 20°N in boreal winter (Fig. 4.3) and at 20°S in austral winter (Fig. 4.4). However, in EMAC-FFSL, the gradients are lower, especially in the Northern hemisphere in February (Fig. 4.3a).

In February, the gradients in the summer Southern hemisphere are stronger in EMAC-FFSL than in the MLS climatology which indicates that the horizontal mixing is too weak in this simulation. In contrast, EMAC/CLaMS shows a weaker gradient compared to the observations. In September, the N_2O gradients in the Northern hemisphere of both model climatologies are stronger than the gradient in the MLS climatology. Here, the overestimation is stronger in EMAC-FFSL. Thus, the EMAC-FFSL transport does not always underestimate the tracer gradients. In cases of weak gradients in the summer hemisphere, EMAC-FFSL results show gradients that are too strong.

In both modelled climatologies, the tropical pipe is wider than in MLS observations. Figure 4.4a clearly shows the Northward shift of EMAC-FFSL. The maximum upwelling is indicated by the region with the lowest meridional gradient, which is located North of the equator in EMAC-FFSL and slightly South of the equator in EMAC/CLaMS and MLS. These differences can be related to the vertical velocities that are used in the two transport schemes (Sect. 3.4).

Overall, the simulations show a good representation of the tropical pipe and the transport barriers at its Northern and Southern edges. One of the main differences between EMAC-FFSL and EMAC/CLaMS is the maximum value of N_2O in the tropics, which is higher in EMAC/CLaMS. Thereby, EMAC/CLaMS fits better to MLS in boreal winter, and EMAC-FFSL fits better in boreal summer. The location of the tropical pipe is better represented in EMAC/CLaMS. At the egdes of the tropical pipe, the lower gradients in the summer hemisphere as well as the maximum gradients in the winter hemisphere are improved using the Lagrangian transport scheme in EMAC/CLaMS.

4.2 The quasi-biannual oscillation (QBO)

The Brewer-Dobson-Circulation is modulated by the quasi-biannual oscillation (QBO) that induces a secondary meridional circulation [e.g., *Punge et al.*, 2009; *Flury et al.*, 2013]. The different phases of the QBO manifest in a reversion of the mean zonal wind in the tropics. Easterly and westerly wind regimes propagate downwards with a mean period of 28 months. The maximum amplitude of the QBO is located at about 20 hPa. The characteristics and implications of the QBO are reviewed by e.g. *Baldwin et al.* [2001].

The QBO is well represented in EMAC, if the model is run in the middle atmosphere (MA) mode with a high vertical resolution, i.e. 90 vertical levels up to 0.01 hPa ($\approx$80 km). This has been tested with ECHAM/MESSy1 by *Jöckel et al.* [2006] for the same resolution (T42L90MA) that is used for the present work. The QBO has also been evaluated for ECHAM/MESSy2 [see supplement of *Jöckel et al.*, 2010]. In the EMAC model, there is the possibility to nudge the QBO pattern towards observations. In the studies mentioned above, QBO-nudging was performed only in the first year for initialisation. From the second year of simulation, the model was able to simulate a realistic QBO pattern without nudging. In this work, no QBO-nudging was performed. In this way, the free-running simulation can not be compared exactly to observations in a given year, but the year-to-year variability in the tropical wind field is represented correctly.

The time evolution of the tropical zonal wind between 5°S and 5°N in EMAC is displayed in Fig. 4.5. This figure shows the characteristic downwelling pattern of the QBO phases. The easterly phases are more pronounced than the westerly phases. At high altitudes, another ocsillation pattern, namely the mesospheric semi-annual oscillation (SAO) with a period of about 6 months is visible. The SAO is most pronounced at about 1 hPa and propagates down to about 5 hPa.

The QBO influences the stratospheric trace gas distributions. The easterly phase of the QBO is associated with enhanced tropical upwelling and therefore positive anomalies of trace gases with tropospheric origin [*Punge et al.*, 2009; *Flury et al.*, 2013]. The SAO also modulates trace gas distributions [*Randel et al.*, 1998; *Jackson et al.*, 1998]. Trace gas anomalies have been calculated by subtracting the climatological monthly mean mixing ratio from the respective 10-year simulation climatology for each tracer from the current monthly mean mixing ratio in each vertical level. Figure 4.6 displays time series of trace gas anomalies in the tropics at the latitude range from 10°S and 10°N. These time series are analysed for the species N_2O, CFC-11,

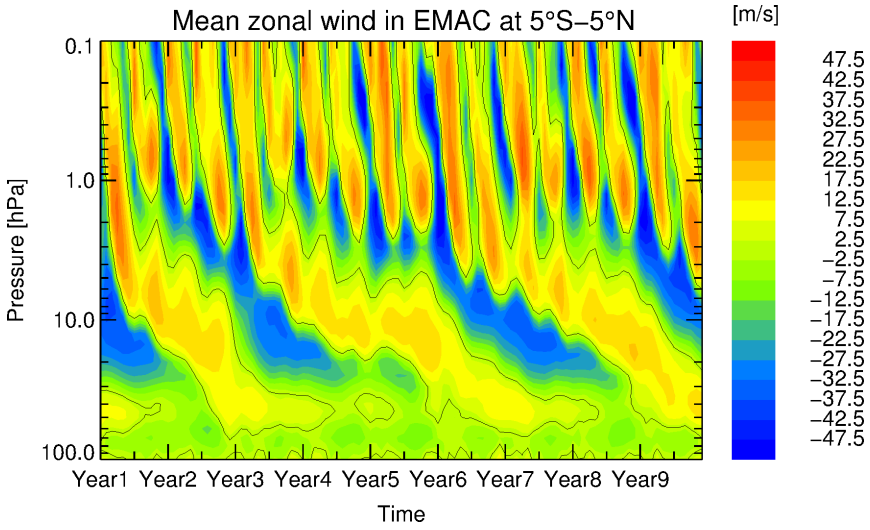

Figure 4.5: Simulated zonally averaged zonal wind [m/s] in EMAC in the tropics at the latitude range between 5°S and 5°N. Negative values denote easterly QBO phases, while positive values indicate westerly winds.

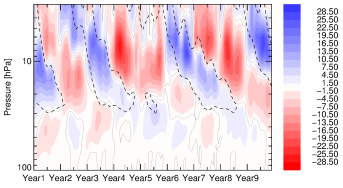

(a) EMAC-FFSL N_2O [ppb]

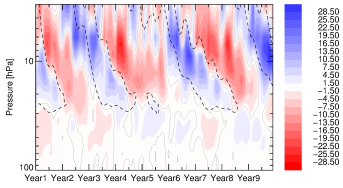

(b) EMAC/CLaMS N_2O [ppb]

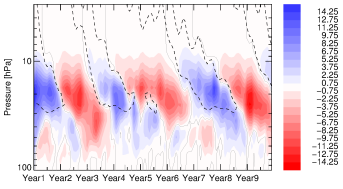

(c) EMAC-FFSL CFC-11 [ppt]

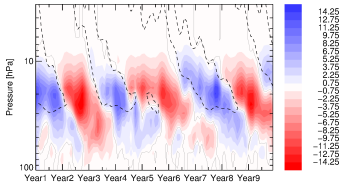

(d) EMAC/CLaMS CFC-11 [ppt]

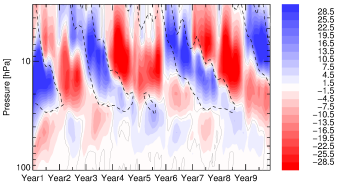

(e) EMAC-FFSL CFC-12 [ppt]

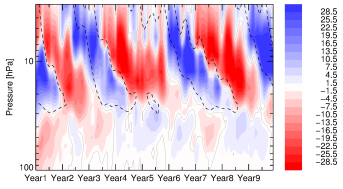

(f) EMAC/CLaMS CFC-12 [ppt]

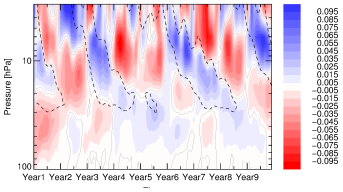

(g) EMAC-FFSL CH_4 [ppm]

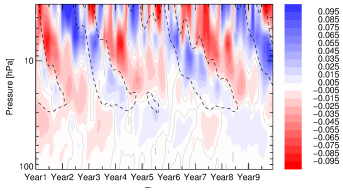

(h) EMAC/CLaMS CH_4 [ppm]

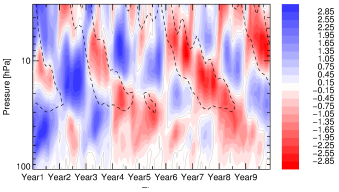

(i) EMAC-FFSL age of air [months]

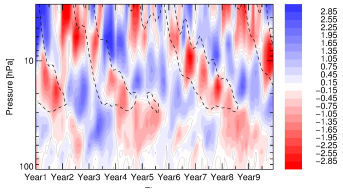

(j) EMAC/CLaMS age of air [months]

Figure 4.6: Simulated trace gas and age of air anomalies due to QBO in EMAC. This figure shows the anomalies compared to the 10-year climatological mean for N_2O, CFC-11, CFC-12, CH_4, and age of air. Left panels show results from EMAC-FFSL, right panels show results from EMAC/CLaMS. The easterly phase of the QBO is indicated by dashed isolines at $-15\frac{\mathrm{m}}{\mathrm{s}}$.

CFC-12, and CH_4 for EMAC/CLaMS and EMAC-FFSL. In Fig. 4.6, the QBO easterly phases are indicated by an isotach at $-15\frac{\mathrm{m}}{\mathrm{s}}$. The anomalies of all trace gases in both transport schemes follow the QBO pattern of the model. This behaviour is expected in a consistent simulation. Positive anomalies occur during the easterly phase and negative anomalies during the westerly phase of the QBO. The amplitudes of the trace gas variations are similar in both transport schemes. The variations in CFC-11 are not visible above 10 hPa due to too low CFC-11 mixing ratios at high altitudes. The other trace species depict the variability of the SAO at high altitudes above 7 hPa. The SAO pattern itself can not be seen in this figure, since this oscillation shows the same seasonal cycle every year and the anomalies here have been calculated as a difference from the monthly climatological mean. Figures 4.6i and 4.6j show the variation in mean age of air due to the QBO in EMAC-FFSL and EMAC/CLaMS, respectively. In contrast to the chemical tracers, the easterly QBO phases are associated with negative anomalies in age of air, since enhanced upwelling leads to younger air in the tropical pipe during the easterly wind regime.

Thus, the examination of the QBO pattern in EMAC and its influence on trace gas transport delivers consistent results. It is shown that this variation of the stratospheric circulation is well represented in the EMAC model. There are no significant differences in the QBO pattern between the two transport schemes EMAC/CLaMS and EMAC-FFSL.

4.3 Subtropical jet and extratropical tropopause

The extratropical lowermost stratosphere region is separated from the tropopause by two boundaries: the extratropical tropopause and the subtropical jet stream. These boundaries act as transport barriers and allow only limited in-mixing of tropospheric air masses into the lowermost stratosphere region. The transport barriers cause strong gradients in the trace gas distributions: a vertical gradient at the tropopause and a horizontal gradient at the subtropical jet.

Because of the high variability and the wavy structure of the jet stream the zonal mean is not a suitable perspective to examine the subtropical transport barrier. The height of the tropopause is also variable. Thus, the trace gas gradients are strongly smoothed in the zonal mean. Therefore, vertical, meridional cross-sections of single days of the simulation are shown in this section to analyse the strength of the transport barriers in the two transport schemes EMAC-FFSL and EMAC/CLaMS.

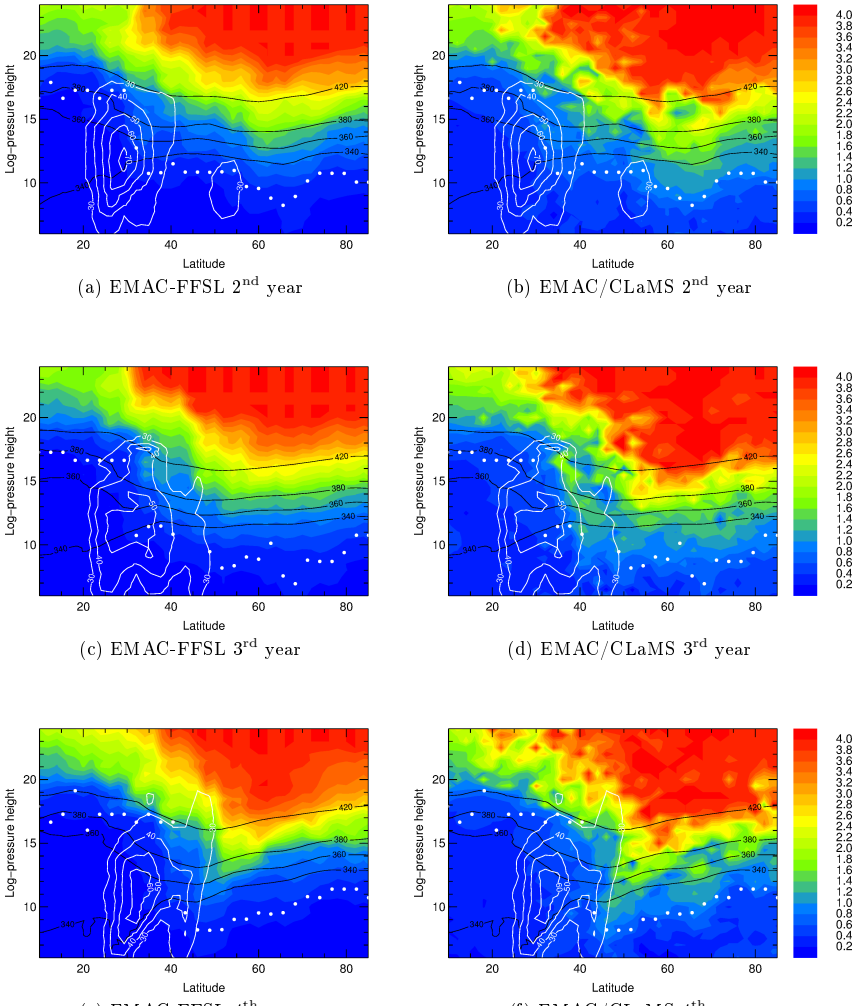

(a) EMAC-FFSL 2nd year

(b) EMAC/CLaMS 2nd year

(c) EMAC-FFSL 3rd year

(d) EMAC/CLaMS 3rd year

(e) EMAC-FFSL 4th year

(f) EMAC/CLaMS 4th year

Figure 4.7: Age of air in the lowermost stratosphere from EMAC-FFSL and EMAC/CLaMS at 120°E in the Northern hemisphere at the 15th December for different years in the simulation. Black lines show potential temperature levels [K] and white contours indicate zonal wind in the subtropical jet regions $[\frac{\mathrm{m}}{\mathrm{s}}]$. White dots indicate the thermal tropopause.

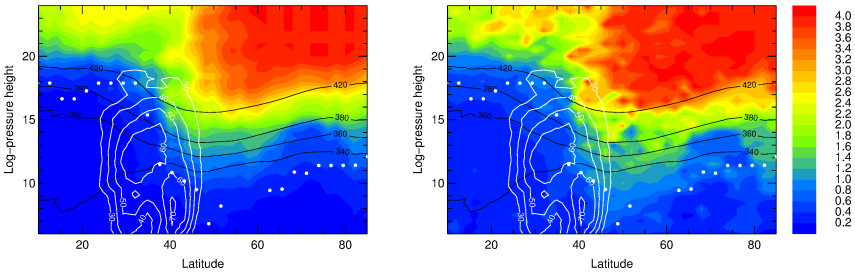

(g) EMAC-FFSL 5$^{\text{th}}$ year (h) EMAC/CLaMS 5$^{\text{th}}$ year

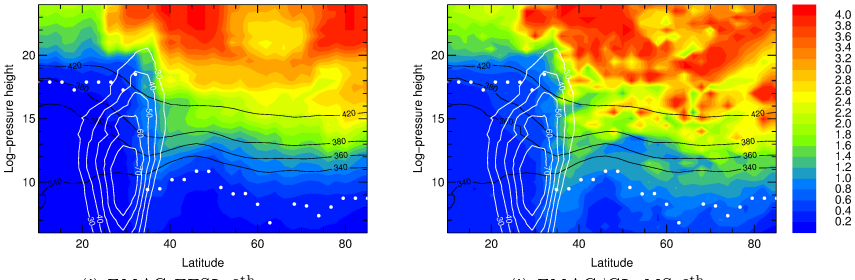

(i) EMAC-FFSL 6$^{\text{th}}$ year (j) EMAC/CLaMS 6$^{\text{th}}$ year

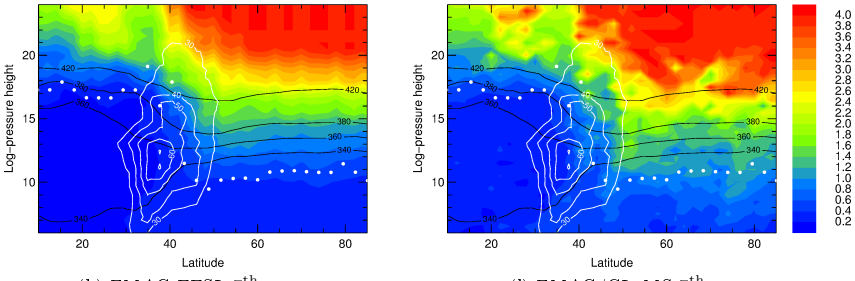

(k) EMAC-FFSL 7$^{\text{th}}$ year (l) EMAC/CLaMS 7$^{\text{th}}$ year

Figure 4.7: (Continued)

Vertical cross-sections at 120°E for the Northern hemisphere are presented in Fig. 4.7. In this region over Asia the jet stream is very strong in Northern hemispheric winter. The plots of Fig. 4.7 have been produced by interpolating EMAC-FFSL and EMAC/CLaMS age of air onto the same 2-dimensional vertical regular grid with a resolution of 2° in longitudinal and 0.5 km in vertical direction. In the case of EMAC-FFSL, age of air values of the gridpoints of one meridional layer in the EMAC grid closest to 120°E were selected. In the case of EMAC/CLaMS, all Lagrangian air parcels are chosen that are situated in the longitude range of 120°E $\pm\frac{1}{2}\Delta\lambda$ (with $\Delta\lambda$ denoting the extent of the EMAC gridboxes in longitudinal direction). In Figure 4.7, the interpolated age of air distibutions for EMAC-FFSL and EMAC/CLaMS are shown for one day in December for six different years of the simulation. To illustrate the locations of the transport barriers, the subtropical jet stream and the thermal tropopause are also shown in this figure.

The age of air tracer is chosen for this diagnostic since it is a passive tracer and displays only the transport characteristics without the influence of chemical change. Figure 4.7 identifies clear differences in the age of air patterns of EMAC-FFSL and EMAC/CLaMS in the lowermost extratropical stratosphere.

The transport barrier at the jet stream is more pronounced in the age of air distributions derived with the Lagrangian transport scheme in EMAC/CLaMS. This is visible in all examples in Fig. 4.7, independently of the strength of the jet stream. In the third year of the simulation (Figs. 4.7c, 4.7d) the jet stream is not as strong as in the other years with a maximum wind speed of less than 60 $\frac{\mathrm{m}}{\mathrm{s}}$. In EMAC/CLaMS, there is a distinct step in the age of air isolines at the subtropical jet. The contour line denoting the age of one year runs almost vertical in the region of the jet in EMAC/CLaMS. In contrast, the transition from the tropical to the subtropical age of air pattern is less abrupt in EMAC-FFSL. An example for a very strong subtropical jet is shown in Figs. 4.7i and 4.7j. Here, the maximum velocity in the zonal wind is more than 70 $\frac{\mathrm{m}}{\mathrm{s}}$. At this day, the jet region is very narrow and centred at 30°N. In both transport schemes, the strong transport barrier dominates the shape of the age of air cross-section. The difference between EMAC-FFSL and EMAC/CLaMS is not as large as in the cases of a weaker jet stream, but there is still a more pronounced transport barrier in EMAC/CLaMS than in EMAC-FFSL. Figures 4.7i and 4.7j show that at 35°N directly North of the jet old stratospheric air can penetrate down to the tropopuase in EMAC/CLaMS, whereas in EMAC-FFSL the air is much younger at this location and shows tropospheric characteristics. The Lagrangian transport scheme in EMAC/CLaMS is well suited for the transport in the jet region

since the Lagrangian air parcels move within the jet stream. Only a well determined amount of mixing takes place at the edges of the jet stream due to wind shear (see Sect. 2.1.2).

At the extratropical tropopause, there is again a stronger gradient present in EMAC/CLaMS than in EMAC-FFSL. One example is shown in Figure 4.7b. The effect is clearly visible at latitudes polewards of 60°N. In EMAC/CLaMS the vertical gradient of age of air in the altitude range from the tropopause up to 400 K is much stronger than in EMAC-FFSL (Fig. 4.7a).

The EMAC/CLaMS age of air cross-sections in Fig. 4.7 show the expected appearance of a tracer that was transported with a full-Lagrangian transport scheme. The overall age of air pattern is more structured in EMAC/CLaMS, as there are often small, separated fragments of young air visible in the lowermost stratosphere in EMAC/CLaMS, whereas in EMAC-FFSL the age of air pattern is more smooth without small filaments.

Overall, the stronger transport barriers in EMAC/CLaMS lead to a difference in age of air of about 0.5 years in the lower part of the stratosphere in the Northern hemisphere. It is not possible solely based on the age of air results to distinguish whether the young air in EMAC-FFSL has been diffused through the extratropical tropopause or has passed the jet stream and spread on the isentropic surfaces. It is assumed that both transport barriers are weaker in EMAC-FFSL and thus allow more air to cross the stratospheric boundaries.

CHAPTER 5

Representation of polar vortices

This section presents a comparison of the representation of the Arctic and Antarctic polar vortices in the two transport schemes. The edge of the polar vortex forms a strong transport barrier in the stratosphere [e.g., *Steinhorst et al.*, 2005; *Günther et al.*, 2008]. Inside the vortex, diabatic descent of airmasses from high altitudes leads to low concentrations of trace gases which are of tropospheric origin and have a stratospheric sink [e.g., *Müller et al.*, 1996]. These isolated conditions are crucial for polar ozone depletion. However, the simulation of a highly isolated vortex is a difficult task for climate models with limited spatial resolution. *SPARC* [2010] show that many CCMs do not form a sufficiently isolated Antartic polar vortex and that this problem is often even more pronounced for Arctic conditions.

When comparing the model performance in the case of vortex isolation against observations, it is important to assess the quality of the simulated horizontal wind. Therefore, before validating the transport schemes, the mean zonal wind in EMAC is compared with the mean zonal wind in ERA-Interim in Fig. 5.1. It is found that ERA-Interim zonal winds are slightly stronger in the winter hemisphere polar jet regions. Thus the polar vortex is weaker in EMAC than in ERA-Interim and the trace gas gradients are also expected to be moderately weaker in the simulation results compared to satellite climatologies, independently of the employed the transport scheme.

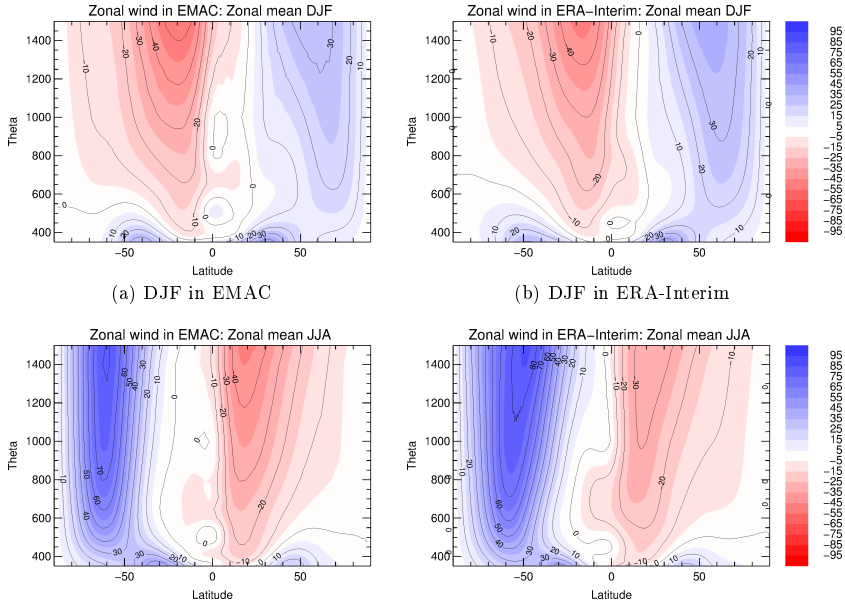

(a) DJF in EMAC (b) DJF in ERA-Interim

(c) JJA in EMAC (d) JJA in ERA-Interim

Figure 5.1: Zonal mean of zonal wind [m/s] from ERA-Interim climatology and EMAC climatology for NH winter (top panels) and SH winter (bottom panels).

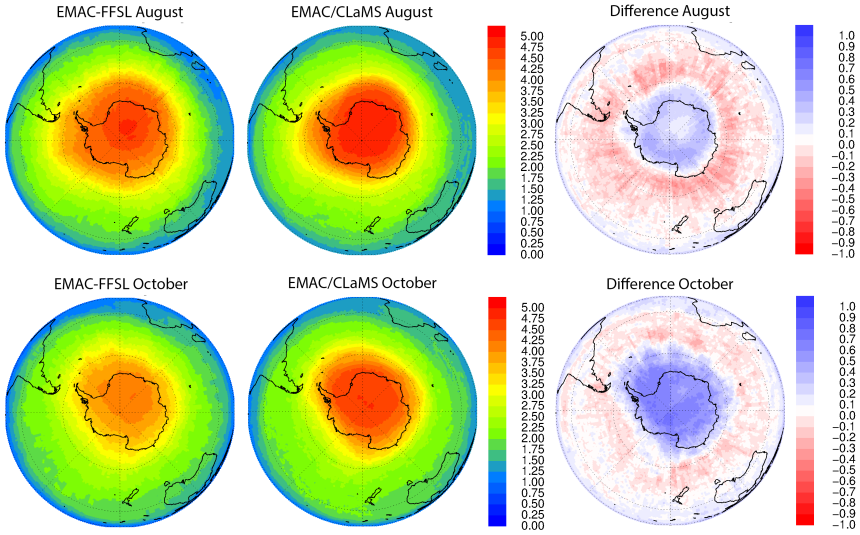

Figure 5.2: Age of air [years] at 450 K for August (top panels) and October (bottom panels) in the Southern hemisphere. Left and middle panels display age of air distributions for EMAC-FFSL and EMAC/CLaMS, respectively. Right panels show the absolute difference in mean age of air [years] (EMAC/CLaMS−EMAC-FFSL). Blue colour denotes older air in EMAC/CLaMS, and red colour denotes older air in EMAC-FFSL.

5.1 Antarctic polar vortex

Figure 5.2 shows horizontal age of air distributions of EMAC/CLaMS and EMAC-FFSL at 450 K for August and October in the Southern hemisphere. In August (top panels), older air masses are found inside the vortex in EMAC/CLaMS compared to EMAC-FFSL. More specifically, the air is up to 0.5 years younger inside the vortex in EMAC-FFSL. On the contrary, EMAC/CLaMS shows younger air outside the vortex. In October (bottom panels), the age of air differences inside the vortex have increased to values of 0.8 years. The differences are larger than in October because the processes that dominate the vortex evolution are different. During August, diabatic downwelling is the most important process in the vortex. It is found that in August the downwelling of the diabatic vertical velocity in EMAC/CLaMS is stronger in the polar vortex region than the downwelling of the kinematic vertical

velocity in EMAC-FFSL (Sect. 3.4). This leads to the small differences in age of air in August that are displayed in the top right panel of Fig. 5.2. However, in October downwelling decreases in strength and becomes less important for the age of air distribution so that the impact of horizontal transport through the vortex edge and mixing increases [*Gerber*, 2012]. During the period when the transport barrier controls horizontal mixing, the differences in age of air are larger than during the earlier period when downwelling is the most important process.

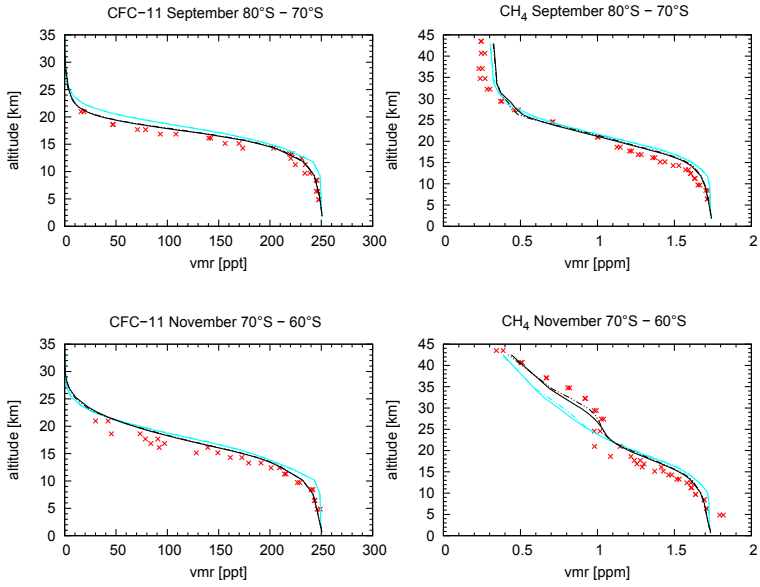

Figure 5.3: Profiles of CFC-11 and CH_4 for different months and latitude bins: ACE-FTS climatology is shown in red, blue profiles display simulation results with EMAC-FFSL transport and black profiles show results with EMAC/CLaMS full Lagrangian transport. Solid lines show mean values over ten years of simulation, whereas dashed-dotted lines indicate results for only the last five years of simulation. The profiles for the simulations have been generated as follows: daily output have been interpolated onto a regular grid, then monthly mean values are calculated. The mean value of all simulated years for the respective latitude bins is shown here. ACE-FTS climatological profiles are shown for 72.5°S and 77.5°S in the top panels, and for 62.5°S and 67.5°S in the bottom panels, respectively.

The simulated pattern of long-lived tracers with a purely stratospheric loss and a purely tropospheric source are dominated by the age of air distribution in the model but allow a comparison against measurements. For the Antarctic polar vortex region, vertical profiles of simulated CFC-11 and CH_4 were compared with profiles from measurement climatologies of the Atmospheric Chemistry Experiment-Fourier Transform Spectrometer (ACE-FTS). The ACE-FTS climatology [*Jones et al.*, 2012] contains monthly zonal mean values for 14 species. It does not include error budget estimates, but comparisons with measurements from other instruments show differences in the order of 10% for CFC-11 and CH_4 [*Jones et al.*, 2012]. The climatology includes ACE-FTS measurements from February 2004 to February 2009.

The top panels in Fig. 5.3 show profiles for September in the 80°S to 70°S latitude bin. At this time, the vortex is still stable and clearly separated from mid-latitude air. The profile of CFC-11 from EMAC/CLaMS is in good agreement with the ACE-FTS climatology, although slightly higher in the 17-19 km altitude range. However, the EMAC-FFSL simulation produces higher CFC-11 mixing ratios for all altitudes. This shows that the transport barrier at the edge of the polar vortex is weaker in the EMAC-FFSL simulation which results in an overestimated mixing across the vortex edge.

The top right panel of Fig. 5.3 displays the respective profiles of CH_4. Here, the same pattern as shown in the CFC-11 profiles is visible. The EMAC-FFSL profiles show higher CH_4 concentrations than the satellite climatology. EMAC/CLaMS also exhibits higher CH_4, but is closer to the ACE-FTS measurements up to 20 km. At altitudes above 30 km both models show higher CH_4 mixing ratios than observed. Overall, EMAC/CLaMS transport leads to an improvement of the CH_4 simulation in the vortex region, although it still results in higher mixing ratios compared to the satellite climatology.

The bottom panels in Fig. 5.3 present similar plots for November between 70°S and 60°S. In this month, the Antarctic vortex begins to break up. This process starts at high altitudes. The weakening of the vortex boundary is clearly visible in the CH_4 profiles in the bottom right panel. The ACE-FTS profile exhibits a pronounced kink at 20 to 25 km altitude. This kink appears in the profile because the vortex air masses above 25 km are mixed with CH_4-rich air from mid-latitudes. The kink is also visible in the EMAC/CLaMS profiles, although it is not as distinct as in the ACE-FTS climatology. The EMAC/CLaMS profiles between 90°S and 70°S latitude also feature this kink, but at these most Southern latitudes there are no ACE-FTS measurements available for comparison. In the EMAC-FFSL profiles, this

kink is not visible. These results indicate that the vortex breakup is much better represented in the CLaMS Lagrangian transport. The kink is not visible in the respective CFC-11 profiles (bottom left panel), because the concentrations are too low to show indications of mixing between polar and mid-latitude air in the altitude range where the beginning of the vortex breakup occurs. The CFC-11 profiles of November are another example for the overall pattern of differences between the two transport schemes: with the CLaMS full-Lagrangian transport, it is possible to produce trace gas distributions that indicate a stronger polar vortex than in EMAC-FFSL, but still weaker than in the satellite climatology, which seems to be linked to the weaker zonal winds in EMAC (see Fig. 5.1).

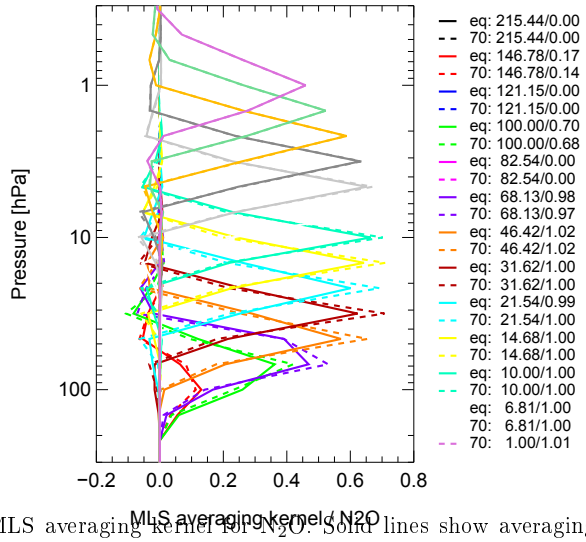

Figure 5.4: MLS averaging kernel for N_2O. Solid lines show averaging kernels for the equator (eq), and dashed lines show averaging kernels for 70° latitude (70). The equatorial averaging kernels are applied to all profiles up to 60° in both hemispheres, and the averaging kernel for 70° is applied from 75° to the pole. Between 60° and 75°, a linear interpolation between the averaging kernel for the equator and the averaging kernel for 70° is used. In the legend, the first number denotes the pressure level [hPa], for which the averaging kernel is valid. The second number is the sum of all weighting factors of the averaging kernel. Courtesy of F. Ploeger.

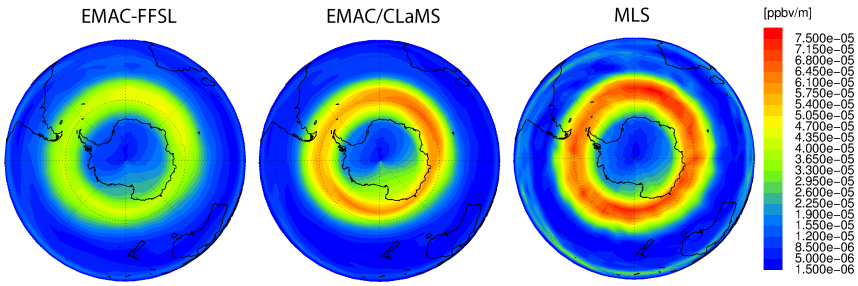

Figure 5.5: Horizontal gradient of N_2O in September on the 450 K isentropic surface.

The polar vortex edge is characterized by strong horizontal gradients of trace gases. For this study, N_2O gradients from the simulation climatologies are compared to gradients in monthly climatologies from MLS measurements (see Sect. 4.1). For the comparison, the simulation results have been vertically smoothed in a way that simulates the smoothing achieved by the MLS averaging kernel. *Ploeger et al.* [2013] show that this procedure is necessary to obtain a meaningful comparison of model results with MLS measurements in the lower stratospheric polar regions. Figure 5.4 presents the MLS averaging kernel for N_2O. The simulation climatologies have been interpolated to the pressure levels that are used for the averaging kernel. Then, the smoothed climatology was calculated by applying the weighting functions that are shown in Fig. 5.4 to the interpolated simulation results. E.g., the value for the pressure level at 68.13 hPa is the sum of the N_2O mixing ratios from the pressure levels from about 105 hPa to 40 hPa, multiplied with the displayed weighting factors. The averaging kernel was applied to the simulation climatologies above 68.13 hPa, where the sum of all weighting factors is close to 1. In lower levels the influence of the a priori values is too large in the MLS averaging kernel and it can not be applied in a post-processing diagnostic.

Figure 5.5 shows the absolute value of the horizontal N_2O gradients on the 450 K isentropic surface for September. The left panel displays the EMAC-FFSL results, the middle panel the gradient in EMAC/CLaMS, and the right panel the MLS climatological values. It is clearly visible that the N_2O gradient is too weak in the EMAC-FFSL transport, with maximum values around $4.5 \cdot 10^{-5}$ ppb/m. The MLS data exhibit maximum values of $7.0 \cdot 10^{-5}$ ppb/m. The EMAC/CLaMS N_2O gradient, calculated with the full Lagrangian transport scheme, shows maximum values of $6.0 \cdot 10^{-5}$ ppb/m. These values are still smaller than those found in the satel-

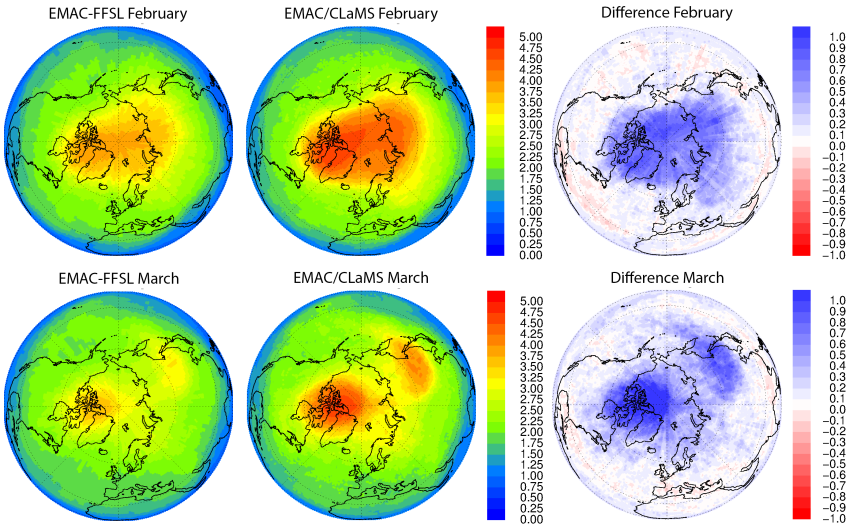

Figure 5.6: Age of air [years] at 450 K for February (top panels) and March (bottom panels) in the Northern hemisphere. Left and middle panels display age of air distributions for EMAC-FFSL and EMAC/CLaMS, respectively. Right panels show the absolute difference in mean age of air [years] (EMAC/CLaMS−EMAC-FFSL). Blue colour denotes older air in EMAC/CLaMS, and red colour denotes older air in EMAC-FFSL.

lite data set, but they show a clear improvement in comparison to the flux-form semi-Lagrangian transport scheme.

5.2 Arctic polar vortex

This section presents age of air distributions in the Arctic polar vortex region at the end of winter. As the Arctic polar vortex shows substantial interannual variability, much more than the Antarctic polar vortex [*Weber et al.*, 2011], the 10-year climatology does not give a clear picture of the Arctic polar vortex. Instead, monthly mean values from the second year of the time-slice simulation are shown as an example in this section.

Figure 5.6 shows age of air distributions in the Northern hemisphere on the 450 K potential temperature surface. In February (top panels), the EMAC/CLaMS simu-

lation results in a stronger polar vortex than the EMAC-FFSL transport. The air inside the vortex is older and the gradient at the vortex edge is stronger when using the full-Lagrangian transport scheme. The absolute differences for age of air in February are displayed in the top right panel. This plot shows that the maximum difference in mean age of air is located inside the vortex and reaches values up to one year.

In March the vortex has split into two parts (see bottom panels in Fig. 5.6). This structure is visible in both transport schemes, but it is more pronounced in EMAC/CLaMS. In the EMAC-FFSL representation, stronger mixing of air masses from inside and outside the vortex has taken place. Again, the differences in age of air are largest (up to one year) in the regions of the polar vortex.

The differences in age of air between EMAC-FFSL and EMAC/CLaMS are larger in the Northern hemispheric vortex than in the Southern hemispheric vortex. This can be explained by the fact that planetary wave activity is stronger in the Arctic than in the Antarctic. Thus, isentropic Rossby waves disturb the zonal symmetry of the Arctic polar vortex much stronger than the symmetry of the almost circumpolar vortex in the Antarctic stratosphere. In such a case, a Lagrangian transport scheme has an advantage over the FFSL approach by minimizing the numerical mixing in the vicinity of a disturbed transport barrier like the vortex edge. The differences between EMAC-FFSL and EMAC/CLaMS due to mixing seem to be larger than the differences due to vertical velocities. This is consistent with the analysis for the Southern hemisphere, where the differences in age of air are most pronounced in October, when the impact of downwelling decreases and the impact of in-mixing into the vortex increases.

Figure 5.7 shows the age of air in the Arctic in February for the following four years in the simulation to illustrate the variability of the Arctic polar vortex. In the third and fifth year, the Arctic polar vortex is more pronounced than in the forth and sixth year of the simulation. In the third year, the vortex is very strong and has a circumpolar structure. In the other years, the shape of the vortex varies and its center is not displaced from the North pole. Figure 5.7 shows clearly that the Arctic polar vortex is always stronger in EMAC/CLaMS than in EMAC-FFSL. Thus, a more pronounced structure in age of air is found in EMAC/CLaMS in cases of stronger as well as weaker vortices.

The differences in the strength of the polar vortex are also visible in trace gas distributions. Figure 5.8 shows the distributions of CFC-11 in EMAC-FFSL and

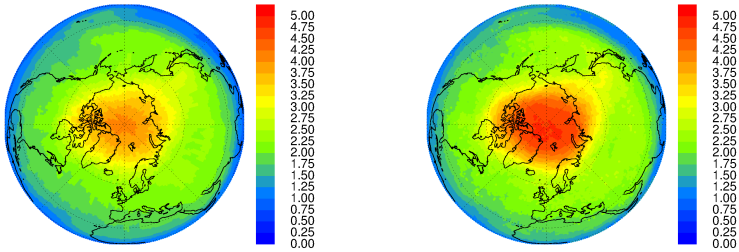

(a) EMAC-FFSL 3rd year (b) EMAC-CLaMS 3rd year

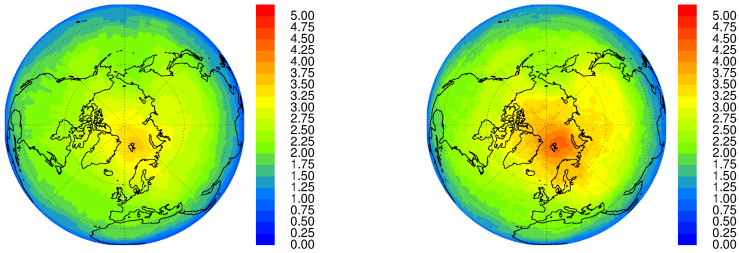

(c) EMAC-FFSL 4th year (d) EMAC-CLaMS 4th year

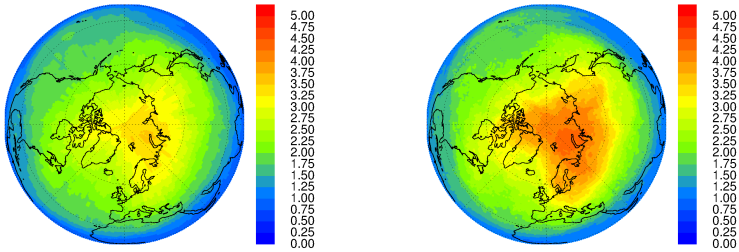

(e) EMAC-FFSL 5th year (f) EMAC-CLaMS 5th year

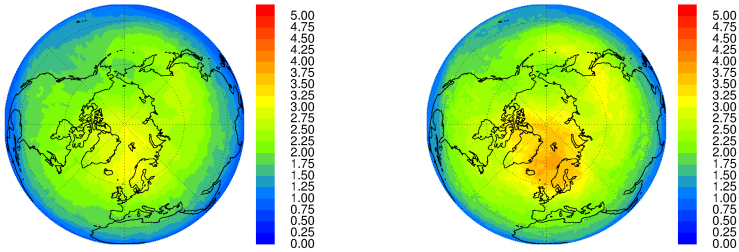

(g) EMAC-FFSL 6th year (h) EMAC-CLaMS 6th year

Figure 5.7: Age of air [years] at 450 K for February in the Northern hemisphere for different years. The left column shows age of air in EMAC-FFSL, and the right column shows age of air in EMAC/CLaMS.

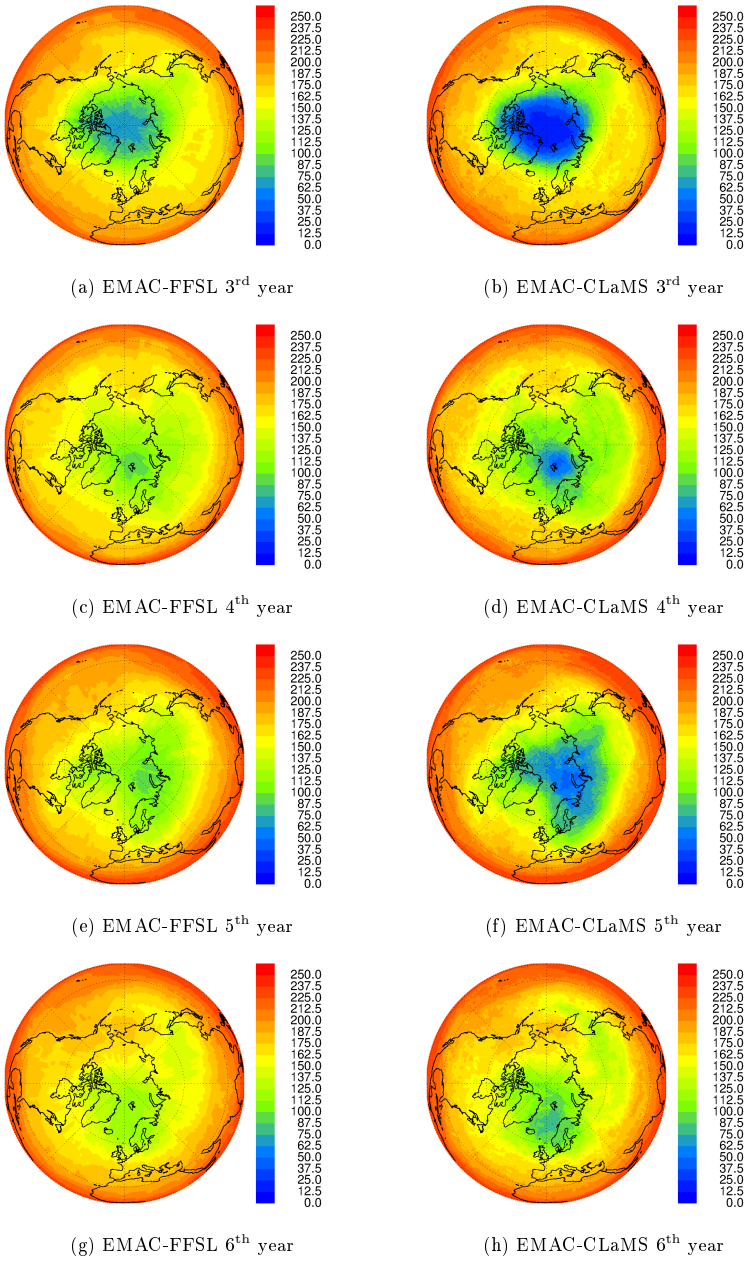

(a) EMAC-FFSL 3rd year

(b) EMAC-CLaMS 3rd year

(c) EMAC-FFSL 4th year

(d) EMAC-CLaMS 4th year

(e) EMAC-FFSL 5th year

(f) EMAC-CLaMS 5th year

(g) EMAC-FFSL 6th year

(h) EMAC-CLaMS 6th year

Figure 5.8: CFC-11 [ppt] at 450 K for February in the Northern hemisphere for different years. The left column shows CFC-11 mixing ratios in EMAC-FFSL, and the right column shows CFC-11 mixing ratios in EMAC/CLaMS.

EMAC/CLaMS in February for the same years as the age of air distributions in Fig. 5.7. The variability of the polar vortex also causes a variation in the CFC-11 distribution in the simulation with very low CFC-11 mixing ratios in the years of a strong, unsplit vortex. Again, there are clear differences visible between the EMAC-FFSL and EMAC/CLaMS simulation results. In EMAC/CLaMS, there are low CFC-11 mixing ratios inside the Arctic polar vortex. In EMAC-FFSL, these low values are not reached. It is expected that lower values of CFC-11 will lead to stronger polar ozone depletion in the model if chemical ozone loss is simulated, which is not done in the present runs using the simplified chemistry scheme. Lower CFC mixing ratios correspond to higher inorganic chlorine reservoir values, which when activated through heterogeneous reactions lead to faster ozone depletion.

CHAPTER 6

Zonal mean climatologies

6.1 Age of air

This section presents zonal mean distributions of age of air which are a very useful result for the verification of the newly coupled model system [*SPARC*, 2013]. The age of air diagnostic is suitable for this purpose since mean age is a passive tracer that directly displays transport characteristics. *Eluszkiewicz et al.* [2000] show that age of air is very sensitive to the choice of the transport scheme. *Mahowald et al.* [2002] investigate the influence of different vertical coordinates on the age of air distributions. They find improved age of air distributions in their simulations when using the hybrid-isentropic vertical coordinate instead of the standard hybrid-pressure vertical coordinate. The advantageous hybrid-isentropic vertical coordinate system was also used for the EMAC/CLaMS simulation. There are different physical mechanisms that impact the distributions of the zonal mean age of air in the model and could lead to discrepancies between different models or observations: The strength of the Brewer-Dobson-Circulation has the largest impact on the magnitude of the mean age, while the quasi-horizontal mixing modulates the width of the tropical upwelling pattern of young air [*Waugh and Hall*, 2002].

Zonal mean age of air at 50 hPa for the EMAC-FFSL and EMAC/CLaMS climatologies is compared to mean age of air derived from measurements in Fig. 6.1. The observed mean age of air values are derived from SF_6 and CO_2 airborne measure-

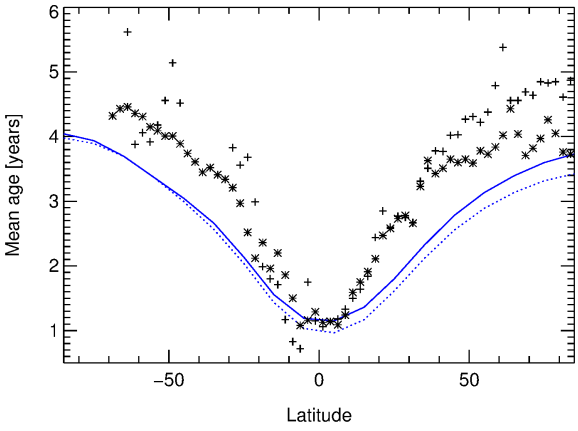

Figure 6.1: Zonal mean age of air at 50 hPa [years]: Simulation results of EMAC/CLaMS are represented by the solid blue line, EMAC-FFSL the dotted blue line, and mean age from airborne measurements by the black crosses (SF_6) and the black asterisks (CO_2). The measurements are taken from different campaigns with the NASA ER-2 aircraft [*Elkins et al.*, 1996; *Boering et al.*, 1996; *Waugh and Hall*, 2002]. The simulated age of air has been reduced by three months to account for the fact that age of air in EMAC-FFSL and EMAC/CLaMS is defined with reference to the surface, while it is defined with reference to the tropopause in the age of air from measurements.

ments from various campaigns with the NASA ER-2 research aircraft [*Elkins et al.*, 1996; *Boering et al.*, 1996; *Waugh and Hall*, 2002]. Figure 6.1 shows that both types of EMAC simulations produce a similar and reasonable age of air distribution. In EMAC-FFSL as well as in EMAC/CLaMS, the age of air pattern is consistent with the general features of the stratospheric circulation. There is upwelling of young air masses in the tropics, and downwelling of old air masses in the polar regions. Both simulations exhibit slightly older air in the Southern hemisphere compared to the Northern hemisphere, consistent with the measurements. Age of air in EMAC-FFSL and EMAC/CLaMS is defined with reference to the surface, while it is defined with reference to the tropopause in the age of air from measurements. Therefore, the simulated age of air in Fig. 6.1 has been reduced by three months to obtain comparable values. The simulated mean age is younger in comparison to observations which is a typical feature seen in climate models that can be much more pronounced than in the example shown here [*Waugh and Hall*, 2002; *SPARC*, 2010]. Age of air

derived from SF_6 at high latitudes is typically high biased because the algorithms do not account for the stratospheric loss of SF_6 [*Waugh and Hall*, 2002]. Overall, both transport representations allow the expected age of air distribution to be reproduced. The largest difference in the simulated age of air is found in Northern hemispheric high latitudes. Here, EMAC/CLaMS shows older air masses than EMAC-FFSL and is thus closer to the observations.

Figure 6.2 shows zonal mean age of air distributions for the altitude range from 350 to 1500 K for EMAC-FFSL and EMAC/CLaMS. As already shown for the 50 hPa level in the last paragraph, the age of air distribution in both EMAC simulations is consistent with the known the stratospheric diabatic circulation (Brewer-Dobson-Circulation) that is discussed in Chapter 3. The tropical upwelling region transporting young air masses from the troposphere upward to the stratosphere is clearly visible. At high latitudes in the stratosphere, the air is older with age of air values of more than 4.75 years in the annual, zonal mean. The highest vertical gradient in age of air is found above the tropopause at around 400 K at high- and mid-latitudes. The zonal mean age of air distributions in Fig. 6.2a and Fig. 6.2b show that both transport schemes, EMAC/CLaMS and EMAC-FFSL, allow a reasonable age of air pattern to be reproduced.

There are however notable differences in age of air of up to 0.5 years between EMAC/CLaMS and EMAC-FFSL (Fig. 6.2c). The annual zonal mean of the age of air differences between the two transport schemes shows younger air in EMAC-FFSL below 500 K. Above 500 K, a clear difference between the Northern and the Southern hemisphere emerges. The usage of EMAC/CLaMS results in younger air in the Southern hemisphere and older air in the Northern hemisphere compared to EMAC-FFSL. This picture of the annual mean differences is a result of various processes that change over the course of a year. Therefore, the age of air differences in all seasons are now analysed separately.

Figure 6.3 shows age of air differences between EMAC-FFSL and EMAC/CLaMS for all seasons. There is a particular pattern which is present throughout the year: In the lowermost stratosphere up to 500 K the age of air is always lower in EMAC-FFSL. One reason for this is the subtropical jet stream that constitutes a transport barrier, which is more pronounced in EMAC/CLaMS than in EMAC-FFSL (see Sect. 4.3). The second reason is a more diffusive tropopause when using the flux-form semi-Lagrangian transport scheme, allowing young, tropospheric air to diffuse upward into the lowermost stratosphere. The full-Lagrangian scheme provides a stronger transport barrier at the tropopause.

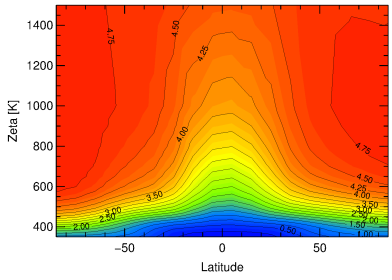

(a) EMAC-FFSL

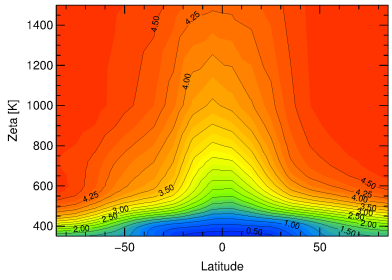

(b) EMAC/CLaMS

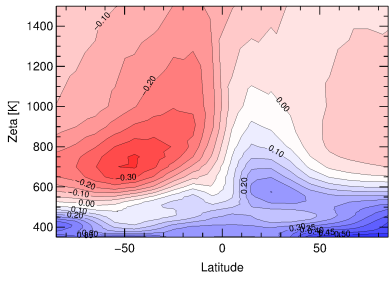

(c) EMAC/CLaMS - EMAC-FFSL

Figure 6.2: Annual, zonal mean age of air from simulation climatologies [years] for EMAC-FFSL and EMAC/CLaMS. The bottom panel displays absolute differences in age of air (EMAC/CLaMS−EMAC-FFSL) [years]. Here, blue colors indicate younger air in EMAC-FFSL, while red colors indicate younger air in EMAC/CLaMS.

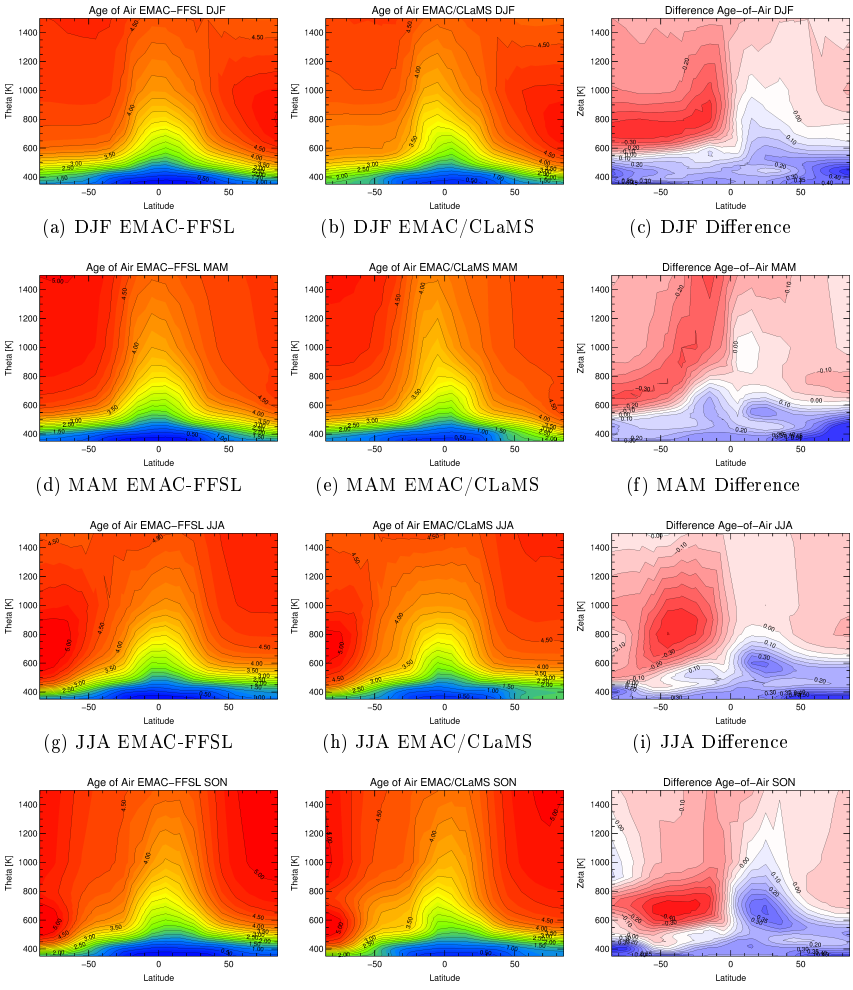

(a) DJF EMAC-FFSL (b) DJF EMAC/CLaMS (c) DJF Difference

(d) MAM EMAC-FFSL (e) MAM EMAC/CLaMS (f) MAM Difference

(g) JJA EMAC-FFSL (h) JJA EMAC/CLaMS (i) JJA Difference

(j) SON EMAC-FFSL (k) SON EMAC/CLaMS (l) SON Difference

Figure 6.3: Zonal mean age of air for different seasons in EMAC-FFSL (left column) and EMAC/CLaMS (middle column) [years] and the absolute differences in age of air (EMAC/CLaMS−EMAC-FFSL, right column) [years].

Between 500 and 600 K around 20° latitude in both hemispheres, there are other regions where EMAC-FFSL shows younger air than EMAC/CLaMS. In contast to the region below 500 K, this feature can be associated with differences in the vertical wind field. As already discussed in Sect. 3.4, the kinematic vertical velocity in EMAC-FFSL exhibits a minimum in upwelling above the equator that is barely present in the diabatic vertical velocity in EMAC/CLaMS. Around this minimum, the vertical velocity is higher in EMAC-FFSL than in EMAC/CLaMS. As a consequence, age of air values are lower in EMAC-FFSL in the regions of stronger upwelling around the equatorial minimum. This effect is clearly visible in boreal spring (MAM, Fig. 6.3f) and summer (JJA, Fig. 6.3i). During boreal autumn, the shift in tropical upwelling that is described below dominates in these regions.

The flux-form semi-Lagrangian transport in EMAC-FFSL results in younger age of air in the polar vortices. This is visible in the polar regions in the respective winter hemisphere with a maximum age of air difference between 400 and 450 K. Here, the difference in age of air is a combined effect of stronger downwelling and a more distinct transport barrier at the vortex edge in EMAC/CLaMS. The representation of the polar vortices in both transport schemes is discussed in detail in Sect. 5.

The most obvious pattern in the age of air differences is the hemispheric age difference at altitudes from 500 to 900 K. This feature dominates the annual mean age difference pattern (Fig. 6.2c) with younger air in EMAC-FFSL in the Northern hemisphere and younger air in EMAC/CLaMS in the Southern hemisphere. Considering all seasonal age of air differences shown in Fig. 6.3, this pattern is not visible equally strongly in all seasons. The hemispheric age of air difference between EMAC-FFSL and EMAC/CLaMS starts to evolve in boreal summer (Fig. 6.3i) and is most pronounced in boreal autumn (Fig. 6.3l). The reason for this difference pattern is the shift of the maximum upwelling in the tropical pipe between EMAC/CLaMS and EMAC-FFSL in boreal summer. During this season, the upwelling in the kinematic vertical velocity field of EMAC-FFSL shifted northwards compared to the diabatic upwelling of EMAC/CLaMS. This is illustrated in Fig. 3.9. *Ploeger et al.* [in preparation] also found that a shift of the tropical pipe leads to hemispheric differences in the age of air pattern.

In boreal autumn (SON, Fig. 6.3l), the hemispheric difference pattern is not symmetric. The pattern of younger age of air in EMAC-FFSL in the Northern hemisphere is less pronounced than the pattern of younger age in EMAC/CLaMS in the Southern hemisphere. The Northern hemispheric difference in age of air is limited to the latitudes from the Equator to 40°N and can be fully explained by the shift of the

maximum upwelling region. On the other hand, in the Southern hemisphere, the younger age of air pattern in EMAC/CLaMS is more pronounced and extends to higher latitudes. This observation can be explained by a combination of two processes: The first reason is, as for EMAC-FFSL in the Northern hemisphere, the shift in tropical upwelling. The second reason is the difference in the transport barriers. In EMAC-FFSL, the polar vortex edge is more diffusive which leads to enhanced in-mixing of old air from the polar vortex into mid-latitude air in the Southern hemisphere in EMAC-FFSL. Additionally, the Southern subtropical barrier in this season is stronger in EMAC-FFSL so that in-mixing of young air from the tropical pipe is reduced in this transport scheme. Thus, the difference in age of air between the two transport schemes is enhanced for the SH mid-latitude region.

During summer in the Southern hemisphere (DJF) the tropical upwelling is stronger in EMAC/CLaMS than in EMAC-FFSL (Fig. 6.3c). This leads to differences in age of air from 600 to 1200 K in the region of the tropical pipe between EMAC-FFSL and EMAC/CLaMS. Figure 3.8 shows that this difference is clearly related to higher vertical velocities in EMAC/CLaMS. In this figure, all isolines show that the upwelling in the diabatic vertical velocity representation in EMAC/CLaMS is stronger than the upwelling in the kinematic vertical velocity representation in EMAC-FFSL. The differences are visible throughout the altitude range from 500 to 1500 K in the SH tropical region from 0°S to 20°S. In the following months (MAM, Fig. 6.3f), as a consequence of the stronger upwelling, the younger age of air pattern in EMAC/CLaMS extends to higher altitudes above 1500 K.

In summary, the discussion above made clear that there are two distinct features of the transport schemes in focus (EMAC-FFSL and EMAC/CLaMS) that are responsible for the different simulations of age of air and trace gases. Firstly, one feature is the use of various vertical velocities due to different vertical coordinates. Secondly, the different transport schemes lead to diverse mixing properties of transport. Only by considering both aspects, all differences between EMAC-FFSL and EMAC/CLaMS can be explained.

6.2 N_2O

As in the case of age of air, the simulated patterns of long-lived tracers with a purely stratospheric loss and a purely tropospheric source reflect the stratospheric circulation. In addition, the analysis of these tracers allows a comparison against

measurements. Therefore, simulated annual zonal mean climatological nitrous oxide (N_2O) distributions are compared to a satellite climatology.

The N_2O simulation results from the EMAC-FFSL and EMAC/CLaMS 10-year climatologies are compared to climatologies from measurements of the Microwave Limb Sounder (MLS) onboard the NASA Aura satellite from the years 2005 to 2012 (see Sect. 4.1). For the comparison, the simulation results have been vertically smoothed in a similar way as the averaging kernel of the MLS retrievals smoothes the atmospheric profiles.

Figure 6.4 shows annual, zonal mean N_2O mixing ratios for EMAC-FFSL with averaging kernel, EMAC/CLaMS with averaging kernel, and MLS from 70 hPa up to 3 hPa. In this altitude range, MLS delivers reliable N_2O measurements [*Livesey et al.*, 2011]. The results of both simulations as well as the MLS climatology show a similar circulation pattern. In all climatologies, N_2O exhibits higher mixing ratios in the upwelling region in the tropics and lower mixing ratios in the descending air at high latitudes. In the tropical region, the highest N_2O mixing ratios are about 300 ppb at 70 hPa and decrease with height. In the downwelling regions at high latitudes, N_2O mixing ratios below 15 ppb are found in the climatologies above altitudes of ~5 hPa. In the tropical regions, the pattern of high N_2O in the tropical pipe is narrower in the MLS data than in both simulations with the different transport representations. The contours of N_2O in Fig. 6.4c are steeper around 20°N and 20°S than in the simulated climatologies. The contours of EMAC/CLaMS are slightly steeper than those in EMAC-FFSL and thus closer to the measurements. The tropical pipe and its seasonal variation is analysed in more detail in Sect. 4.1. Another feature is also improved when using the Lagrangian transport, which is the underestimated N_2O mixing ratio in EMAC-FFSL between 10 and 20 hPa in Southern mid-latitudes.

The relative differences between the measured and simulated N_2O mixing ratios are shown in Fig. 6.5. Overall, the simulation results of EMAC-FFSL and EMAC/CLaMS show higher N_2O mixing ratios at lower altitudes below ~20 hPa and lower mixing ratios above 20 hPa compared to the MLS climatology. The high values of relative differences in the polar downwelling regions above 5 hPa are negligible since the relative differences here become large due to the very low N_2O concentrations. The reason for the too low N_2O mixing ratios in these regions in the simulations is likely due to the upper boundary condition, which is set to 0 ppb for N_2O.

In EMAC-FFSL, the largest difference in N_2O compared to MLS is found in the Southern hemisphere above 20 hPa. In this region, the simulation using the flux-form

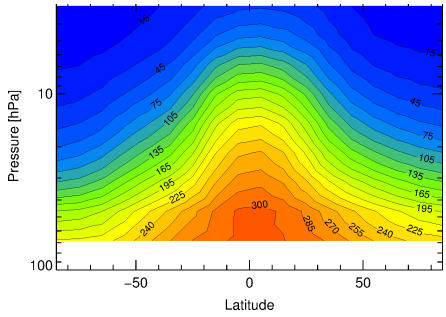

(a) EMAC-FFSL 10-year climatology

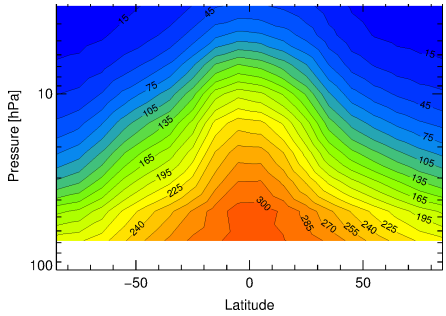

(b) EMAC/CLaMS 10-year climatology

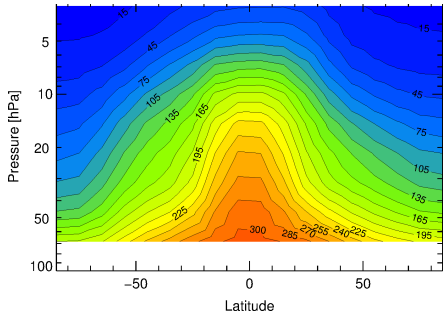

(c) MLS 2005-2012 climatology

Figure 6.4: Zonal mean N_2O mixing ratio [ppb] from modelled and measured climatologies. The simulation results of EMAC/CLaMS and EMAC-FFSL have been vertically smoothed in a similar way as the averaging kernel of the MLS retrievals smoothes the atmospheric profiles.

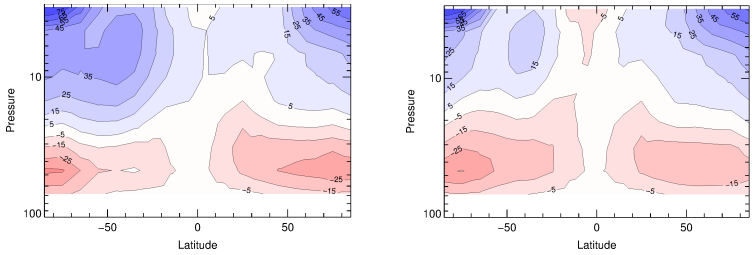

(a) EMAC-FFSL vs. MLS (b) EMAC/CLaMS vs. MLS

Figure 6.5: Zonal mean relative differences of N_2O mixing ratio [ppb] between modelled climatologies and the MLS climatology. Red colour denotes higher N_2O mixing ratios in the simulations, and blue colour denotes a higher N_2O mixing ratio in MLS.

semi-Lagrangian transport scheme shows 35% less N_2O than the MLS climatology. Using the Lagrangian transport scheme, this difference could be significantly reduced. The EMAC/CLaMS climatology only shows a difference of up to 15% compared to the MLS climatology in the Southern hemisphere above 20 hPa.

In the SH tropical region at 10°S, the difference between EMAC/CLaMS and MLS is larger than the difference between EMAC-FFSL and MLS. Here, the vertical wind in EMAC/CLaMS is stronger than the vertical wind in EMAC-FFSL during SH summer (see Sect. 3.4), which leads to enhanced N_2O mixing ratios.

At about 50 hPa in high latitudes in both hemispheres, EMAC-FFSL shows higher N_2O mixing ratios than MLS. The maximum differences are located over the poles. In the Southern hemispheric polar vortex region the annual mean of simulated N_2O mixing ratio of EMAC-FFSL is more than 35% higher than in the MLS climatology. In the Northern hemispheric polar region the difference between EMAC-FFSL and MLS amounts to 25%. In the Southern hemisphere polar region, EMAC/CLaMS is slightly closer to the measured climatology than EMAC-FFSL. In the Northern hemisphere, there is a significant improvement in the EMAC/CLaMS transport. The relative difference between EMAC/CLaMS and MLS N_2O is 15% in the Arctic, while it is 25% between EMAC-FFSL and MLS. The representations of the polar vortex regions in the model simulations are investigated in detail in Chapter 5.

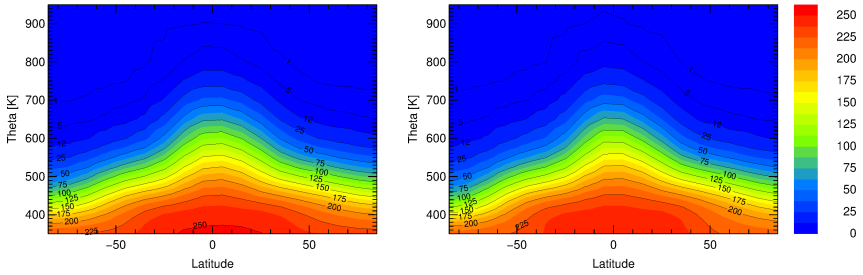

(a) EMAC-FFSL CFC-11 [ppt] (b) EMAC/CLaMS CFC-11 [ppt]

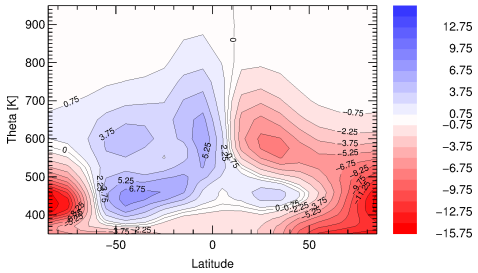

(c) EMAC/CLaMS − EMAC-FFSL ΔCFC-11 [ppt]

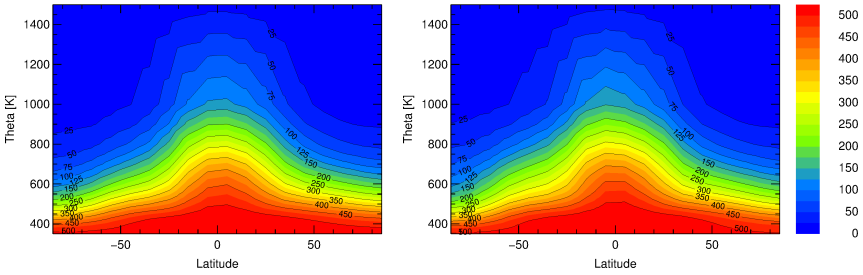

(d) EMAC-FFSL CFC-12 [ppt] (e) EMAC/CLaMS CFC-12 [ppt]

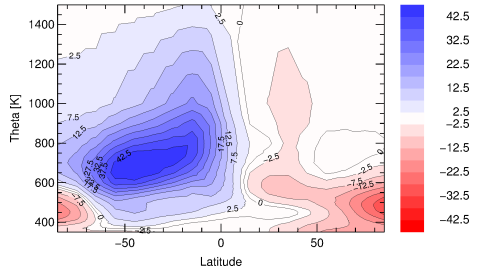

(f) EMAC/CLaMS − EMAC-FFSL ΔCFC-12 [ppt]

Figure 6.6: Zonal mean mixing ratios of different trace gases in EMAC-FFSL and EMAC/CLaMS, as well as the absolute differences. Note that the vertical axis is different for CFC-11 (Fig. 6.6a-6.6c) due to the low mixing ratios of CFC-11 at high altitudes.

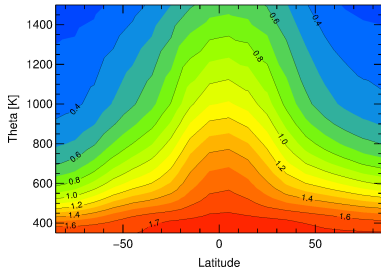

(g) FFSL CH_4 [ppm]

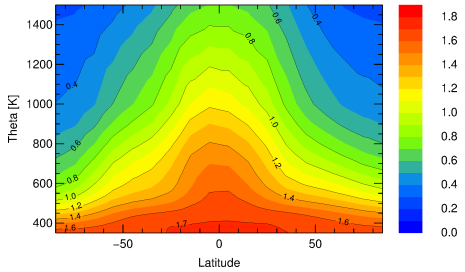

(h) CLaMS CH_4 [ppm]

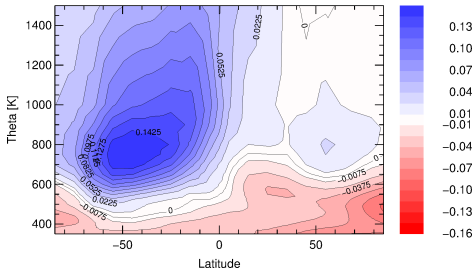

(i) EMAC/CLaMS − EMAC-FFSL ΔCH_4 [ppm]

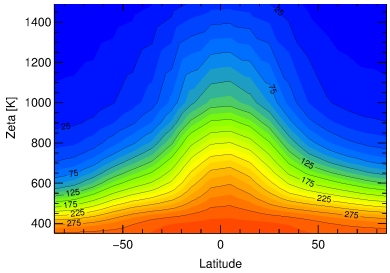

(j) FFSL N_2O [ppb]

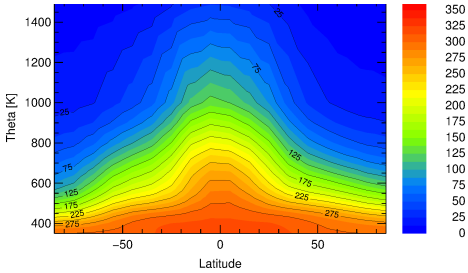

(k) CLaMS N_2O [ppb]

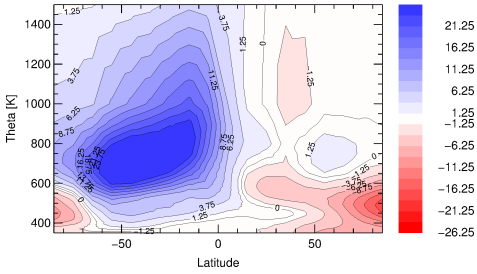

(l) EMAC/CLaMS − EMAC-FFSL ΔN_2O [ppb]

Figure 6.6: (Continued)

Table 6.1: Recommended atmospheric lifetimes [years] and the most likely range for the lifetime of the trace species in the simulation adapted from Table 6.1 and 6.2. in *SPARC* [2013].
* CH_4 is the only shown species with a mainly tropospheric loss. Thus, the atmospheric lifetime of CH_4 is lower than its stratospheric lifetime of ~160 years.

Species	Lifetime	most likely range	
CFC-11	52	43	67
CFC-12	102	88	122
CH_4 *	9.8	7.6	14
N_2O	123	104	152

6.3 Zonal mean trace gas climatologies

In this chapter, zonal mean climatologies for several long-lived trace gases in the simulation with both transport schemes EMAC-FFSL and EMAC/CLaMS are presented. The trace gases are CCl_3F (CFC-11), CCl_2F_2 (CFC-12), CH_4 (methane), and N_2O (nitrous oxide). These trace species all have tropospheric sources, but they have different atmospheric lifetimes and are depleted in different regions in the atmosphere. The atmospheric lifetime τ of a chemical tracer is defined by

$$\tau = \frac{B}{S}, \tag{6.1}$$

where B and S denote the atmospheric burden and sink, respectively. The lifetimes of ozone-depleting substances have recently been re-evaluated in *SPARC* [2013]. The recommended lifetimes of the species included in the simulation are shown in Table 6.1.

Figure 6.6 presents the zonal mean climatologies for various trace gases from EMAC-FFSL and EMAC/CLaMS, as well as the absolute differences between the two simulation climatologies. The overall patterns of the shown trace species look similar, with high mixing ratios in the troposphere, a visible upwelling branch of air with higher trace gas concentrations in the tropical pipe, and low mixing ratios in the downwelling regions of the stratosphere. The differences in the shape of the upwelling branch are due to the different lifetimes of the species and the difference in their height of maximum loss in the stratosphere. The differences between EMAC-FFSL and EMAC/CLaMS are consistent with the difference pattern of age of air (Fig. 6.2c). E.g. in regions where EMAC/CLaMS exhibits lower age of air, the Lagrangian transport scheme shows higher mixing ratios of trace gases of tropospheric

origin.

Because CFC-11 has the strongest loss rate in the stratosphere [*Minschwaner et al.*, 2013; *SPARC*, 2013], the distribution of CFC-11 has a strong vertical gradient and thus very low mixing ratios are present at altitudes above 700 K (Figs. 6.6a, 6.6b). The differences in CFC-11 between EMAC/CLaMS and EMAC-FFSL in Fig. 6.6c show the expected pattern: CFC-11 mixing ratios are lower in EMAC/CLaMS in the polar vortex regions with a maximum difference at the altitude of 450 K. Above 500 K, the hemispheric difference due to the shift in tropical upwelling is visible: Compared to EMAC-FFSL, the trace gas mixing ratios in EMAC/CLaMS are lower in the Northern hemisphere and higher in the Southern hemisphere.

CFC-12 has a longer lifetime than CFC-11, and the region with maximum depletion is located at higher altitudes [e.g., *Minschwaner et al.*, 2013]. Therefore, CFC-12-rich air can propagate to higher altitudes in tropical upwelling region (Figs. 6.6d, 6.6e). The lifetime of N_2O is comparable to the lifetime of CFC-12 and the zonal mean distributions have a similar shape (Figs. 6.6j, 6.6k). The absolute differences in the zonal mean of CFC-12 and N_2O also share characteristics (Figs. 6.6f, 6.6l): One example is the pattern of air masses containing more CFC-12 and N_2O in EMAC-FFSL than in EMAC/CLaMS which is located at 30°N between 800 and 1200 K. For the long-lived trace species CFC-12 and N_2O, this pattern is expanded to higher altitudes than in the zonal mean of CFC-11, which has a shorter lifetime.

Table 6.1 presents total atmospheric lifetimes which approximate the stratospheric lifetimes for CFC-11, CFC-12, and N_2O. In contrast to the other trace gases shown in Fig. 6.6, CH_4 also has tropospheric sinks and is largely removed before entering the stratosphere. Thus, the stratospheric lifetime of CH_4 is much higher than its total atmospheric lifetime. The stratospheric lifetime of CH_4 is approximately 160 years [*SPARC*, 2013], so that the stratospheric vertical gradient of CH_4 is lower than the vertical gradients of the other trace gases.

6.4 Lifetime estimates for CFC-12

Good estimates of the lifetimes of CFCs are important to determine their ozone-depleting potentials and their global warming potentials [*WMO*, 2011; *SPARC*, 2013; *IPCC*, 2013]. Following the theory of *Plumb and Ko* [1992], the ratio of the atmospheric lifetimes of two long-lived species can be derived from the slope of their correlation function in the lower stratosphere at mid-latitudes. This method is only

Table 6.2: Ratio of lifetimes τ(CFC-11) / τ(CFC-12).

Year	EMAC-FFSL	EMAC/CLaMS
1	0.483± 0.080	0.483± 0.080
2	0.486± 0.080	0.491± 0.081
3	0.495± 0.081	0.486± 0.080
4	0.497± 0.082	0.495± 0.081
5	0.485± 0.080	0.484± 0.079
6	0.493± 0.081	0.489± 0.081
7	0.497± 0.082	0.498± 0.082
8	0.485± 0.080	0.476± 0.078
9	0.482± 0.079	0.466± 0.077
10	0.502± 0.083	0.492± 0.081
6-10	0.492± 0.081	0.484± 0.080

applicable if the species are sufficiently long-lived. If the local lifetime is longer than the time scale for horizontal mixing, a compact correlation evolves and the slope of the correlation function can be determined. More precisely, suitable regions for the diagnostic using tracer-tracer correlations show the following characteristics: the chemical sources and sinks of the tracers are weak and isentropic stirring is much faster than the diabatic vertical velocity [*Plumb*, 2007]. Therefore, when applied to atmospheric measurements, the slopes of the tracer-tracer correlation functions have to be determined at the mid-latitude tropopause region [*Plumb*, 1996; *Volk et al.*, 1997].

This slope is related to the ratio of the tracer lifetimes by

$$\frac{\tau_1}{\tau_2} = \frac{B_1}{B_2}\frac{d\sigma_2}{d\sigma_1}. \tag{6.2}$$

Here, τ_1 and τ_2 are the respective lifetimes of the two species. B_1 and B_2 denote their global burdens, and $d\sigma_2/d\sigma_1$ denotes the correlation slope at steady-state conditions.

Volk et al. [1997] used this method to derive atmospheric lifetimes relative to CFC-11 for various species (e.g. CFC-12, N_2O, CH_4, CFC-113) from in-situ aircraft measurements. *Brown et al.* [2013] calculated lifetimes based on ACE-FTS data, in the same way.

Hoffmann et al. [2014] use different zonal mean climatologies from satellite measurements to derive relative lifetimes of CFC-12 in relation to CFC-11. The method delivers consistent CFC-12 lifetimes for different satellite climatologies. The same

Table 6.3: Relative lifetimes of CFC-12 based on a lifetime of 52 years of CFC-11 in EMAC-FFSL.

Year	EMAC-FFSL global	EMAC-FFSL NH	EMAC-FFSL SH
1	107.7 (92.4 - 129.0)	118.7 (102.0 - 142.1)	96.3 (82.7 - 115.3)
2	107.0 (91.9 - 128.1)	113.8 (97.7 - 136.1)	100.6 (86.4 - 120.4)
3	105.1 (90.3 - 125.6)	107.4 (92.2 - 128.7)	102.6 (88.1 - 122.6)
4	104.6 (89.8 - 125.3)	108.1 (92.9 - 129.4)	101.2 (87.0 - 120.9)
5	107.2 (92.0 - 128.4)	111.6 (95.8 - 133.7)	103.2 (88.6 - 123.5)
6	105.5 (90.6 - 126.2)	105.7 (90.8 - 126.5)	105.1 (90.3 - 125.6)
7	104.6 (89.8 - 125.3)	105.1 (90.3 - 125.6)	104.4 (89.7 - 125.0)
8	107.2 (92.0 - 128.4)	109.9 (94.4 - 131.6)	104.4 (89.7 - 125.0)
9	107.9 (92.7 - 129.0)	110.9 (95.2 - 132.7)	104.8 (90.0 - 125.6)
10	103.6 (88.9 - 124.1)	105.7 (90.8 - 126.5)	101.6 (87.2 - 121.5)
6-10	105.7 (90.8 - 126.5)	107.4 (92.2 - 128.7)	104.0 (89.3 - 124.4)

method was also applied to the EMAC/CLaMS results. In the present work, a comparison of the lifetime estimates from EMAC-FFSL and EMAC/CLaMS is presented. The method that is used here to derive the relative atmospheric lifetimes from the climatologies is discussed in detail by *Hoffmann et al.* [2014].

Tables 6.3 and 6.4 list the lifetime estimates for CFC-12 based on a reference lifetime of CFC-11 of 52 years, as recommended by *SPARC* [2013]. As CFC-12 was not initialized from the climatological CLaMS simulation as the other trace species (Sect. 2.4, Appendix C), a spin-up phase is required for CFC-12. Thus, the relative lifetime of CFC-12 in EMAC-FFSL and EMAC/CLaMS was calculated only from the zonal mean climatologies of CFC-11 and CFC-12 for the last five years of the 10-year perpetuum run.

The analysis shows global lifetime estimates that are similar for both transport schemes. The mean global lifetime of CFC-12 in the 5-year mean is 106 years for EMAC-FFSL and 107 years for EMAC/CLaMS. This indicates that both transport schemes provide a reasonable simulation of stratospheric transport. The ratio τ(CFC-11) / τ(CFC-12) is 0.492 for EMAC-FFSL and 0.484 for EMAC/CLaMS. These results are in very good agreement with the recent lifetime estimates from satellite climatologies by *Hoffmann et al.* [2014]. In that study, the the CFC-11/CFC-12 lifetime ratios range from 0.49 to 0.50 for different satellite instruments. The CFC-12 lifetimes from the simulations are in very good agreement with the lifetimes derived by *Minschwaner et al.* [2013] and slightly higher than the current recommendation

Table 6.4: Relative lifetimes of CFC-12 based on a lifetime of 52 years of CFC-11 in EMAC/CLaMS.

Year	EMAC/CLaMS global	EMAC/CLaMS NH	EMAC/CLaMS SH
1	107.7 (92.4 - 129.0)	118.5 (101.8-141.7)	98.9 (85.0 -118.2)
2	105.9 (90.9 - 126.8)	108.6 (93.2 -130.0)	103.6 (88.9 -124.1)
3	107.0 (91.9 - 128.1)	104.0 (89.3 -124.4)	110.2 (94.5 -132.0)
4	105.1 (90.3 - 125.6)	103.2 (88.6 -123.5)	107.0 (91.9 -128.1)
5	107.4 (92.4 - 128.4)	106.3 (91.4 -127.1)	108.8 (93.4 -130.3)
6	106.3 (91.2 - 127.5)	102.6 (88.1 -122.6)	110.4 (94.7 -132.3)
7	104.4 (89.7 - 125.0)	101.2 (86.8 -121.2)	108.1 (92.9 -129.4)
8	109.2 (93.9 - 130.7)	109.2 (93.9 -130.7)	109.2 (93.9 -130.7)
9	111.6 (95.8 - 133.7)	112.3 (96.5 -134.4)	111.1 (95.4 -133.0)
10	105.7 (90.8 - 126.5)	103.0 (88.4 -123.2)	108.8 (93.4 -130.3)
6-10	107.4 (92.2 - 128.7)	105.3 (90.4 -125.9)	109.5 (94.0 -131.0)

by *SPARC* [2013] of 102 years.

The lifetimes were also estimated separately for the Northern and the Southern hemisphere. The results for each hemisphere are also shown in the Tables 6.3 and 6.4. In EMAC-FFSL, the lifetime of CFC-12 in the 5-year mean is higher in the Northern hemisphere (107 years) than in the Southern hemisphere (104 years). Considering all single years of the EMAC-FFSL simulation in Table 6.3, the lifetime of CFC-12 is always higher in the Northern hemisphere. However, in the EMAC/CLaMS 5-year mean, the lifetime is higher in the Southern hemisphere (110 years) than in the Northern hemisphere (105 years). However, these differences are likely not significant considering the large error estimates. In the first year of the simulation, both transport schemes show a higher lifetime in the Northern hemisphere, which is likely due to the different initialization methods of CFC-11 and CFC-12. With the CLaMS Lagrangian transport scheme, this relation changes after two years: From the third year (with one exception in the ninth year), the Northern hemispheric lifetime of CFC-12 in EMAC/CLAMS is lower than the Southern hemispheric lifetime. Thus, the hemispheric lifetimes of CFC-12 in EMAC/CLaMS are in better agreement with measurement climatologies than the respective lifetimes in EMAC-FFSL. All climatologies derived from measurements that were analysed by *Hoffmann et al.* [2014] show a higher lifetime in the Southern hemisphere, like EMAC/CLaMS.

Thus, the results for global and hemispheric relative lifetimes of CFC-12 in EMAC/CLAMS compare very well with lifetimes derived independently from vari-

ous satellite climatologies by *Hoffmann et al.* [2014]. The good agreement between the model deduced and observationally deduced lifetimes provides further confidence in the representation of transport and chemistry of long-lived tracers in the EMAC/CLaMS model system.

CHAPTER 7

Conclusions

The full-Lagrangian CTM CLaMS was successfully coupled with the climate model EMAC. The interface structure MESSy was used for coupling the two models. In this thesis, a ten-year time-slice simulation was performed with the newly coupled model system EMAC/CLAMS. Climatologies for age of air and the long-lived trace species CFC-11, CFC-12, CH_4, and N_2O have been created from the simulation results. The EMAC/CLAMS climatologies have been compared to climatologies derived with the standard flux-form semi-Lagrangian transport scheme in EMAC and validated by comparison to satellite data.

The motivation for implementing the Lagrangian transport scheme of CLaMS in a climate model was to obtain more accurate simulations of trace gas distributions in the stratosphere and in the UTLS region. When using the original FFSL transport scheme in the EMAC model, the isolation of the polar vortex is too weak and there is a too much mixing of tropical and mid-latitude air, especially in the Northern hemisphere [*SPARC*, 2010]. Improvements in these regions could be achieved, as shown in this study. In most parts of the stratosphere trace gas distributions derived with EMAC/CLaMS show better results compared to trace gas climatologies derived with the FFSL transport scheme. The reason for the changes in simulated trace gas distributions can be attributed to two differences in the CLaMS transport scheme compared to the FFSL transport scheme:

Vertical velocity The vertical velocity based on diabatic heating in EMAC/CLaMS leads to a more uniform pattern of the Brewer-Dobson-Circulation compared to the kinematic vertical velocity in EMAC-FFSL, which is more noisy. There are no measurements of stratospheric vertical velocities that allow for direct validation of the simulated values, but it is possible to compare modelled trace gas distributions with measurements. Long-lived trace gases show an accumulated effect of the differences in vertical velocity. The comparison of simulated trace gas distributions reveals that in most regions of the stratosphere the diabatic velocity results in more realistic trace gas distributions, e.g. by providing stronger downwelling in the polar vortices. One exception is unrealistically large updraft during the Southern hemisphere summer at 10°S in the diabatic vertical velocity. Using the diabatic vertical velocity further improves the location of the maximum upwelling region in the tropics, which leads to remarkable differences in trace gas and age of air distributions between EMAC-FFSL and EMAC/CLaMS.

Representation of advection and mixing The main difference between EMAC-FFSL and EMAC/CLaMS is the numerical scheme for the calculation of tracer transport. The CLaMS transport scheme shows clear improvements in cases of strong transport barriers due to the less diffusive nature of the Lagrangian transport representation. Strong, improved gradients are present in the EMAC/CLaMS climatology at the polar vortex edge, at the winter subtropical jet, and around the tropopause. Moreover, the Lagrangian transport scheme also shows better performance in cases of weakening transport barriers, such as during the polar vortex breakup at high altitudes or at the edge of the tropical pipe in the summer hemisphere. Here, the FFSL transport scheme leads to overestimated tracer gradients while the representation in the Lagrangian transport scheme is more realistic.

The main differences between the simulated trace gas distributions of EMAC-FFSL and EMAC/CLaMS are found in the following regions:

Extratropical lowermost stratosphere Due to two transport barriers at the extratropical tropopause and at the subtropical jet in the winter hemisphere, which are more pronounced in the Lagrangian transport scheme, large differences in the age of air and trace gas distributions are found in the extratropical lowermost stratosphere region. Gradients in trace gas climatologies in the

vicinity of strong transport barriers are larger using the Lagrangian transport scheme than using the FFSL transport scheme. Thus, in the extratropical lower stratosphere, EMAC/CLaMS shows higher age of air and lower mixing ratios of tropospheric tracers than EMAC-FFSL. This effect is more pronounced in the Northern hemisphere with differences of up to 0.5 years in the zonal mean age of air.

SH middle stratosphere Lower age of air is found around 700 K in the Southern hemisphere mid-latitudes in EMAC/CLaMS due to a combined effect of the northward shift of the tropical pipe in EMAC-FFSL, as well as a stronger transport barrier at the subtropical jet during the summer, and a weaker transport barrier at the polar vortex in the FFSL transport scheme. The lower N_2O mixing ratios in EMAC/CLaMS in this region fit better to the satellite climatological N_2O than the higher N_2O mixing ratios derived with EMAC-FFSL.

Polar vortex The polar vortex regions also exhibit large differences in trace gas and age of air distributions between EMAC-FFSL and EMAC/CLaMS. It was found that the age differences are most pronounced at the Arctic polar vortex and reach values of up to one year, where minimising the numerical mixing in the vicinity the vortex edge is crucial for obtaining a sufficiently isolated vortex. Nevertheless, the representation of trace gases in the Antarctic polar vortex could be improved as well with the Lagrangian transport scheme. Comparisons to observations show that the horizontal gradient in N_2O at the Antarctic polar vortex edge could be considerably improved using the CLaMS transport scheme.

The newly developed model system EMAC/CLaMS provides various possibilities for future model studies that were not feasible with the original offline version of CLaMS. The MESSy interface allows for an easy comparison between different process parametrisations, similar as done for transport schemes in the present study. As the ATTILA transport scheme is already implemented into MESSy, the model system presented here will provide the structure for direct comparisons between ATTILA and CLaMS Lagrangian transport in the future.

The promising potential of the newly coupled model is the possibility for two-way coupling between CLaMS and EMAC. That is, trace gas distributions derived by CLaMS can serve as input for the EMAC radiation module. A good representation of the polar vortex is a prerequisite for accurately simulating polar ozone depletion

which is still a difficult task for current CCMs. With the work achieved so far, the extension to the detailed CLaMS chemistry scheme including full ozone chemistry is straightforward to implement.

The newly developed coupled model system EMAC/CLaMS constitutes a suitable tool for future climate simulations which require an accurate representation of stratospheric trace gases. The strength of the full-Lagrangian transport scheme is the simulation of trace gas distributions in regions in the upper troposphere and lower stratosphere, where transport barriers are of crucial importance.

APPENDIX A

MESSy submodels used in the simulation

The present study uses the following MESSy submodels. All submodels whose names begin with 'CLAMS' are new developments for this study and originate from CLaMS modules [*Hoppe et al.*, 2014].

CLAMS This submodel is used to set up the environment for CLaMS Lagrangian air parcels.

CLAMSTRAJ This submodel drives the Lagrangian transport of CLaMS air parcels (see Sect. 2.1.1).

CLAMSCHEM The submodel CLAMSCHEM is used for the application of the CLaMS simplified chemistry scheme on CLaMS Lagrangian air parcels (see Sect. 2.1.3).

CLAMSCHEME5 The submodel CLAMSCHEME5 is used for the application of the CLaMS simplified chemistry scheme on tracers in the ECHAM5 gridpoint representation.

CLAMSCIRRUS This submodel contains a simple freeze-drying scheme from CLaMS.

CLAMSMIX This submodel contains the mixing module for CLaMS Lagrangian air parcels (see Sect. 2.1.2).

CLAMSBMIX The boundary conditions for chemical tracers in the CLaMS chemistry scheme in the Lagrangian as well as in the gridpoint representation are updated using this submodel (see Appendix B).

CLOUD The submodel CLOUD contains the cloud processes from ECHAM5 in a seperated submodel.

CONVECT For the convection scheme, the standard setting was used in this study [Tiedke convection with Nordeng closure, *Tiedtke*, 1989; *Nordeng*, 1994].

GWAVE The Hines scheme was used to parametrise gravity waves in EMAC [*Hines*, 1997].

RAD4ALL RAD4ALL contains the ECHAM5 radiation scheme in a separate submodel for EMAC. It is run every third time step, and EMAC prognostic water vapour and cloud forcing is used. The other radiative forcing is not prognostic. O_3 is taken from the climatology of *Paul et al.* [1998]. The following trace gases are set to a constant value for the year 2000 in the troposphere with a linear decay in the stratosphere: CO_2, CH_4, N_2O, CFC-11, CFC-12.

TRACER Submodel containing data structures and meta data for chemical tracers that are transported using the FFSL transport scheme [*Jöckel et al.*, 2008].

APPENDIX B

Boundary conditions for chemical tracers

The boundaries of the chemical tracers and age of air are updated using results from the climatological CLaMS run [*Pommrich et al.*, 2014]. Tables B.1 and B.2 list the boundaries, up to which the EMAC data are overwritten with the climatological CLaMS data. This table also shows the sources for the CLaMS boundaries.

Water vapour at the lower boundary is not updated by the CLaMS data, but by using the prognostic specific humidity from EMAC. *Pommrich et al.* [2014] provide a detailed description of the boundary conditions in the climatological CLaMS simulation.

[1] http://www.esrl.noaa.gov/gmd/hats/insitu/cats/
[2] www.esrl.noaa.gov/gmd/ccgg/globalview/co/co_intro.html

Table B.1: Lower boundary conditions for chemical tracers and age of air in the EMAC/CLaMS simulation. 0 means that the boundaries are set to Zero. The height denotes the vertical level up to which the data is replaced.

Species	Source	Height
N_2O	CMDL (CATS)[1] [*Rigby et al.*, 2013]	100 K
CH_4	CMDL[2] [*Masarie and Tans*, 1995; *Novelli et al.*, 2003]	100 K
CO_2	CMDL [*Masarie and Tans*, 1995; *Novelli et al.*, 2003]	100 K
CO	MOPITT [*Deeter et al.*, 2011]	500 hPa
O_3	0	100 K
H_2O	EMAC	100 K
CFC-11	CMDL (CATS) [*Rigby et al.*, 2013]	100 K
CFC-12	CMDL (CATS) [*Rigby et al.*, 2013]	100 K
HCl	0	100 K
Mean age	linear increasing [*Waugh and Hall*, 2002]	100 K

Table B.2: Upper boundary conditions for chemical tracers and age of air in the EMAC/CLaMS simulation. 0 means that the boundaries are set to Zero. The data is replaced from the height given in the last column up to the top of the model domain.

Species	Source	Height
N_2O	HALOE [*Grooß and Russell*, 2005]	2000 K
CH_4	HALOE [*Grooß and Russell*, 2005]	2000 K
CO_2	Mean age	2000 K
CO	Mainz-2D model [*Grooß*, 1996]	2000 K
O_3	HALOE [*Grooß and Russell*, 2005]	500 K
H_2O	HALOE [*Grooß and Russell*, 2005]	2000 K
CFC-11	0	2000 K
CFC-12	0	2000 K
HCl	0	500 K
Mean age	MIPAS (SF_6) [*Stiller et al.*, 2008]	2000 K

APPENDIX C

Correlation functions for the initialisation of CFC-12

As CFC-12 was not included in the climatological CLaMS run, which was used for the other trace species for initialization, correlation functions with N_2O were used to initialize CFC-12. N_2O and CFC-12 measurements from the ACE-FTS instrument (see Sect. 5.1) were used for this purpose. ACE-FTS V3.0 data from 01.10.04 to 01.03.05 was used. Data that lie outside the 2σ-range are sorted out by a filter procedure. In the polar regions, additional data that looks reasonable but has a larger uncertainty than allowed for the quality criteria of ACE-FTS was included to obtain a global coverage.

Three correlation functions between N_2O and CFC-12 have been defined for the tropics between 15°N and 15°S in equivalent latitude and the extratropics (polewards from 30° eqivalent latitude) in the Northern and Southern hemisphere. A linear interpolation between the tropical and the respective extratropical correlation function was used in the 15° to 30° latitude range.

A polynomial fit of degree three is used for the correlation between N_2O and CFC-12. Table C.1 shows the coefficients a_i for the polynomial fits $P = \sum_{i=0}^{n} a_i \, x^i$ for the tropics and the extratropics in both hemispheres. In the tropics, two different polynomial fits were used for lower and higher trace gas concentrations.

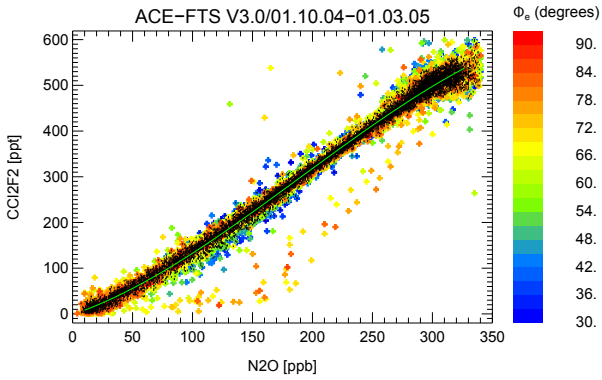

(a) NH extratropics ($\Phi_e = 30°$ to $90°$)

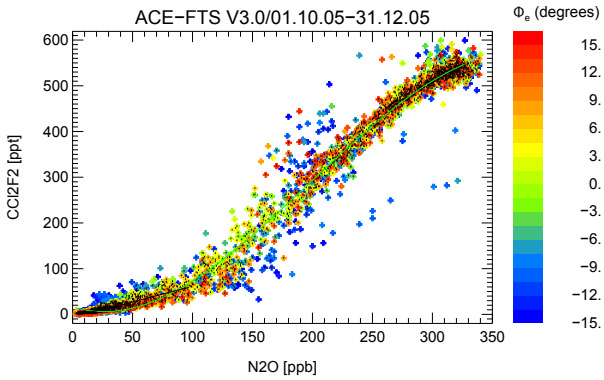

(b) Tropics ($\Phi_e = -15°$ to $15°$)

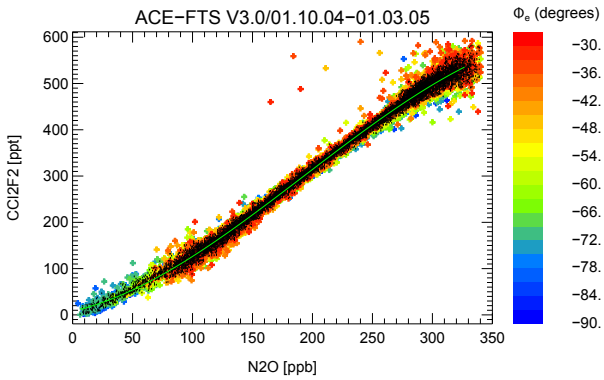

(c) SH extratropics ($\Phi_e = -90°$ to $-30°$)

Figure C.1: Correlation functions for CFC-12 vs. N_2O for different regions (defined by equivalent latitude Φ_e). Courtesy by J.-U. Groß.

Table C.1: Coefficients for the polynomial fit of the correlation between N_2O and CFC-12 in ACE-FTS.

	tropics N_2O:85-330 ppb	tropics N_2O:0-85ppb	NH extr.	SH extr.
a_0	1.7518265	21.725639	-1.3335038	8.0804757
a_1	0.50402438	-1.2563060	0.89538267	0.58536520
a_2	-0.0060683976	0.019773833	0.0054034468	0.0072194461
a_3	5.8999956e-05	-3.3838940e-05	-9.4755294e-06	-1.2460564e-05

Bibliography

Andrews, D. G., J. R. Holton, and C. B. Leovy, *Middle Atmosphere Dynamics*, Academic Press, 1987.

Baldwin, M. P., et al., The quasi-biennial oscillation, *Rev. Geophys.*, *39*, 179–229, 2001.

Bechtold, P., J. Chaboureau, A. Beljaars, A. Betts, M. Kohler, M. Miller, and J. Redelsperger, The simulation of the diurnal cycle of convective precipitation over land in a global model, *Q. J. R. Meteorol. Soc.*, *130*, 3119–3137, 2004.

Boering, K., S. Wofsy, B. Daube, H. Schneider, M. Loewenstein, and J. Podolske, Stratospheric mean ages and transport rates from observations of carbon dioxide and nitrous oxide, *Science*, *274*, 1340–1343, 1996.

Bönisch, H., A. Engel, T. Birner, P. Hoor, D. W. Tarasick, and E. A. Ray, On the structural changes in the Brewer-Dobson circulation after 2000, *Atmos. Chem. Phys.*, *11*, 3937–3948, 2011.

Brasseur, G. P., J. J. Orlando, and G. S. Tyndall (Eds.), *Atmospheric chemistry and global change*, Oxford University Press, 1999.

Brown, A. T., C. M. Volk, M. R. Schoeberl, C. D. Boone, and P. F. Bernath, Stratospheric lifetimes of CFC-12, CCl_4, CH_4, CH_3Cl and N_2O from measurements made by the Atmospheric Chemistry Experiment-Fourier Transform Spectrometer (ACE-FTS), *Atmos. Chem. Phys.*, *13*, 6921–6950, 2013.

Butchart, N., et al., Simulations of anthropogenic change in the strength of the Brewer-Dobson circulation, *Clim. Dyn.*, *27*, 727–741, 2006.

Carpenter, R. L., K. K. Droegemeier, P. R. Woodward, and C. E. Hane, Application of the Piecewise Parabolic Method (PPM) to Meteorological Modeling, *Mon. Wea. Rev.*, *118*, 586–612, 1990.

Carver, G. D., P. D. Brown, and O. Wild, The ASAD atmospheric chemistry integration package and chemical reaction database , *Comput. Phys. Commun.*, *105*, 197 – 215, 1997.

Dee, D. P., et al., The ERA-Interim reanalysis: configuration and performance of the data assimilation system, *Quart. J. Roy. Meteorol. Soc.*, *137*, 553–597, 2011.

Deeter, M. N., H. M. Worden, J. C. Gille, D. P. Edwards, D. Mao, and J. R. Drummond, MOPITT multispectral CO retrievals: Origins and effects of geophysical radiance errors, *J. Geophys. Res.*, 2011.

Elkins, J., et al., Airborne gas chromatograph for in situ measurements of long-lived species in the upper troposphere and lower stratosphere, *Geophys. Res. Lett.*, *23*, 347–350, 1996.

Eluszkiewicz, J., R. Hemler, J. Mahlman, L. Bruhwiler, and L. Takacs, Sensitivity of age-of-air calculations to the choice of advection scheme, *J. Atmos. Sci.*, *57*, 3185–3201, 2000.

Eyring, V., et al., A Strategy for Process-Oriented Validation of Coupled Chemistry-Climate Models, *Bull. Am. Meteorol. Soc.*, *86*, 1117–1133, 2005.

Flury, T., D. L. Wu, and W. G. Read, Variability in the speed of the Brewer-Dobson circulation as observed by Aura/MLS, *Atmos. Chem. Phys.*, *13*, 4563–4575, 2013.

Fueglistaler, S., B. Legras, A. Beljaars, J.-J. Morcrette, A. Simmons, A. M. Tompkins, and S. Uppala, The diabatic heat budget of the upper troposphere and lower/mid stratosphere in ECMWF reanalyses, *Q. J. R. Meteorol. Soc.*, *135*, 21–37, 2009.

Gerber, E. P., Stratospheric versus Tropospheric Control of the Strength and Structure of the Brewer-Dobson Circulation, *J. Atmos. Sci.*, *69*, 2857–2877, 2012.

Grooß, J.-U., Modelling of stratospheric chemistry based on HALOE/UARS satellite data, PhD thesis, University of Mainz, 1996.

Grooß, J.-U., and J. M. Russell, Technical note: A stratospheric climatology for O_3, H_2O, CH_4, NO_x, HCl, and HF derived from HALOE measurements, *Atmos. Chem. Phys.*, *5*, 2797–2807, 2005.

Grooß, J.-U., K. Brautzsch, R. Pommrich, S. Solomon, and R. Müller, Stratospheric ozone chemistry in the Antarctic: what determines the lowest ozone values reached and their recovery?, *Atmos. Chem. Phys.*, *11*, 12,217–12,226, 2011.

Günther, G., R. Müller, M. von Hobe, F. Stroh, P. Konopka, and C. M. Volk, Quantification of transport across the boundary of the lower stratospheric vortex during arctic winter 2002/2003, *Atmos. Chem. Phys.*, *8*, 3655–3670, 2008.

Hack, J. J., Parameterization of moist convection in the National Center for Atmospheric Research community climate model (CCM2), *J. Geophys. Res.*, *99*, 5551–5568, 1994.

Hall, T. M., and R. A. Plumb, Age as a diagnostic of stratospheric transport, *J. Geophys. Res.*, *99*, 1059–1070, 1994.

Hines, C. O., Doppler-spread parameterization of gravity-wave momentum deposition in the middle atmosphere. Part 1: Basic formulation, *J. Atmos. Solar Terr. Phys.*, *59*, 371–386, 1997.

Hoffmann, L., et al., Ratio of stratospheric lifetimes of CFC-11 and CFC-12 from satellite observations and a Lagrangian chemistry transport model, *in preparation for Atmos. Chem. Phys.*, 2014.

Hoppe, C. M., L. Hoffmann, P. Konopka, J.-U. Grooß, F. Ploeger, G. Günther, P. Jöckel, and R. Müller, The implementation of the CLaMS Lagrangian transport core into the chemistry climate model EMAC 2.40.1: application on age of air and transport of long-lived trace species, *Geosci. Model Dev. Diss.*, *7*, 1759–1790, 2014.

Hurrell, J. W., J. J. Hack, D. Shea, J. M. Caron, and J. Rosinski, A New Sea Surface Temperature and Sea Ice Boundary Dataset for the Community Atmosphere Model, *J. Climate*, *21*, 5145–5153, 2008.

IPCC, *Climate Change 2013: The Physical Science Basis. Contribution of Working Group I to the Fifth Assessment Report of the Intergovernmental Panel on Climate Change*, Cambridge University Press, Cambridge, United Kingdom and New York, NY, USA, 2013.

Jackson, D. R., M. D. Burrage, J. E. Harries, L. J. Gray, and J. M. Russell, The semi-annual oscillation in upper stratospheric and mesospheric water vapour as observed by HALOE, *Q. J. R. Meteorol. Soc.*, *124*, 2493–2515, 1998.

Jöckel, P., R. von Kuhlmann, M. Lawrence, B. Steil, C. Brenninkmeijer, P. Crutzen, P. Rasch, and B. Eaton, On a fundamental problem in implementing flux-form advection schemes for tracer transport in 3-dimensional general circulation and chemistry transport models, *Q. J. R. Meteorol. Soc.*, *127*, 1035–1052, 2001.

Jöckel, P., R. Sander, A. Kerkweg, H. Tost, and J. Lelieveld, Technical Note: The Modular Earth Submodel System (MESSy) - a new approach towards Earth System Modeling, *Atmos. Chem. Phys.*, *5*, 433–444, 2005.

Jöckel, P., A. Kerkweg, J. Buchholz-Dietsch, H. Tost, R. Sander, and A. Pozzer, Technical note: Coupling of chemical processes with the modular earth submodel system (MESSy) submodel TRACER, *Atmos. Chem. Phys.*, *8*, 1677–1687, 2008.

Jöckel, P., A. Kerkweg, A. Pozzer, R. Sander, H. Tost, H. Riede, A. Baumgaertner, S. Gromov, and B. Kern, Development cycle 2 of the Modular Earth Submodel System (MESSy2), *Geosci. Model Dev.*, *3*, 717–752, 2010.

Jöckel, P., et al., The atmospheric chemistry general circulation model ECHAM5/MESSy1: consistent simulation of ozone from the surface to the mesosphere, *Atmos. Chem. Phys.*, *6*, 5067–5104, 2006.

Jones, A., et al., Technical Note: A trace gas climatology derived from the Atmospheric Chemistry Experiment Fourier Transform Spectrometer (ACE-FTS) data set, *Atmos. Chem. Phys.*, *12*, 5207–5220, 2012.

Kasahara, A., Various vertical coordinate systems used for numerical weather prediction, *Mon. Wea. Rev.*, *102*, 509–522, 1974.

Konopka, P., J.-U. Grooß, G. Günther, F. Ploeger, R. Pommrich, R. Müller, and N. Livesey, Annual cycle of ozone at and above the tropical tropopause: observations versus simulations with the Chemical Lagrangian Model of the Stratosphere (CLaMS), *Atmos. Chem. Phys.*, *10*, 121–132, 2010.

Konopka, P., F. Ploeger, and R. Müller, Entropy- and static stability-based Lagrangian model grids, in *Geophysical Monograph Series: Lagrangian Modeling of the Atmosphere*, edited by J. Lin, vol. 200, pp. 99–109, American Geophysical Union, 2012.

Konopka, P., et al., Mixing and ozone loss in the 1999-2000 Arctic vortex: Simulations with the three-dimensional Chemical Lagrangian Model of the Stratosphere (CLaMS), *J. Geophys. Res.*, *109*, 2004.

Konopka, P., et al., Contribution of mixing to upward transport across the tropical tropopause layer (TTL), *Atmos. Chem. Phys.*, *7*, 3285–3308, 2007.

Lin, S., and R. Rood, Multidimensional flux-form semi-Lagrangian transport schemes, *Mon. Wea. Rev.*, *124*, 2046–2070, 1996.

Lin, S.-J., A "Vertically Lagrangian" Finite-Volume Dynamical Core for Global Models, *Mon. Wea. Rev.*, *132*, 2293–2307, 2004.

Livesey, N., et al., Earth Observing System (EOS) Aura Microwave Limb Sounder MLS version 3.3 level 2 data quality and description document, *Tech. rep.*, Jet Propulsion Laboratory, 2011.

Mahowald, N., R. Plumb, P. Rasch, J. del Corral, F. Sassi, and W. Heres, Stratospheric transport in a three-dimensional isentropic coordinate model, *J. Geophys. Res.*, *107*, 2002.

Masarie, K., and P. Tans, Extension and integration of atmospheric carbon dioxide data into a globally consistent measurement record, *J. Geophys. Res.*, *100*, 11,593–11,610, 1995.

McKenna, D. S., J.-U. Grooß, G. Günther, P. Konopka, R. Müller, G. Carver, and Y. Sasano, A new Chemical Lagrangian Model of the Stratosphere (CLaMS) 2. Formulation of chemistry scheme and initialization, *J. Geophys. Res.*, *107*, ACH 4–1–ACH 4–14, 2002a.

McKenna, D. S., P. Konopka, J.-U. Grooß, G. Günther, R. Müller, R. Spang, D. Offermann, and Y. Orsolini, A new Chemical Lagrangian Model of the Stratosphere (CLaMS) 1. Formulation of advection and mixing, *J. Geophys. Res.*, *107*, ACH 15–1–ACH 15–15, 2002b.

Minschwaner, K., L. Hoffmann, A. Brown, M. Riese, R. Müller, and P. F. Bernath, Stratospheric loss and atmospheric lifetimes of CFC-11 and CFC-12 derived from satellite observations, *Atmos. Chem. Phys.*, *13*, 4253–4263, 2013.

Müller, R., P. J. Crutzen, J.-U. Grooß, C. Brühl, J. M. Russell III, and A. F. Tuck, Chlorine activation and ozone depletion in the Arctic vortex: Observations by the

Halogen Occultation Experiment on the Upper Atmosphere Research Satellite, *J. Geophys. Res.*, *101*, 12,531–12,554, 1996.

Nordeng, T., *Extended Versions of the Convective Parametrization Scheme at ECMWF and Their Impact on the Mean and Transient Activity of the Model in the Tropics*, ECMWF technical memorandum, European Centre for Medium-Range Weather Forecasts, 1994.

Novelli, P. C., K. A. Masarie, P. M. Lang, B. D. Hall, R. C. Myers, and J. W. Elkins., Reanalysis of tropospheric CO trends: Effects of the 1997-1998 wildfires, *J. Geophys. Res.*, *108*, 2003.

Paul, J., F. Fortuin, and H. Kelder, An ozone climatology based on ozonesonde and satellite measurements, *J. Geophys. Res.*, *103*, 31,709–31,734, 1998.

Ploeger, F., P. Konopka, G. Günther, J.-U-Groß, and R. Müller, Impact of the vertical velocity scheme on modeling transport across the tropical tropopause layer, *J. Geophys. Res.*, *115*, 2010.

Ploeger, F., P. Konopka, R. Müller, G. Günther, J.-U. Groß, C. Schiller, F. Ravegnani, A. Ulanovski, and M. Riese, Backtrajectory reconstruction of water vapour and ozone in-situ observations in the TTL, *Meteorol. Z.*, *21*, 239–244, 2012a.

Ploeger, F., et al., Insight from ozone and water vapour on transport in the tropical tropopause layer (TTL), *Atmos. Chem. Phys.*, *11*, 407–419, 2011.

Ploeger, F., et al., Horizontal transport affecting trace gas seasonality in the Tropical Tropopause Layer (TTL), *J. Geophys. Res.*, *117*, 2012b.

Ploeger, F., et al., Horizontal water vapor transport in the lower stratosphere from subtropics to high latitudes during boreal summer, *J. Geophys. Res.*, *118*, 8111–8127, 2013.

Plumb, R., and J. Eluszkiewicz, The Brewer-Dobson circulation: Dynamics of the tropical upwelling, *J. Atmos. Sci.*, *56*, 868–890, 1999.

Plumb, R. A., A "tropical pipe" model of stratospheric transport, *J. Geophys. Res.*, *101*, 3957–3972, 1996.

Plumb, R. A., Tracer interrelationships in the stratosphere, *Rev. Geophys.*, *45*, 2007.

Plumb, R. A., and M. K. W. Ko, Interrelationships between mixing ratios of long-lived stratospheric constituents, *J. Geophys. Res.*, *97*, 10,145–10,156, 1992.

Pommrich, R., R. Müller, J.-U. Grooß, P. Konopka, G. Günther, H.-C. Pumphrey, S. Viciani, F. D'Amato, and M. Riese, Carbon monoxide as a tracer for tropical troposphere to stratosphere transport in the Chemical Lagrangian Model of the Stratosphere (CLaMS), *Geosci. Model Dev. Discuss.*, *4*, 1185–1211, 2011.

Pommrich, R., et al., Tropical troposphere to stratosphere transport of carbon monoxide and long-lived trace species in the Chemical Lagrangian Model of the Stratosphere (CLaMS), *in preparation for Geosci. Model Dev. Discuss.*, 2014.

Punge, H. J., P. Konopka, M. A. Giorgetta, and R. Müller, Effects of the quasi-biennial oscillation on low-latitude transport in the stratosphere derived from trajectory calculations, *J. Geophys. Res.*, *114*, 2009.

Randel, W., and E. Jensen, Physical processes in the tropical tropopause layer and their roles in a changing climate, *Nature Geoscience*, *6*, 169–176, 2013.

Randel, W. J., F. Wu, J. M. Russell, A. Roche, and J. W. Waters, Seasonal cycles and QBO variations in stratospheric CH_4 and H_2O observed in UARS HALOE data, *J. Atmos. Sci.*, *55*, 163–185, 1998.

Randel, W. J., M. Park, F. Wu, and N. Livesey, A large annual cycle in ozone above the tropical tropopause linked to the Brewer-Dobson circulation, *J. Atmos. Sci.*, *64*, 4479–4488, 2007.

Ravishankara, A. R., J. S. Daniel, and R. W. Portmann, Nitrous Oxide (N_2O): The Dominant Ozone-Depleting Substance Emitted in the 21st Century, *Science*, *326*, 123–125, 2009.

Reithmeier, C., and R. Sausen, ATTILA: atmospheric tracer transport in a Lagrangian model, *Tellus B*, *54*, 278–299, 2002.

Riese, M., F. Ploeger, A. Rap, B. Vogel, P. Konopka, M. Dameris, and P. Forster, Impact of uncertainties in atmospheric mixing on simulated UTLS composition and related radiative effects, *J. Geophys. Res.*, *117*, 2012.

Rigby, M., et al., Re-evaluation of the lifetimes of the major CFCs and CH_3CCl_3 using atmospheric trends, *Atmos. Chem. Phys.*, *13*, 2691–2702, 2013.

Röckner, E., R. Brokopf, M. Esch, M. Giorgetta, S. Hagemann, L. Kornblueh, E. Manzini, U. Schlese, and U. Schulzweida, Sensitivity of simulated climate to horizontal and vertical resolution in the ECHAM5 atmosphere model, *J. Climate*, *19*, 3771–3791, 2006.

Roeckner, E., et al., The atmospheric general circulation model ECHAM5. PART I: Model description, *Tech. Rep. MPI-Report 349*, Max Planck Institute for Meteorology, 2003.

Schoeberl, M. R., A. R. Douglass, Z. X. Zhu, and S. Pawson, A comparison of the lower stratospheric age spectra derived from a general circulation model and two data assimilation systems, *J. Geophys. Res.*, *108*, 4113, 2003.

Schoeberl, M. R., A. E. Dessler, and T. Wang, Simulation of stratospheric water vapor and trends using three reanalyses, *Atmos. Chem. Phys.*, *12*, 6475–6487, 2012.

Seviour, W. J. M., N. Butchart, and S. C. Hardiman, The Brewer-Dobson circulation inferred from ERA-Interim, *Q. J. R. Meteorol. Soc.*, *138*, 878–888, 2012.

Shaw, T. A., and T. G. Shepherd, Raising the roof, *Nature Geoscience*, *1*, 12–13, 2008.

Simmons, A. J., D. M. Burridge, M. Jarraud, C. Girard, and W. Wergen, The ECMWF medium-range prediction models development of the numerical formulations and the impact of increased resolution, *Meteorol Atmos Phys*, *40*, 28–60, 1989.

Solomon, S., K. Rosenlof, R. Portmann, J. Daniel, S. Davis, T. Sanford, and G.-K. Plattner, Contributions of stratospheric water vapor to decadal changes in the rate of global warming, *Science*, *327*, 1219–1223, 2010.

Son, S.-W., et al., The impact of stratospheric ozone recovery on the southern hemisphere westerly jet, *Science*, *320*, 1201–1204, 2008.

SPARC, *SPARC report on the evaluation of chemistry-climate models*, SPARC Rep. No. 5, WRCP-132, WMO-TD No. 1526, World Meteorol. Organ., 2010.

SPARC, *SPARC Report on the Lifetimes of Stratospheric Ozone-Depleting Substances, Their Replacements, and Related Species*, SPARC Rep. No. 6, WRCP-15/2013, World Meteorol. Organ., 2013.

Steinhorst, H.-M., P. Konopka, G. Günther, and R. Müller, How permeable is the edge of the Arctic vortex: Model studies of winter 1999-2000, *J. Geophys. Res.*, *110*, 2005.

Stenke, A., V. Grewe, and M. Ponater, Lagrangian transport of water vapor and cloud water in the ECHAM4 GCM and its impact on the cold bias, *Clim. Dynam.*, *31*, 491–506, 2008.

Stenke, A., M. Dameris, V. Grewe, and H. Garny, Implications of Lagrangian transport for simulations with a coupled chemistry-climate model, *Atmos. Chem. Phys.*, *9*, 5489–5504, 2009.

Stevens, B., et al., Atmospheric component of the MPI-M Earth System Model: ECHAM6, *Journal of Advances in Modeling Earth Systems*, *5*, 146–172, 2013.

Stiller, G. P., et al., Global distribution of mean age of stratospheric air from MIPAS SF_6 measurements, *Atmos. Chem. Phys.*, *8*, 677–695, 2008.

Strahan, S. E., et al., Using transport diagnostics to understand chemistry climate model ozone simulations, *J. Geophys. Res.*, *116*, 2011.

Sutton, R. T., H. Maclean, R. Swinbank, A. O'Neill, and F. W. Taylor, High-resolution stratospheric tracer fields estimated from satellite observations using Lagrangian trajectory calculations, *J. Atmos. Sci.*, *51*, 2995–3005, 1994.

Thompson, D. W. J., and S. Solomon, Interpretation of recent Southern Hemisphere climate change, *Science*, *296*, 895–899, 2002.

Tiedtke, M., A comprehensive mass flux scheme for cumulus parameterization in large-scale models, *Mon. Wea. Rev.*, *117*, 1779–1800, 1989.

Tost, H., P. Jöckel, and J. Lelieveld, Influence of different convection parameterisations in a GCM, *Atmos. Chem. Phys.*, *6*, 5475–5493, 2006.

Volk, C. M., J. W. Elkins, D. W. Fahey, G. S. Dutton, J. M. Gilligan, M. Loewenstein, J. R. Podolske, and K. R. Chan, On the evaluation of source gas lifetimes from stratospheric observations, *J. Geophys. Res.*, *102*, 25,543–25,564, 1997.

Waugh, D., and T. Hall, Age of stratospheric air: Theory, observations, and models, *Rev. Geophys.*, *40*, 2002.

Weber, M., S. Dikty, J. P. Burrows, H. Garny, M. Dameris, A. Kubin, J. Abalichin, and U. Langematz, The Brewer-Dobson circulation and total ozone from seasonal to decadal time scales, *Atmos. Chem. Phys.*, *11*, 11,221–11,235, 2011.

WMO, *Scientific assessment of ozone depletion: 2010*, Global Ozone Research and Monitoring Project–Report No. 52, Geneva, Switzerland, 2011.

Wohltmann, I., and M. Rex, The Lagrangian chemistry and transport model ATLAS: validation of advective transport and mixing, *Geosci. Model Dev.*, *2*, 153–173, 2009.

Wright, J. S., and S. Fueglistaler, Large differences in reanalyses of diabatic heating in the tropical upper troposphere and lower stratosphere, *Atmos. Chem. Phys.*, *13*, 9565–9576, 2013.

Zhang, G., and N. McFarlane, Sensitivity of Climate Simulations to the Parameterization of Cumulus Convection in the Canadian Climate Center General-Circulation Model, *Atmos. Ocean*, *33*, 407–446, 1995.

List of Figures

Danksagung

An dieser Stelle möchte ich mich ganz herzlich bei allen Menschen bedanken, die mich in der Zeit meiner Doktorarbeit unterstützt haben.

Als Erstes gilt mein Dank meinem Doktorvater Rolf Müller, der sich immer viel Zeit für Gespräche mit mir genommen hat, und mir viele Anregungen und Ideen zu dieser Arbeit gegeben hat. Des Weiteren möchte ich ich mich bei Prof. Martin Riese bedanken, der mir die Möglichkeit gegeben hat am Forschungszentrum Jülich meine Doktorarbeit zu schreiben und an verschiedenen Konferenzen und an der Climate Modelling Summerschool in Cambridge teilzunehmen. Vielen Dank an Prof. Ralf Koppmann für die Begutachtung dieser Arbeit.

Dann möchte ich mich bei Lars Hoffmann, meinem Ansprechpartner in Jülich Supercomputing Center bedanken, der meine Arbeit sehr engagiert unterstützt hat.

Desweiteren gilt mein Dank den Personen, die mir bei meiner Arbeit mit komplexen Modellen in wissenschaftlichen und technischen Fragen sehr weitergeholfen haben. Dies in der CLaMS Gruppe vor allem Felix Ploeger, Paul Konopka, Jens-Uwe Grooß und Nicole Thomas, sowie Patrick Jöckel für das EMAC Modell.

Ich danke weiterhin den vielen beteiligten Instituten, die Satelliten- und Modelldaten zur Verfügung gestellt haben, dies sind: ECMWF für ERA-Interim Reanalysedaten, die University of Waterloo, Canada für die ACE-FTS Klimatologie und das NASA Goddard Earth Sciences Data and Information Center für die MLS Daten. Ich bedanke mich bei dem Jülich Supercomputing Center für den Support und die zur Verfügung gestellte Rechenzeit. Vielen Dank auch an Sebastian Rast, Hauke Schmidt und Peter Lauitzen für die Bereitstellung von Diagnosetools ihrer Modelle.

Vielen Dank an Tanya Peevey und Roman Litzinger für das Korrekturlesen von Teilen dieser Arbeit.

Des Weiteren möchte ich mich bei meinen Kollegen im IEK-7 für die schöne Arbeitsatmosphäre während meiner Doktorandenzeit bedanken. Ein besonderes Dankeschön gilt Tobias, Felix, Priya, Tanya, Silvio und Ines.

Einen herzlichen Dank an alle, die neben der Arbeit für mich da waren. Danke an alle Freunde in Köln, besonders Julia. Danke an meine Fahrgemeinschaft, die jeden Tag mit mit von Köln nach Jülich gependelt ist. Ich bedanke mich bei meinen Eltern und ganz besonders bei meinem Mann Michael.

Band / Volume 214
Lebensdauer und Schädigungsentwicklung martensitischer Stähle für Niederdruck-Dampfturbinenschaufeln bei Ermüdungsbeanspruchung im VHCF-Bereich
S. Kovacs (2014), IV, 140 pp
ISBN: 978-3-89336-959-1

Band / Volume 215
Micro- and Macro- Mechanical Testing of Transparent $MgAl_2O_4$ Spinel
O. Tokariev (2014), X, 99 pp
ISBN: 978-3-89336-960-7

Band / Volume 216
Potentiale des Strommanagements zur Reduzierung des spezifischen Energiebedarfs von Pkw
T. Grube (2014), IX, 255 pp
ISBN: 978-3-89336-961-4

Band / Volume 217
Transmutation von Transuranen in einem gasgekühlten beschleunigergetriebenen System
K. H. Biß (2014), IV, 157 pp
ISBN: 978-3-89336-964-5

Band / Volume 218
Untersuchung des photochemischen Terpenoidabbaus in der Atmosphärensimulationskammer SAPHIR
M. Kaminski (2014), 148, VI pp
ISBN: 978-3-89336-967-6

Band / Volume 219
Interaction of Phosphoric Acid with Cell Components in High Temperature Polymer Electrolyte Fuel Cells
F. Liu (2014), i, 147 pp
ISBN: 978-3-89336-972-0

Band / Volume 220
Machbarkeitsstudie zum Aufbau und Betrieb eines Prüfstandes für Antriebsstränge von Windenergieanlagen mit Getriebe im Leistungsbereich bis 15 MW am Standort Forschungszentrum Jülich
(2014), 72 pp
ISBN: 978-3-89336-973-7

Band / Volume 221
Phenotyping Nannochloropsis gaditana under different conditions in controlled photobioreactors in laboratory and upscaled photobioreactors in greenhouse
R. Braun (2014), III, 177 pp
ISBN: 978-3-89336-975-1

Band / Volume 222
Fundamental processes of plasma and reactive gas surface treatment for the recovery of hydrogen isotopes from carbon co-deposits in fusion devices
S. Möller (2014), 99 pp
ISBN: 978-3-89336-977-5

Band / Volume 223
Analyse der Lichtstreuung zur Textur-Optimierung von Zinkoxid-Frontkontakten für Silizium-Dünnschichtsolarzellen
G. Jost (2014), viii, 203 pp
ISBN: 978-3-89336-978-2

Band / Volume 224
Luftgestützte Messung von HOx-Radikalkonzentrationen mittels Laser-induzierter Fluoreszenz auf einem Zeppelin NT: Untersuchung der atmosphärischen Oxidationsstärke der unteren Troposphäre
S. Gomm (2014), 5, iii, 205 pp
ISBN: 978-3-89336-981-2

Band / Volume 225
Sorption, Transformation and Transport of Sulfadiazine in a loess and a sandy Soil
S. Sittig (2014), v, 121 pp
ISBN: 978-3-89336-982-9

Band / Volume 226
A Lagrangian transport core for the simulation of stratospheric trace species in a Chemistry Climate Model
C. M. Hoppe (2014), vi, 112 pp
ISBN: 978-3-89336-984-3

Weitere ***Schriften des Verlags im Forschungszentrum Jülich*** unter
http://wwwzb1.fz-juelich.de/verlagextern1/index.asp

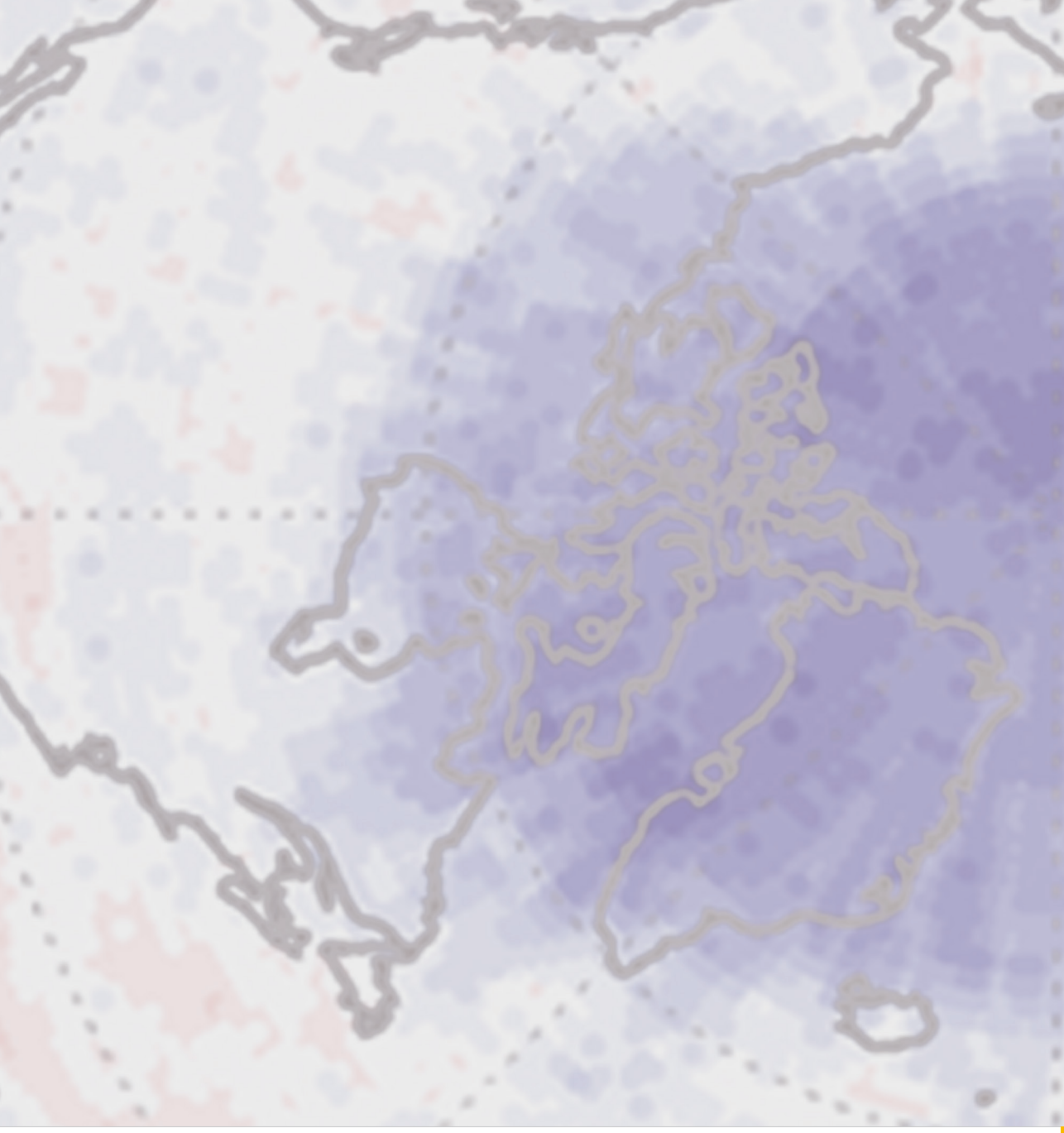

Energie & Umwelt / Energy & Environment
Band / Volume 226
ISBN 978-3-89336-984-3

JÜLICH
FORSCHUNGSZENTRUM